technische universität
dortmund

Dissertation zur Erlangung des
Doktorgrades der Naturwissenschaften

vorgelegt von

Nina Fröhling

Fourth-Order Spin Correlation in Doped Semi-Conductor Quantum Dots

Technische Universität Dortmund
Fakultät Physik
Lehrstuhl für Theoretische Physik II

April 2019

Erster Gutachter	Prof. Dr. Frithjof B. Anders
Zweiter Gutachter	Prof. Dr. Mikhail M. Glazov
Kontakt zum Autor	nina.froehling@tu-dortmund.de

Contents

Publication List

- N. Fröhling and F. B. Anders *Long-time coherence in fourth-order spin correlation functions* Phys. Rev. B 96, 045441, (2017)
- N. Fröhling, F. B. Anders, M. M. Glazov *Nuclear spin noise in the central spin model*, Phys. Rev. B 97, 195311 , (2018)
- N. Fröhling, N. Jäschke, F. B. Anders *Fourth-order spin correlation function in the extended central spin model*, arXiv:1901.08923, submitted to and accepted by Phys. Rev. B, at the time of writing in preprint (2019)

Chapter 1

Introduction

Quantum computation has been of great interest to scientists for decades. Moore's law says the number of transistors in a dense integrated circuit doubles every two years [1]. With electronic devices becoming smaller and more efficient each year, there is a natural end point for classical computing, where quantum effects become relevant. But the future of quantum computation is not only inevitable if we want to continue on our current trajectory of technological growth and improvement, it also brings with it a number of unique advantages. It was Feynman who in 1982 first suggested that classical computers might not be ideal for simulating quantum mechanical problems [2], but that a quantum mechanical system should be preferable. A classical computer can only simulate a quantum system in a computation time growing exponentially with the system size. His conjecture was later proven by Bernstein and Vazirani [3], who – based on a quantum mechanical Turing machine – showed that a quantum computer would be able to simulate a quantum system in polynomial instead of exponential time. This constitutes a great improvement and makes a quantum computer highly desirable. Later works put forward different algorithms [4, 5] that could be implemented more efficiently on a quantum computer, most famously Shor's integer factorization algorithm [6, 7].

In a classical computer, information is stored in a bit that can take on the states of 0 and 1 and can be implemented as a capacitor that is either charged or uncharged. A quantum computer needs a quantum bit (or qubit), where information can be stored as the states $|0\rangle$ and $|1\rangle$, or, unlike the classical case, a superposition of both. A variety of suggestions have been made how this qubit should be implemented. Possible candidates for a qubit are superconducting circuits [8–10], nuclear spins of molecules in liquids [11, 12], phosphorous impurities in silicon [13] and nitrogen vacancies in diamonds [14–16]. This work, however, focuses on electron spins trapped in semi-conductor quantum dots (QD) [17–28]. Unlike, for example, impurities in diamonds, such QDs can be easily integrated into existing semi-conductor devices. Also, they allow for ultrafast optical initialization and control [24, 28, 29].

The fundamental challenge in the realization of a quantum bit by a QD is

the loss of information, as interaction with a fluctuating environment causes the electron spin to decay over time. Trapping the electron in a QD suppresses spin decoherence caused by free movement, but the high localization of the electron causes the Fermi contact hyperfine interaction [30] to dominate the short time dynamics of the confined electron spin [31–35]. In order to understand the decoherence mechanisms, an in-depth investigation of the interaction processes influencing the electron spin dynamics in QDs on all time scale is desirable.

Gaudin [36] first proposed the central spin model (CSM) to describe QD systems. It consists of a central electron or hole spin that interacts with its surrounding nuclear spin bath via hyperfine interaction. The interactions between nuclear spins are neglected. The CSM has proven to be well suited as a theoretical description of QD systems [31, 32, 37, 38] and has been the subject of numerous studies over the years. The CSM is integrable and solvable via Bethe ansatz, both exactly [39–42] and stochastically [43, 44]. Due to the highly sophisticated nature of the Bethe ansatz, its solution is limited to certain initial conditions and bath sizes below $N = 50$. The highest number of nuclear spins that can be simulated is $N = 1000$ via TD-DMRG [45], but this method is restricted to small time frames.

In order to gain insight into the physics of a system, it has to be observed in experiment. Spin noise spectroscopy (SNS) [46], originally proposed by Aleksandrov and Zapasskii [47, 48], has since been established as a minimally invasive, weak measurement of electron spin dynamics. Here, a linearly polarized laser beam propagating through the probe experiences rotation of its polarization plane orientation caused by local magnetization of the medium. SNS was employed to observe the spin noise in an ensemble of alkali atoms [49] and in bulk semiconductors [50–52]. It was also used to study the influence of the nuclear-electric quadrupolar interactions in an ensemble of semi-conductor QD [21] on the long-time decoherence [53, 54] of the second-order spin correlation [55–61].

The analysis of the second-order spin noise spectrum [38,51,54,55,57,59,61,62] reveals much of the intrinsic dynamics of the central spin. However, the information obtained from second-order correlation, whether in real-time or in the frequency domain, is limited by the fluctuation dissipation theorem to linear effects, if only the thermal equilibrium is considered. For this reason many experiments utilize non-equilibrium conditions, whether generated by radio frequency [63–65] or through periodic laser pulsing [28, 66–70].

Recently, correlation functions beyond second-order were suggested [71–73] as a way to measure quantum effects not accessible by second-order correlation or second-order noise. Higher order spectra have also been utilized to study dynamical decoupling schemes [73–75], and it has been shown that higher order contributions arise from strong continuous measurement of the spin noise [76]. Bechtold et al. have measured the joint probability of finding an electron spin in the spin-$|\downarrow\rangle$ state at two consecutive measurements, after the electron had been initialized in the spin-$|\downarrow\rangle$ state in the beginning. This can be described by a fourth-order spin correlation function. Press et al [29] slowed down the electron

spin decay in a QD via spin echo method, where the spin echo amplitude is likewise given by a fourth-order spin correlation function.

The focus of this work will be the studies of fourth-order correlation functions and noise in a QD system, in order to reveal what additional information they carry in comparison to the well-known and long studied second-order correlation. The work is organized as follows: Chapter 2 gives an introduction into the experimental background. The basic techniques and ideas are reviewed briefly: what QDs are, how an electron spin in a QD can be manipulated, and how the spin polarization can be measured. In Chapter 3 the theoretical modeling of all interactions relevant to an electron localized in a QD will be discussed in detail. We will introduce the Fermi contact hyperfine interaction and review its derivation. The simple CSM will be extended by nuclear-electric quadrupolar coupling, where the quadrupolar moments of the nuclear spins couple to the electric strain field of the QD. Chapter 4 gives an overview of the different correlation functions discussed in this work, as well as a very brief introduction into cumulant theory. Chapter 5 presents the methods used to investigate the correlation functions. The analytical methods given are the frozen Overhauser field approximation and the exact solution of the CSM with homogeneous hyperfine couplings. The numerical methods are the calculation of second and fourth-order correlation functions via exact diagonalisation (ED) of the Hamilton matrix, and a more elaborate time propagation scheme based on the Lanczos method. Lastly, a semi-classical method is presented employing the numerical solution of the equations of motion of the spins treated as classical magnetic moments.

The central results of this thesis can be found in Chapter 6-8. Chapter 6 reviews different hyperfine coupling distributions and their effect on the second-order correlation, as well as general features of second-order correlation and the influence of quadrupolar coupling on its long time decay. The same chapter also introduces the spin bath correlation and investigates it both analytically exact and via a numerical scheme. In Chapter 7, the fourth-order spin noise is investigated thoroughly using both classical and quantum mechanical methods. Chapter 8 studies the real time fourth-order spin correlation functions that were already observed in experiments [29,72]. We show that the observables measured in both experiments are described by fourth-order correlation functions and analyze the physical origin of the different time scales of the decay. We provide strong evidence that the additional magnetic field dependent long-time exponential decay is governed by the relation between the quadrupolar interaction causing the decoherence and the nuclear Zeeman effect which is suppressing the decay.

Chapter 2

Experimental Background

This chapter gives a brief review of the experimental background of this thesis. Section 2.1 explains what QDs are and how they are formed. In Sec. 2.2 details how the spin of a charge carrier trapped in a QD can be manipulated into the desired state. Two different ways to measure the spin polarization of said charge carrier are presented in Sec. 2.3.

2.1 Semi-conductor Quantum Dots

In most solid materials the atoms align in a lattice whose structure is periodic in space. The specific form of this lattice causes the charge carriers to form energy bands. The highest energy that an electron can have at a temperature of 0 K is called the Fermi energy. In metals the Fermi energy is located in a band, which makes the material conductive. In isolators and semi-conductors all bands are either completely below or completely above the Fermi energy. The bands closest to the Fermi energy are called valence bands if they are below the Fermi energy, and conduction bands if they are above it. In an undoped semi-conductor or an isolator, the lowest conduction band and the highest valence band are separated by a band gap, with the Fermi energy in between. The band gap energy, the difference between the highest valence state and the lowest conduction state, is the lowest energy needed to excite an electron bound to a valence state into a conduction state. The difference between isolators and semi-conductors is the value of the band gap energy: In

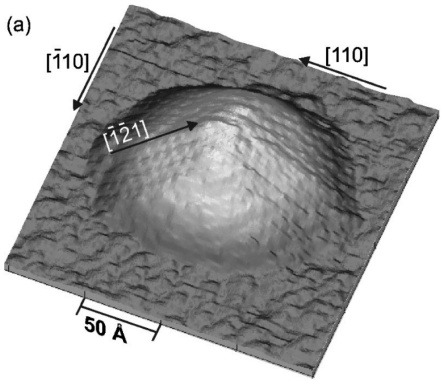

Figure 2.1: Uncovered InAs QD grown with the Stranski-Krastranov method anatomically resolved by scanning tunneling microscopy. Figure taken from Ref. [77].

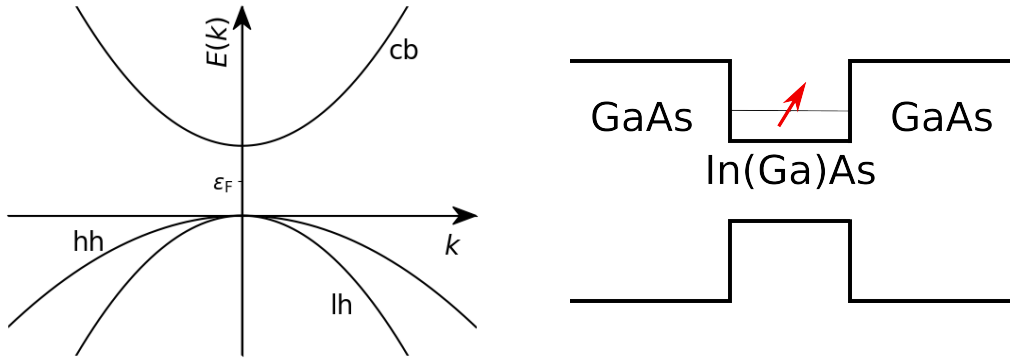

Figure 2.2: On the left a typical simplified band structure of a semi-conductor is shown. The conduction band is above the Fermi energy. hh stands for heavy holes, while lh means light holes. All bands have a paraboloid shape near the band gap. One the right one can see a schematic for the QD, with a spin trapped in the valence band of $In_{1-x}Ga_xAs$, between the barrier created by the much higher band gap of GaAs.

isolators, the band gap is to large to be bridged, while in semi-conductors it is sufficiently small that a charge carrier from the valence state can be excited into the conduction state. In this work, the experiments considered are usually conducted at $6 - 8\,\mathrm{K}$, a temperature sufficiently low that the valence bands can be considered completely filled and the conduction bands completely empty. If a semi-conductor is confined in all directions by another semiconducting material with a significantly higher band gap, carriers can be contained in the potential well that is created. This is called a semi-conductor quantum dot (QD).

These QDs are usually several nanometers large and consist of $10^5 - 10^6$ atoms. Due to the high localization, the energy bands become discrete energy states. Therefore, a QD is sometimes referred to as an 'artificial atom'. QDs can be used as a component for single electron transistors, where the QD is sandwiched between a source and a drain, with an applied gate voltage which controls the QDs energy levels. Another important use for QD is as an electron trap. This enables researchers to manipulate the charge carrier spin and observe its decay without the carrier tunnelling away or interacting with other carriers.

There are several methods to create a QD, but the experiments we will analyze use InGaAs QDs self-assembled via molecular beam epitaxy (MBE) based on the Stranski-Krastanov-growth process [78, 79]. There, a several atoms thick wetting layer of InAs is applied on a GaAs surface. Due to the strain resulting from 7% smaller lattice constants of the barrier material (GaAs) compared to the dot material (InAs), islands of InAs arch up, forming the QD. After that, another GaAs barrier is applied. The dot material will usually also contain Ga, leading to $In_{1-x}Ga_xAs$ dots. The lattice strain that causes the $In_{1-x}Ga_xAs$ to arch, also creates electric field gradients which will be important later.

Control of the amount of QDs created can be achieved by increasing or decreasing the amount of InAs deposited on the GaAs barrier. The QD can be n-doped with an electron or p-doped with a hole. One way to achieve n-doping

is by growing a doping layer, e.g. consisting of Si, underneath the substrate. By electron tunneling from the donor atoms into the QDs, the QDs become charged with usually one electron per QD. Another process to manipulate the QD's physical properties is called annealing [80]. Here, the sample is heated to cause diffusion of the sample material into the QD and vice versa.

A QD can be doped by an electron or a hole. Since the periodic part of the Bloch function of the conduction states is s like, the electron in the conduction band has spin 1/2. On the other hand a valence state is p like, which means that the hole has the total angular momentum $J = 3/2$. Holes with $J_z = \pm 1/2$ are called light holes and those with $J_z = \pm 3/2$ are heavy holes, since their effective mass is determined by the curvature of the bands, see left panel of Fig. 2.2.

Now that we briefly discussed the most important features of the quantum system in question, we will explain how a carrier spin trapped in a QD can be controlled.

2.2 Pumping a Quantum Dot

Pumping a QD with coherent laser pulses is one way to initialize the electron spin in a preferred state in an optical experiment. Here, the quantization axis is chosen to be parallel to the optical axis.

The optical selection rules are shown in Fig. 2.3 and are the same for excitation via photon absorption as well as for relaxation via photon emission. Circularly polarized laser pulses carry an angular momentum and can increase (σ^+) or decrease (σ^-) the total angular momentum by 1. A pulse can excite an electron from a valence state into a conduction state and leave behind a hole. These electron-hole pairs trapped in the QD are called excitons. If the conduction state was already populated by an electron, the two electrons in the conduction state will form a singlet. Together with the valence state hole, this is called a trion state $|\uparrow\downarrow\Uparrow\rangle$. Due to quantum confinement or strain, the heavy and light hole states are separated by an energy gap of several tens of meV. Therefore, the light hole excitation can usually be neglected. However, strain and rotational symmetry breaking in the QD can cause heavy to light hole coupling, which makes all transitions shown in Fig. 2.3 possible, though heavy hole excitation still being much more probable than light hole excitation.

Polarization is achieved in the system by applying an external magnetic field transversal to the optical axis, where the Larmor precession is faster or equal to the trion decay. Figure 2.3 depicts how an expectation value of polarization in a rotating system arises during trion decay. When a QD doped with an electron is pumped with σ^- polarised light, the electron is unaffected if it is in the $|\uparrow\rangle$ state. Then, the electron freely precesses in the magnetic field, which is shown in Fig. 2.3 as the red spin standing still in the system rotating with Larmor frequency. If the electron is in the $|\downarrow\rangle$ state, a trion is excited ($|\downarrow\rangle \rightarrow |\downarrow\uparrow\Downarrow\rangle$, which does not

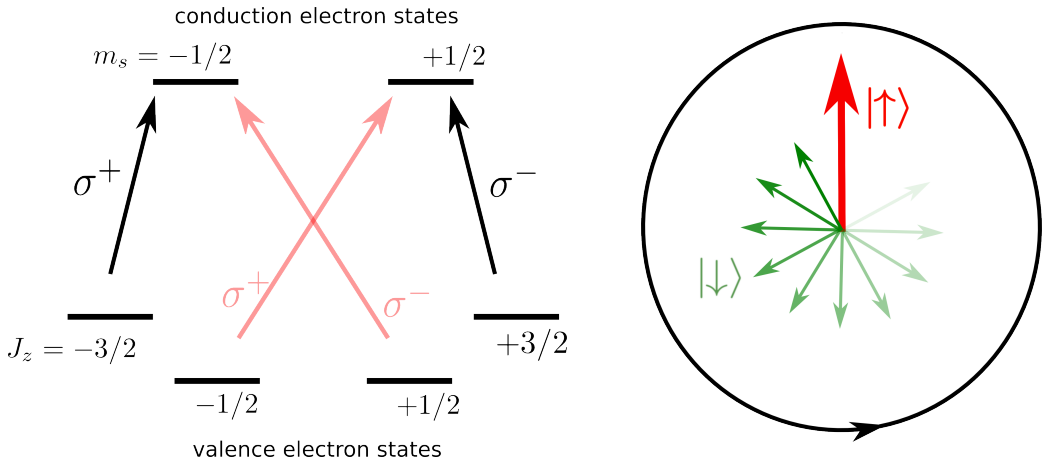

Figure 2.3: On the left: Optical selection rules for exciting electrons from the valence state to the conduction states [81]. Since the $J = 1/2$ and the $J = 3/2$ states are far apart in energy, the $J = 1/2$ states can usually be neglected for optical excitation and are not shown here. The excitation from the $\pm 1/2$ valence states is less likely than the excitation from the $\pm 3/2$ states. A σ^+ (σ^-) pulse will increase (decrease) the angular momentum by 1. On the right: Spins during trion decay in a system rotating in the transversal magnetic field. If the spin is during the σ^- pulse in the $|\uparrow\rangle$ state, it is not affected. If it is in the $|\downarrow\rangle$ state, the spin is excited into the trion state. As the trion decays, the $|\downarrow\rangle$ is reintroduced into the rotating system at a random time, averaging out the $|\downarrow\rangle$ polarization.

precess since the g factor of the trion is negligible. But after a short but random time period, the trion relaxes back into the spin $|\downarrow\rangle$ state. As the trion decay rate is large compared to the precession period of the rotating system, the expectation value of the relaxed $|\downarrow\rangle$ spin in the rotating system averages, ideally, to zero. As nothing will happen to the spin if it is in the $|\uparrow\rangle$ state, this creates an effective polarization of the system.

2.3 Measuring the Polarization

It is a fundamental principle of quantum mechanics that no measurement can be made without simultaneously perturbing the system. Observation of a particle for instance causes the immediate collapse of the wave function describing the probability of the particle to be in a specific state. Therefore, frequent measurement means frequent collapse of the wave function, and can suppress time evolution of the system. This is known as the quantum Zeno effect. In this chapter, however, we will discuss only two limits, very weak and very strong measurement. It is possible to do a continuous measurement of polarization in an ensemble of QD where the perturbation is weak enough to be negligible. This is called the weak measurement limit. On the other hand, polarization can also be measured in such a way that completely destroys the state measured, but in a predictable way. Both methods are part of experiments discussed in this thesis.

2.3.1 Weak Measurement Limit

By optically exciting a doped QD it is possible to gain information about the state of the QD at the time of the measurement. As described in the above section, a σ^- polarized laser pulse will excite a trion if the electron is in the $|\downarrow\rangle$ state, and the photon emitted when the trion decays can be detected. Since no photon will be emitted if the electron is in the spin $|\uparrow\rangle$ state, optical excitation gives us information about the state of the system at a specific time. However, this measurement also changes the state by exciting a trion. This section will deal with weakly measuring the polarization within an ensemble of QDs, meaning measuring the polarization without non-negligibly influencing the measured system. While the spins were described quantum mechanically before, for the derivation of the Faraday rotation a classical description will be used.

The Faraday rotation can be used to measure magnetic polarization in a system. If an electromagnetic wave propagates through a medium, it will induce oscillating electric dipoles in the atoms. The force on an electron in an electric field $\vec{E}$ and a magnetic field $\vec{B}$ is

$$\vec{F} = -e(\vec{E} + \frac{1}{c}\vec{v} \times \vec{B}). \tag{2.3.1}$$

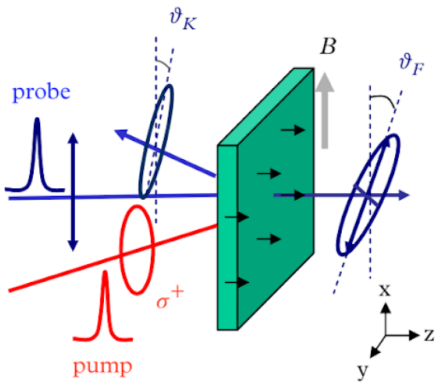

Figure 2.4: Schematic of a pump–probe experiment in Voigt geometry, to illustrate the Faraday rotation measurement technique. θ_F denotes the Faraday rotation angle. Figure taken from Ref. [82].

If the magnetic field only stems from the electromagnetic wave, $|\vec{B}| \approx |\vec{E}|$, the Lorentz force term can usually be neglected since the electron moves non-relativistically, $v \ll c$. But if a background magnetic field is present (as is the case when the system is polarized), the second term contributes. If the propagation direction of the electronic wave and the background magnetic field are aligned in z direction, then the electric field $\vec{E}$ and the vector $\vec{s}$, which describes the displacement of the electron from equilibrium, are constrained to the xy plane.

We assume the atomic electrons have a natural frequency ω_0 and both $\vec{s}$ and $\vec{E}$ have an $\exp(-\mathrm{i}\omega t)$ time dependence. The resulting equations of motion can be solved by defining $s_\pm = s_x \pm \mathrm{i}s_y$ and $E_\pm = E_x \pm \mathrm{i}E_y$, yielding

$$s_\pm = -\frac{eE_\pm}{m(\omega_0^2 - \omega^2 \mp \Omega\omega)} \tag{2.3.2}$$

with Ω being the cyclotron frequency $\Omega = eB/mc$. Since the dipole moment is $P_\pm = n_e e s_\pm$, where n_e is the number of electrons that oscillate in the applied electromagnetic field, and the polarizability is $\chi_\pm = 4\pi P_\pm / E_\pm$, we arrive at different

refractory indices for left-handed and right-handed circularly polarized waves

$$n_{\pm} = \sqrt{1+\chi_{\pm}} = \sqrt{1 + \frac{4\pi e^2 n_e}{m(\omega_0^2 - \omega^2 \mp \Omega\omega)}}. \tag{2.3.3}$$

Since the cyclotron frequency is usually quite small compared to the frequency of a light wave, $\omega, \omega_0 \gg \Omega$, the difference between the refractive index of left-hand circularly polarized light and right-hand circularly polarized light becomes

$$\Delta n = n_+ - n_- \approx \frac{4\pi e^2 n_e \omega}{m(\omega_0^2 - \omega^2)^2}\Omega, \tag{2.3.4}$$

linearly dependent on the background field strength B. The mean refractive index can be expressed as

$$n = \frac{n_+ + n_-}{2} \approx 1 + \frac{2\pi e^2 n_e}{m(\omega_0^2 - \omega^2)}. \tag{2.3.5}$$

An electromagnetic wave that propagates in z direction can always be described as a linear combination of left-hand circularly polarized and right-hand circularly polarized light,

$$\vec{E}(z,t) = E_+ e^{\mathrm{i}(k_+ z - \omega t)}\vec{e}_+ + E_- e^{\mathrm{i}(k_- z - \omega t)}\vec{e}_-. \tag{2.3.6}$$

Assuming that the wave was fully polarized in x direction at $z = 0$ ($\vec{E}(z=0,t) = E_w \exp(-\mathrm{i}\omega t)\vec{e}_x$), the electromagnetic field can be written as

$$\vec{E}(z,t) = E_w \left[\cos\left(\frac{\Delta n \omega}{2c} z\right)\vec{e}_x - \sin\left(\frac{\Delta n \omega}{2c} z\right)\vec{e}_y\right] e^{-\mathrm{i}\omega t} e^{\mathrm{i}\frac{n\omega}{c}z} \tag{2.3.7}$$

with the change of the polarization angle by propagation distance

$$\frac{\partial \theta_F}{\partial z} = \frac{\Delta n \omega}{2c}. \tag{2.3.8}$$

As electromagnetic radiation typically has frequencies much higher than the resonance frequency of atoms, $\omega \gg \omega_0$, the total change of the polarization angle of the light after having travelled through the sample is

$$\Delta\theta_F = \frac{e^3 \lambda^2}{2\pi (mc^2)^2} \int \mathrm{d}z\, n_e(z) B(z) \tag{2.3.9}$$

with the wavelength $\lambda = 2\pi c/\omega$. This allows measurement of the polarization and, therefore, of the state of the electron spin in a QD or a QD ensemble without generating a spin flip and disturbing the system non-negligibly.

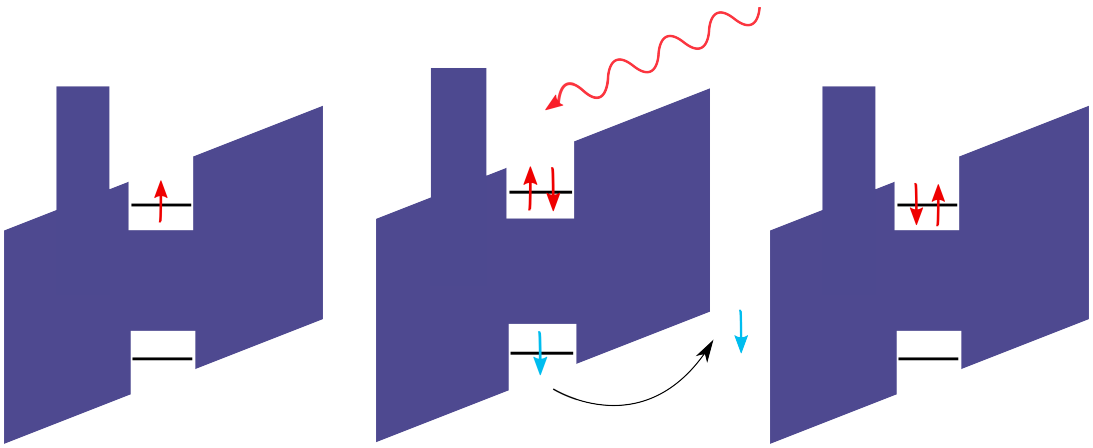

Figure 2.5: A QD doped with an electron in the $|\uparrow\rangle$-state, with applied voltage and an asymmetric tunnel barrier. The left panel shows the system before the σ^+ pulse, the center panel shows the system immediately after the laser pulse excited a trion. Due to the applied voltage, the hole in the valence state tunnels out. This leaves the system in an optically inactive state with a double negatively charged QD (right panel). This schematic describes the experiment reported on in Ref. [72].

2.3.2 Measurement with Perturbation of the System

In this set-up, sketched in Fig. 2.5, a σ^+-pulse is applied to a single QD doped with on electron. Additionally a voltage is applied, but an asymmetric tunnel barrier prevents the electron in the conduction band of the QD from tunneling out.

If the electron is in the $|\downarrow\rangle$-state, nothing will happen, since the Pauli-exclusion principle prohibits the excitation of another $|\downarrow\rangle$-spin electron into the conduction band. If the electron spin is in the spin-$|\uparrow\rangle$ state, the pulse excites an electron-hole pair ($|\uparrow\rangle \rightarrow |\uparrow\downarrow\Uparrow\rangle$). Due to the applied voltage, the hole tunnels out of the QD. After that the QD is charged with two electrons ($|\uparrow\downarrow\Uparrow\rangle \rightarrow |\uparrow\downarrow\rangle$) and becomes optically inactive, since the Pauli exclusion principle prevents any more electrons being excited. If the electron is in the spin-$|\downarrow\rangle$ state, the σ^+-pulse has no effect, since the Pauli principle does not allow the creation of another $|\downarrow\rangle$-electron. The state of the spin at the time of the pulse can then be inferred via measuring the charge of the QD.

Chapter 3

Model

In order to model the spin dynamics of electrons trapped in QDs adequately, we need to establish which interactions and physical properties play a dominant role in the QD system. The goal of this chapter is to obtain a Hamiltonian H that incorporates all pertinent interactions and to discuss realistic values for all parameters entering the theory.

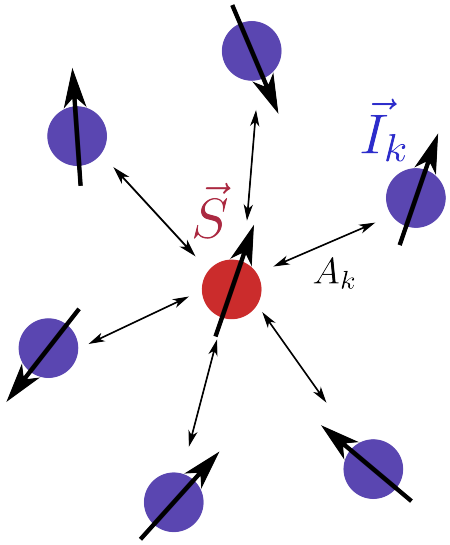

Figure 3.1: The central spin model: A central spin $\vec{S}$ interacting with a bath of nuclear spins $\vec{I}_k$ via the hyperfine interaction couplings A_k.

3.1 Hyperfine Interaction and Zeeman Splitting

In this section, the hyperfine interaction of the electron or hole with the bath of nuclear spin is analyzed. We start out with a system containing one charge carrier (electron or hole) moving in the magnetic field of one static nucleus. The derivation in this chapter shows that the electron-nucleus interaction is governed by the Fermi-contact interaction, while for hole spins only the dipole-dipole interaction is non-vanishing.

Due to the high localization of the electron in the QD the hyperfine interaction between a carrier with a spin $\vec{S}$ and the surrounding nuclei becomes dominant in the system. Fermi [30] derived the hyperfine splitting of a non-relativistic nucleus interacting with a relativistic carrier using a perturbative approach. A non-relativistic derivation can be found by examining a carrier with the spin $\vec{S}$ and the charge e, interacting with the magnetic moment $\vec{\mu}$ of a single nucleus with the nuclear spin $\vec{I}$ [83]. We describe the magnetic properties of the nucleus

as those of a magnetic dipole $\vec{\mu} = \gamma_N \vec{I}$, with γ_N being the gyromagnetic moment of the nucleus with the spin $\vec{I}$. The vector potential $\vec{A} = (\vec{\mu} \times \vec{r})/r^3 = \vec{\nabla} \times (\vec{\mu}/r)$ is generated by the magnetic moment $\vec{\mu}$, and the magnetic field can in turn be expressed via the vector potential $\vec{H} = \vec{\nabla} \times \vec{A}$. Both the interaction of the carrier spin with the magnetic field as well as the carrier dynamics are described by the Hamiltonian

$$\mathcal{H} = \frac{1}{2m_e} \left(\vec{p} + e\vec{A} \right)^2 + 2\mu_\mathrm{B} \vec{S} \cdot (\vec{\nabla} \times \vec{A}). \tag{3.1.1}$$

In first order perturbation theory we retain only those terms linear in $\vec{A}$ and obtain the Hamiltonian

$$\mathcal{H}_1 = 2\mu_\mathrm{B}\gamma_N \frac{\vec{l} \cdot \vec{I}}{r^3} + 2\mu_\mathrm{B}\gamma_N \vec{S} \cdot \vec{\nabla} \times \left(\vec{\nabla} \times \left(\frac{\vec{I}}{r} \right) \right) + \mathcal{O}(\vec{A}^2). \tag{3.1.2}$$

Here, μ_B is Bohr's magneton, $\vec{r}$ is the position of the electron in relation to the nucleus and $\vec{l}$ is the orbital momentum $\vec{l} = \vec{r} \times \vec{p}$ of the electron. The Hamiltonian can be rewritten as

$$\mathcal{H}_1 = 2\mu_\mathrm{B}\gamma_N \vec{I} \cdot \left(\frac{\vec{l}}{r^3} - \frac{\vec{S}}{r^3} + 3\frac{\vec{r} \cdot (\vec{S} \cdot \vec{r})}{r^5} + \frac{8}{3}\pi \vec{S}\delta(\vec{r}) \right). \tag{3.1.3}$$

The first three terms describe the dipole-dipole interaction $\mathcal{H}_{dd}$, while the last is the Fermi-contact interaction, as it only contributes at the location of the nucleus. We define the vector operator

$$\vec{H}_e = -2\mu_\mathrm{B} \left(\frac{\vec{l}}{r^3} - \frac{\vec{S}}{r^3} + 3\frac{\vec{r} \cdot (\vec{S} \cdot \vec{r})}{r^5} + \frac{8}{3}\pi \vec{S}\delta(\vec{r}) \right) \tag{3.1.4}$$

that describes the magnetic field produced by the electron at the nucleus and write

$$\mathcal{H}_1 = -\gamma_N \vec{H}_e \cdot \vec{I}. \tag{3.1.5}$$

We want to express the Hamiltonian as

$$\mathcal{H}_1 = c_j \vec{j} \cdot \vec{I}. \tag{3.1.6}$$

with $\vec{j}$ being the total angular momentum $\vec{j} = \vec{l} + \vec{S}$ of the electron. Comparing the expectation values $\langle c_j \vec{j} \cdot \vec{j} \rangle$ and $\langle -\gamma_N \vec{H}_e \cdot \vec{j} \rangle$ for a s-type electron, only the Fermi-contact interaction term remains and we obtain

$$c_j = \frac{16}{3}\pi \mu_B \gamma_N |\psi_e(0)|^2. \tag{3.1.7}$$

Here $\psi_e(\vec{r})$ is the wave function of the electron.

While the electron in the conduction band of the QD is s-like, holes in the valence band can be described by a p-type wave function. For $l > 0$ only the dipole-dipole term contributes, since orbitals with $l > 0$ vanish at $\vec{r} = 0$.

The z axis is aligned to [001], the growth direction of the QD. In the bases of heavy holes ($S = 3/2$, $S_z = \pm 3/2$) and light holes ($S = 3/2$, $S_z = \pm 1/2$), the dipole-dipole contribution to the Hamiltonian from eq. (3.1.3) can be expressed as [34]

$$(\mathcal{H}_{\mathrm{dd}})_{\mathrm{hh}} = \frac{8}{5}\mu_B\gamma_N\Omega|\psi_e(0)|^2\left\langle\frac{1}{r^3}\right\rangle\begin{pmatrix} I_z & 0 \\ 0 & -I_z \end{pmatrix} \tag{3.1.8}$$

for heavy holes (hh) and

$$(\mathcal{H}_{\mathrm{dd}})_{\mathrm{lh}} = \frac{8}{15}\mu_B\gamma_N\Omega|\psi_e(0)|^2\left\langle\frac{1}{r^3}\right\rangle\begin{pmatrix} I^z & -2(I^x - iI^y) \\ -2(I^x + iI^y) & -I^z \end{pmatrix} \tag{3.1.9}$$

for light holes (lh). Ω is the volume of the semi-conductor's unit cell containing two atoms. Introducing a spin-1/2 pseudo-spin $\vec{S}_{\mathrm{h}}$, the dipole-dipole coupling can, therefore, be rewritten as

$$(\mathcal{H}_{\mathrm{dd}})_{\mathrm{hh}} = \frac{16}{5}\mu_B\gamma_N\Omega|\psi_e(0)|^2\left\langle\frac{1}{r^3}\right\rangle I^z S^z_{\mathrm{h}} \tag{3.1.10}$$

for heavy holes and

$$(\mathcal{H}_{\mathrm{dd}})_{\mathrm{lh}} = \frac{16}{15}\mu_B\gamma_N\Omega|\psi_e(0)|^2\left\langle\frac{1}{r^3}\right\rangle (S^z_{\mathrm{h}}I^z - 2[S^x_{\mathrm{h}}I^x + S^y_{\mathrm{h}}I^y]) \tag{3.1.11}$$

for light holes.

Expanding the system from the interaction between an electron or hole with one nucleus at $\vec{r} = 0$ to an electron or hole interacting with N nuclei at the locations $\vec{R}_k$, the total Hamiltonian reads

$$\mathcal{H}_{\mathrm{hf}} = \sum_{k=1}^{N}(\mathcal{H}_1)_k, \tag{3.1.12}$$

disregarding the dipole-dipole interaction between the nuclear spins. For electrons this results in

$$\mathcal{H}_{\text{hf-contact}} = \sum_{k=1}^{N} J_k\vec{S}\vec{I}_k \tag{3.1.13}$$

with

$$J_k = \frac{16}{3}\pi\mu_B\gamma_N|\psi(\vec{R}_k)|^2, \tag{3.1.14}$$

$|\psi_e(\vec{R}_k)|^2$ being the probability of the electron found at the location of the k-th nucleus. For holes interacting with N nuclei the hyperfine interaction Hamiltonian can be written as

$$\mathcal{H}_{\mathrm{hh}} = \sum_{k=1}^{N} C_k S^z_h I^z_k \tag{3.1.15}$$

$$\mathcal{H}_{\mathrm{lh}} = \sum_{k=1}^{N} \frac{C_k}{3}(S^z_{\mathrm{h}}I^z - 2[S^x_{\mathrm{h}}I^x + S^y_{\mathrm{h}}I^y]) \tag{3.1.16}$$

with

$$C_k = \Omega \frac{16\mu_B}{5} \gamma_N \left\langle \frac{1}{r^3} \right\rangle |\psi_e(\vec{R}_k)|^2. \tag{3.1.17}$$

Both in the electron and the hole case, nuclei are assumed to have identical gyromagnetic moments $\gamma_N = \mu_N/I$. In reality, this is not necessarily the case. In an InGaAs QD both Gallium and Arsenide nuclei have $I = 3/2$, while Indium nuclei carry spin $I = 9/2$. The electron wave function $\psi_e(\vec{r})$ of a periodic state in a QD can be written, using the Bloch theorem, as a product $\psi_e(\vec{r}) = u(\vec{r})\psi(\vec{r})$ of the Bloch amplitude $u(\vec{k})$ and the envelope function $\psi(\vec{r})$. The Bloch amplitude is periodic in the crystal lattice and has its maxima at the positions of the nuclei in the unit cells, where typical values of $\eta_k = |u(\vec{R}_k)|^2$ are in the order $10^3 - 10^4$ [27]. While this varies among individual nuclei, we again treat all nuclei equally and set $\eta_k = 1$. This assumption does not influence the character of the dynamics of the system and influences only the time scale. Since it is not the goal to give a realistic value of the energy scale of the hyperfine coupling, this approach is valid. Later we will introduce a time scale T^*, governing the decay stemming from the hyperfine interaction, as a characteristic time unit of the system. Experimental data allows us to obtain a realistic value for T^* and compare our theoretical findings to the experiments. The envelope function $\psi(\vec{r})$ describes how the electron is positioned in the QD and influences the distribution function of the hyperfine coupling constants J_k and C_k.

All these considerations lead us to define the anisotropic hyperfine interaction Hamiltonian

$$\mathcal{H}_{\text{hf}} = \sum_{k=1}^{N} A_k \left(I_k^z S^z + \frac{1}{\lambda}[S^x I^x + S^y I^y] \right) \tag{3.1.18}$$

with λ being the anisotropy factor. To make the connection with the Hamiltonians in eqs. (3.1.13), (3.1.15) and (3.1.16), this factor is $\lambda = 1$ for electrons, $\lambda = \frac{1}{2}$ for light holes and $\lambda \to \infty$ for heavy holes. Since hole states often exist in a superposition between heavy and light hole states [34], a value of λ between $\frac{1}{2}$ and ∞ can be used to describe this. For electrons, the prefactor $A_k = J_k$, for heavy and mixed holes $A_k = C_k$, while for light holes the prefactor assumes $A_k = C_k/3$.

In the isotropic case, the magnetic field caused by the nuclear spin bath acting on the electron

$$\vec{B}_N = \sum_{k=1}^{N} A_k \vec{I}_k \tag{3.1.19}$$

is called the Overhauser field. In the anisotropic case the scalar A_k would have to be replaced by a tensor. The Overhauser field dynamic is much slower than the central spin dynamic, hence the electron spin can be described as precessing in a static Overhauser field in short time periods [31].

Symmetric to the Overhauser field, the nuclear spin $\vec{I}_k$ can be described as precessing in the magnetic field generated by the carrier, the Knight field $A_k\vec{S}$.

While the A_k for electrons and holes have different physical backgrounds, both are governed by the probability of the electron being measured at the location of the k-th nuclei $|\psi(\vec{R}_k)|$. Independently of the nature of the carrier spin, the A_k can be written as

$$A_k = A_s\Omega|\psi(\vec{R}_k)|^2 \tag{3.1.20}$$

where the prefactor A_s can be deduced by comparison with the coupling constants defined in Eqs. (3.1.13), (3.1.15) and (3.1.16). $|\psi(\vec{R}_k)|^2$ is a probability function and, therefore, normal. If we assume that the volume of one unit cell Ω is very small compared to the volume of the QD and that $|\psi(\vec{R}_k)|^2$ can be considered constant within one unit cell, we can write

$$1 = \int \mathrm{d}V|\psi(\vec{r})|^2 \approx \Omega\sum_{k=1}^{N}|\psi(\vec{R}_k)|^2. \tag{3.1.21}$$

It follows from Eqs. (3.1.20) and (3.1.21) that the prefactor A_s is

$$A_s = \sum_{k=1}^{N} A_k \tag{3.1.22}$$

an energy scale that describes the total energy of the hyperfine interaction in the system. Because of the normalization condition of the probability function $|\psi(\vec{R}_k)|^2$, A_s is independent of the coupling constant distribution. Usually, A_s is in the order of $\mathcal{O}(10\,\mu\mathrm{eV})$ for electrons [21, 35] and $\mathcal{O}(1\,\mu\mathrm{eV})$ for holes [34]. The Hamiltonian in Eq. (3.1.18) completely describes the hyperfine interaction

	I	μ/μ_N	$\gamma_\mathrm{N}/\mu_\mathrm{N}$	$\gamma_\mathrm{N}/\mu_\mathrm{B}$
^{75}As	3/2	1.439	0.959	5.22×10^{-4}
^{69}Ga	3/2	2.015	1.343	7.31×10^{-4}
^{71}Ga	3/2	2.560	1.709	9.31×10^{-4}
^{115}In	9/2	5.535	1.230	6.70×10^{-4}

Table 3.1: Magnetic moments and gyromagnetic ratios found in InGaAs QDs [84].

between an electron or hole spin with a bath of nuclear spins. However, in most experiments an external magnetic field is applied to the sample, which acts on both the carrier spin and the nuclear spins. Incorporating an externally applied magnetic field $\vec{B}$ into our model results in the Hamiltonian

$$\mathcal{H}_\mathrm{CSM} = g\mu_\mathrm{B}\vec{S}\vec{B} + \gamma_\mathrm{N}\sum_{k=0}^{N}\vec{I}^k\vec{B} + \sum_{k=1}^{N}A_k\left(I_k^zS^z + \frac{1}{\lambda}[S^xI^x + S^yI^y]\right). \tag{3.1.23}$$

Again it is assumed that all nuclear spins are identical, in that they share gyromagnetic ratio γ_N, and thus exhibit the same strength of Zeeman splitting $\gamma_\mathrm{N}|\vec{B}|$.

While the g-factor of a free electron is $g_e \approx 2$, localized in an InGaAs QD $g_e = 0.54$ has been measured [55]. The g-factor varies between electron and holes, with the hole g-factor in InGaAs being $g_h = 0.16$ [55]. μ_B is the Bohr magneton. Due to the difference in mass, the Zeeman splitting of the nuclei is significantly smaller than the Zeeman splitting of the electron, the nuclear magneton $\mu_N = e/2m_p$, with m_p being the proton mass, is by a factor of $\mu_B/\mu_N = 1836.109$ smaller than the Bohr magneton $\mu_B = e/2m_e$. Examples for gyromagnetic ratios of the common isotopes in InGaAs QD are given in Tab. 3.1. Because the nuclear Zeeman splitting is about three orders of magnitude smaller than the electronic Zeeman splitting, it is often neglected. However, in large external magnetic fields the nuclear Zeeman splitting enters the same order of magnitude as the hyperfine interaction and the later discussed quadrupolar coupling and can, therefore, no longer be neglected. The ratio between the electron Zeeman splitting and the nuclear Zeeman splitting will in the following be defined as

$$\zeta = \frac{\gamma_N}{g\mu_B}. \tag{3.1.24}$$

3.2 Quadrupolar Coupling

The growth process of QDs, that in the case of molecular beam epitaxy relies on a mismatch of lattice constants between growth layers, can lead to lattice strain. Lattice strain causes the emergence of electric field gradients in the QD, which couple to the nuclear spins. The nuclear spin translates to a prolate nuclear charge distribution, which presents a nuclear quadrupole moment Q, see Fig. 3.2.

In deriving the quadrupole Hamiltonian one starts with describing the Coulomb interaction between the charge distribution $\rho_n(r_n)$ of one nucleus and $\rho_e(r_e)$ of the electrons around the nucleus and expands this expression up to quadrupole order. The Wigner-Eckart theorem makes it possible to describe the interaction

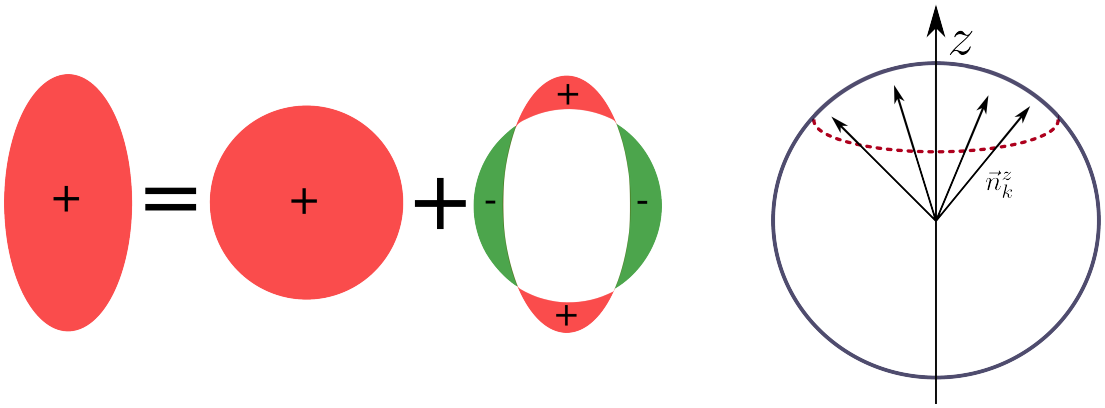

Figure 3.2: Left: A prolate nuclei can be described by a spherical and a quadrupolar charge distribution. Right: Randomly selecting the quadrupolar orientation vector $\vec{n}_k^z$ within a cone around the optical z axis [81, 85].

between two charge distributions as the interaction between the nuclear spin $\vec{I}$ and the classic electrostatic potential $V(r_n)$ produced by the electrons at the location of the nucleus. In the end, the quadrupole Hamiltonian describing the interaction of one nucleus and the electron cloud can be derived [83, 86] to be

$$\mathcal{H}_{\text{Quad, e-n}} = \frac{eV_{zz}Q}{4I(2I-1)}\left\{3I_z^2 - I(I+1) + \frac{\eta}{2}(I_+^2 + I_-^2)\right\}, \tag{3.2.1}$$

where the spin is quantified along the easy axis. $I_+ = I^x + iI^y$ and $I_- = I^x - iI^y$ are the spin ladder operators of the nuclear spin. The anisotropy factor $\eta = (V_{xx} - V_{yy})/V_{zz}$ corresponds to the axial symmetry of the system. Here, as the coordinate axes x, y and z we choose to use the principal axes of the electric field gradient

$$V_{ij} = \frac{\partial^2 V}{\partial x_i \partial x_j}, \tag{3.2.2}$$

so that the non-diagonal elements of V_{ij} amount to zero. In order to describe a bath of N nuclei with a nuclear spin length I, one has to consider that V_{ij} differs for each nucleus. Therefore we define $\vec{n}_k^x$, $\vec{n}_k^y$ and $\vec{n}_k^z$ as the principal axis of the Hesse-matrix V_{ij} of the electrostatic potential $V(\vec{R}_k)$ at the k-th nucleus. These are called the quadrupolar orientation vectors. This allows us to write the quadrupole Hamiltonian of the whole bath as

$$\mathcal{H}_Q = \sum_{k=1}^{N} \tilde{q}_k \left((\vec{I}_k \vec{n}_k^z)^2 - \frac{I(I+1)}{3} + \frac{\eta}{3}(\vec{I}_k \vec{n}_k^x)^2 - \frac{\eta}{3}(\vec{I}_k \vec{n}_k^y)^2 \right) \tag{3.2.3}$$

with

$$\tilde{q}_k = \frac{3eQ_k}{4I(2I+1)} V_{zz}^k \tag{3.2.4}$$

being the strength of the quadrupolar interaction of the k-th nucleus. In eq. (3.2.3) the base was transformed from the sum of the electrons interactions with each spin. $\mathcal{H}_Q$ only yields non-zero contributions if the nuclear spins are $I > 1/2$. In fact it can be shown [83] that a nucleus with a spin I will only have non-vanishing moments of the order $l \leq 2I+1$. This means that for the nuclear spins of Ga or As, where the spin length is $I = 3/2$, neglecting all moments higher than quadrupolar order is exact. Note that $\mathcal{H}_Q$ conserves time reversal symmetry [59], contrary to simplified approaches to modelling quadrupolar interaction by a random magnetic field and $I = 1/2$ [61].

There are several different parameters governing the behaviour of the quadrupolar interaction: (i) The anisotropy factor η is often neglected, but has been found to be $\eta \approx 0.5$ in self assembled QDs [87], which is the parameter setting we will use in the following. (ii) The quadrupolar orientation axes $\vec{n}_k^z$ that have been reported to be at a mean deviation angle of $\overline{\theta} = 23°$ for an $In_{0.4}Ga_{0.6}As$ QD [87] with the z axis. This mean angle can be reproduced numerically by generating

isotropically distributed vectors and discarding any vector at an angle larger than $\theta_{\max} = 34°$. The remaining basis vectors $\vec{n}_k^x$ and $\vec{n}_k^y$ are then chosen to create an orthonormal base. iii) The quadrupolar coupling constants of the nuclei, $\tilde{q}_k$, are randomly generated from a unitary distribution with $\tilde{q}_k \in [0.5 : 1]$.

All these parameters are influenced by the growth process and can vary strongly between samples. Previous works [59,85] showed that choosing the parameters as specified above results in the correct prediction of experimental data for second-order correlation functions in InAsGa QD.

3.3 Characteristic Time Scale

The second-order correlation function $\langle S_z(t)S_z\rangle$ decays on a time scale characteristic to the QD, in the absence of a magnetic field and quadrupolar coupling. One can expand the second-order correlation in time by expressing the time evolution with a Taylor series with the Hamiltonian H, yielding

$$\begin{aligned}\langle S_z(t)S_z\rangle &= \langle \mathrm{e}^{\mathrm{i}Ht} S_z \mathrm{e}^{-\mathrm{i}Ht} S_z\rangle \\ &= \langle \sum_n \frac{(\mathrm{i}Ht)^n}{n!} S_z \sum_m \frac{(-\mathrm{i}Ht)^m}{m!} S_z\rangle \\ &= \langle S_z S_z\rangle + \mathrm{i}t\,\langle [H,S_z]S_z\rangle - \frac{t^2}{2}\langle [H,[H,S_z]]S_z\rangle + \mathcal{O}(t^3).\end{aligned} \tag{3.3.1}$$

If we go to the high temperature limit and regard all states as equally occupied in an unpumped system ($\rho = \mathbf{1}/D$, with D being the dimension of the Hilbert space), the term linear in t vanishes, and $\langle S_z(t)S_z\rangle$ can be written as

$$\langle S_z(t)S_z\rangle = \frac{1}{4} - \frac{t^2}{8\lambda^2}\sum_{k=1}^{N} A_k^2\,\langle I_k^x I_k^x + I_k^y I_k^y\rangle + \mathcal{O}(t^3). \tag{3.3.2}$$

At $t = 0$, the nuclear spins are not correlated with the electron and are isotropic in their average orientation, due to the absence of an external magnetic field. Therefore we can assume that $\langle I_k^i I_k^i\rangle = I(I+1)/3$ with $i = x, y, z$. This leads us to the expression

$$\langle S_z(t)S_z\rangle = \frac{1}{4} - \left(\frac{t}{4T^*}\right)^2 + \mathcal{O}(t^3) \tag{3.3.3}$$

where we introduce the characteristic time scale

$$T^* = \lambda\sqrt{\frac{3}{4I(I+1)}\frac{1}{\sum A_k^2}} = \frac{1}{\omega_{\mathrm{fluc}}}. \tag{3.3.4}$$

We see that in the first non-vanishing order the central spin dynamics is governed by the characteristic time scale T^*. In the isotropic case the characteristic time

scale is inversely proportional to

$$\sqrt{\langle \vec{B}_N^2 \rangle} = \sqrt{I(I+1)\sum_{k=1}^{N} A_k^2} \tag{3.3.5}$$

the fluctuation frequency of the Overhauser field. Note that for heavy holes, the anisotropy factor $\lambda \to \infty$, and the characteristic time scale is no longer applicable. Having defined the characteristic time scale T^* allows us to define the characteristic energy scale $\omega_{\text{fluc}} = 1/T^*$ as its inverse. In the following, we will use the dimensionless central spin model Hamiltonian

$$H_{\text{CSM}} = T^* \mathcal{H}_{\text{CSM}} = \vec{b}\vec{S} + \zeta \sum_{k=1}^{N} \vec{I}_k \vec{b} + \sum_{k=1}^{N} a_k \left(I_k^z S^z + \frac{1}{\lambda}[S^x I^x + S^y I^y] \right) \tag{3.3.6}$$

with the dimensionless hyperfine coupling constants $a_k = T^* A_k$, the Zeeman splitting ratio $\zeta = \gamma_N / g\mu_{\text{B}}$ and the dimensionless external magnetic field $\vec{b} = T^* g \mu_{\text{B}} \vec{B}$.

The dimensionless Hamiltonian of the quadrupolar interaction $H_Q = T^* \mathcal{H}_Q$ is defined in a similar manner

$$H_Q = \sum_{k=1}^{N} q_k \left((\vec{I}_k \vec{n}_k^z)^2 - \frac{I(I+1)}{3} + \frac{\eta}{3}(\vec{I}_k \vec{n}_k^x)^2 - \frac{\eta}{3}(\vec{I}_k \vec{n}_k^y)^2 \right). \tag{3.3.7}$$

In order to compare the strength of the hyperfine interaction with the quadrupolar interaction strength, we introduce the ratio

$$Q_r = \frac{\sum_k q_k}{\sum_k a_k} \tag{3.3.8}$$

which will be used in the following to quantify the interaction strength. The dimensionless quadrupolar coupling constants q_k can be obtained through

$$q_k = Q_r \tilde{q}_k \frac{\sum_k a_k}{\sum_k \tilde{q}_k} \tag{3.3.9}$$

to fulfil Eq. (3.3.8).

Chapter 4

Cumulants and Correlation Functions

Cumulants and correlation functions are highly useful mathematical concepts that have application in numerous fields. They can, for instance, be employed in diagrammatic perturbation theory to describe correlation in the Anderson lattice with Coulomb repulsion [88, 89]. Correlation functions appear as two-particle Greens functions in dynamical mean field theory on non-local correlation in the Hubbard model [90–92]. In the full counting statistics cumulants are used to describe shot noise and charge fluctuation [93, 94]. In the CSM, second-order spin correlations have likewise been widely studied [57–59, 61, 95–97].

Correlation functions are used to quantify the correlation between the measurands of two or more operators. The amount of operators whose interdependence the correlation function describes gives the order of the correlation function. An auto-correlation function, which describes the correlation of a measurand with itself at different times (for example the spin polarization at the beginning of the measurement and some time later) can be used to evaluate the decay of an initialized measurand in a system. In a static system the auto-correlation function of any measurand will always be constant, as no information is lost. Compare this to a very noisy system, where any information that has been put into the system, for example through pumping a spin into a specific state, will decay quickly. The Fourier transformation of the correlation function is called noise.

Higher order spin correlators link measurands at several times (or in the case of higher order noise, frequencies). Therefore it is possible that they contain additional information compared to the second order, which makes them an interesting object to study.

This work focuses on correlation functions and noise of an electron spin interacting with a nuclear spin bath. While the main focus here are fourth-order correlators, second-order spin correlation will also be investigated in order to compare the results to experimental findings and thus to find realistic values for the parameters of the system.

In this chapter the correlators studied in this thesis are defined. The corresponding experiments are discussed as well as the fourth-order correlators derived by measurement theory if necessary.

4.1 Cumulant Theory

Cumulants are a widely applicable mathematical tool that plays an important role in probability theory, and is crucial in quantum mechanics as well as in thermodynamics [98]. The cumulant generating functional

$$K(\xi) = \log \left\langle e^{\xi X} \right\rangle \tag{4.1.1}$$

with some parameter ξ_i and the random variable X is linked to the exponentiated series of the n-th order cumulant κ_n via

$$K(\xi) = \sum_{n=1}^{\infty} \frac{\xi^n}{n!} \kappa_n. \tag{4.1.2}$$

This observation had a profound impact for analysis of noise [99] as well as diagrammatic perturbation theory. The first cumulant of a set of random variables is the mean

$$\kappa_1 = \langle X \rangle_c = \langle X \rangle . \tag{4.1.3}$$

The subscript c refers to the cumulant average. The second-order cumulant of two variables X_1 and X_2 is defined as

$$\langle X_1 X_2 \rangle_c = \langle X_1 X_2 \rangle - \langle X_1 \rangle \langle X_2 \rangle \tag{4.1.4}$$

and is identical to $\langle X_1 X_2 \rangle$ if either X_1 or X_2 have a mean equal to zero. This can be systematically extended to higher order cumulants [98], such as the third-order cumulant

$$\begin{aligned} \langle X_1 X_2 X_3 \rangle_c = &\langle X_1 X_2 X_3 \rangle - \langle X_1 X_2 \rangle \langle X_3 \rangle - \langle X_2 X_3 \rangle \langle X_1 \rangle + \langle X_1 X_3 \rangle \langle X_2 \rangle \\ &+ 2 \langle X_1 \rangle \langle X_2 \rangle \langle X_3 \rangle \end{aligned} \tag{4.1.5}$$

and the fourth-order cumulant

$$\begin{aligned} \langle X_1 X_2 X_3 X_4 \rangle_c = &\langle X_1 X_2 X_3 X_4 \rangle - \langle X_1 \rangle \langle X_2 X_3 X_4 \rangle - \langle X_2 \rangle \langle X_1 X_3 X_4 \rangle \\ &- \langle X_3 \rangle \langle X_1 X_2 X_4 \rangle - \langle X_4 \rangle \langle X_1 X_2 X_3 \rangle - \langle X_1 X_2 \rangle \langle X_3 X_4 \rangle \\ &- \langle X_1 X_3 \rangle \langle X_2 X_4 \rangle - \langle X_1 X_4 \rangle \langle X_2 X_4 \rangle + 2 \langle X_1 \rangle \langle X_2 \rangle \langle X_3 X_4 \rangle \\ &+ 2 \langle X_1 \rangle \langle X_3 \rangle \langle X_2 X_4 \rangle + 2 \langle X_1 \rangle \langle X_4 \rangle \langle X_2 X_3 \rangle + 2 \langle X_2 \rangle \langle X_3 \rangle \langle X_1 X_4 \rangle \\ &+ 2 \langle X_2 \rangle \langle X_4 \rangle \langle X_1 X_3 \rangle + 2 \langle X_3 \rangle \langle X_4 \rangle \langle X_1 X_2 \rangle - 6 \langle X_1 \rangle \langle X_2 \rangle \langle X_3 \rangle \langle X_4 \rangle . \end{aligned} \tag{4.1.6}$$

As can be seen in Eqs. (4.1.4), (4.1.5) and (4.1.6), the n-th order cumulant is given by the n-th order auto-correlation function from which all Gaussian noise is subtracted [98]. This separates the true higher order correlations from a trivial factorisation. If a system would be fully characterized by Gaussian noise, all higher order cumulants would be vanishing [99]. Using cumulants, we can discern true correlation from randomness.

4.2 High Temperature Limit

The quantum mechanical expectation value of an operator O is defined as

$$\langle O \rangle = \mathrm{Tr}[\rho O] \tag{4.2.1}$$

with ρ being the density operator of the system. In equilibrium, the density operator is given by the Boltzmann distribution

$$\rho_{\mathrm{eq}} = \frac{1}{Z} e^{-\beta H}. \tag{4.2.2}$$

H is the system Hamiltonian, $\beta = 1/k_B T$ the inverse of the thermal energy, the product of the temperature T and the Boltzmann constant k_B. Z denotes the partition function

$$Z = \mathrm{Tr}[e^{-\beta H}]. \tag{4.2.3}$$

Spin noise experiments in semi-conductor QDs are usually performed at around $T = 5\,K$, which translates to a thermal energy $k_B T = 431\,\mu\mathrm{eV}$. The fluctuation frequency of the Overhauser field is, depending on the QD, around $\omega_{\mathrm{fluc}} = 10^9\,1/\mathrm{s}$ [35], which gives the characteristic energy scale of the system $\hbar\omega_{\mathrm{fluc}} = 0.7\,\mu\mathrm{eV}$. With the thermal energy being approximately 650 times higher than the systems characteristic energy scale, it is justified to apply the limit $T \to \infty$. The equilibrium density operator then becomes $\rho_{\mathrm{eq}} = \mathbb{1}/D$, as all states are equally occupied. D is the dimension of the Hilbert space.

If very high external magnetic fields are applied, the high temperature limit may not be valid. At a magnetic field strength of $B_{\mathrm{ext}} = 13.5\,\mathrm{T}$ the thermal energy $k_B T$ and the electronic magnetic energy $g_e \mu_B B_{\mathrm{ext}}$ become equal. Since the magnetic fields considered in this thesis remain far below this, the high temperature limit will be used throughout.

4.3 Second-Order Correlation Function and Noise

Due to the high temperature limit causing all states to be equally occupied, we can neglect the equilibrium spin polarization $\langle S_z \rangle$. This leads the second-order spin-spin auto-correlation function

$$\tilde{C}_2(t_1, t_2) = \langle S_z(t_1) S_z(t_2) \rangle \tag{4.3.1}$$

to be identical to its cumulant $\langle S_z(t_1) S_z(t_2) \rangle_c$. It describes the correlation between the z component of the spin at the start of the measurement t_1 and at time t_2.

We also assume that the system is in equilibrium, which means that the Hamiltonian commutes with the density operator. Since the system is translationally invariant in time, the correlation function only depends on the relative time $\tau = t_1 - t_2$. It can also be written as

$$C_2(\tau) = \langle S_z(\tau) S_z(0) \rangle. \tag{4.3.2}$$

For systems that are translationally invariant in time one time variable can always be eliminated in higher order correlation [99] in favour of relative time coordinates. Therefore, the n-th order correlation function only depends on $n-1$ time variables.

The second-order spin correlation function $C_2(\tau)$ describes the correlation between the z-component of the spin at the start of the measurement and at time t. In a typical pump-probe experiment, the spin is initialized at $t = 0$ in one state, and then left to decay while being simultaneously measured via Faraday rotation. The density operator caused by the initialisation, for example into the $|\uparrow\rangle$-state, can be described by $\rho_{\text{initial}} = 2P_\uparrow/D$, $P_\uparrow$ being the projection operator into the $|\uparrow\rangle$-state. Therefore, the polarization can be written as

$$S(t) = \frac{2}{D}\mathrm{Tr}[P_\uparrow S_z(t)]. \tag{4.3.3}$$

Since $P_\uparrow = 1/2 + S_z$ and all spin matrices are traceless, the polarization yields

$$S(t) = 2\langle S_z(t)S_z\rangle = 2C_2(t) \tag{4.3.4}$$

in the high temperature limit. The polarization along the z axis that is measured by Faraday rotation is thus directly equitable with the second-order correlation function.

This work will analyze correlators both in the frequency domain and in the time domain. In order to access the frequency information for spin correlation functions, we introduce the Fourier transform of the spin operator S_z,

$$a(\omega) = \frac{1}{\sqrt{T_m}}\int_{-T_m/2}^{T_m/2} \mathrm{d}t\, e^{-\mathrm{i}\omega t} S_z(t), \tag{4.3.5}$$

defined over the measurement time T_m starting at $t_0 = -T_m/2$. The spin noise is defined as the Fourier transform of $C_2(\tau) = \langle S_z(\tau)S_z(0)\rangle$

$$C_2(\omega) = \int_{-\infty}^{\infty} d\tau \langle S_z(\tau)S_z(0)\rangle e^{-i\omega\tau}. \tag{4.3.6}$$

The steady-state spin auto-correlation $\langle a(\omega_1)a(\omega_2)\rangle$ is related to the spin noise power spectrum via the Wiener-Chintchin theorem [46, 100]. It requires that the measuring time T_m is much longer than the characteristic time scale of the spin decay T^* ($T_m \gg T^*$). Since the measuring time T_m is very large compared to the characteristic time scale of spin decay T^*, we perform the limit $T_m \to \infty$ to simplify the mathematical expressions. However, applying the limit can lead to divergence in expressions. Substituting the Fourier transformation (4.3.5) and using the translational invariance in time, we obtain the second-order spin correlation function in the frequency domain

$$\begin{aligned}\tilde{C}_2(\omega_1,\omega_2) =& \lim_{T_m\to\infty}\langle a(\omega_1)a(\omega_2)\rangle \\ =& \lim_{T_m\to\infty}\frac{1}{T_m}\int_{-\frac{T_m}{2}}^{\frac{T_m}{2}} dt_1\, e^{-\mathrm{i}\omega_1 t_1}\int_{-\frac{T_m}{2}}^{\frac{T_m}{2}} dt_2\, e^{-\mathrm{i}\omega_2 t_2}\langle S_z(t_1)S_z(t_2)\rangle \\ =& \delta_{\omega_1,-\omega_2}C_2(\omega).\end{aligned} \tag{4.3.7}$$

The spin-noise spectrum $C_2(\omega)$ satisfies the sum rule

$$\int_{-\infty}^{\infty} d\omega C_2(\omega) = \frac{\pi}{2}. \tag{4.3.8}$$

Note that the inclusion of the prefactor $1/\sqrt{T_m}$ into the definition of the Fourier transformation ensures the convergence of $\tilde{C}_2(\omega_1, \omega_2)$. It also leads to the Kronecker δ in the last line of Eq. (4.3.7).

4.4 Third-Order Correlation

The third-order spin correlation function

$$C_3(t_1, t_2, t_3) = \langle S_z(t_1) S_z(t_2) S_z(t_3) \rangle \tag{4.4.1}$$

will, in contrast to the second and fourth-order spin correlation, not be subject of further investigation. The reason is that C_3 is always imaginary in a system without quadrupolar interaction and an external magnetic field $\vec{B} = (B_x, 0, B_z)^T$. In this case the Hamilton matrix is symmetric and real. Diagonalisation yields the eigenvectors $|n\rangle$ and eigenvalues ϵ_n, satisfying

$$H |n\rangle = \epsilon_n |n\rangle \tag{4.4.2}$$

that are real as well. The spin operator S_z then is symmetric and real in the eigenbasis of the Hamilton matrix, $\langle n|S_z|m\rangle = \langle m|S_z|n\rangle$. $S_{nm} = \langle n|S_z|m\rangle$ is used in the following for abbreviation.

By inserting the identity

$$\mathbb{1} = \sum_n |n\rangle \langle n| , \tag{4.4.3}$$

one can rewrite the third-order correlation as

$$C_3(t_1, t_2, t_3) = \frac{1}{D} \sum_{nml} e^{\mathrm{i}(E_n - E_m)t_1} e^{\mathrm{i}(E_m - E_l)t_2} e^{\mathrm{i}(E_l - E_n)t_3} S_{nm} S_{ml} S_{ln}. \tag{4.4.4}$$

Through complex conjugation we obtain

$$\begin{aligned} C_3^*(t_1, t_2, t_3) =& \frac{1}{D} \sum_{nml} e^{-\mathrm{i}(E_n - E_m)t_1} e^{-\mathrm{i}(E_m - E_l)t_2} e^{-\mathrm{i}(E_l - E_n)t_3} S_{nm} S_{ml} S_{ln} \\ =& C_3(-t_1, -t_2, -t_3). \end{aligned} \tag{4.4.5}$$

Now, we introduce the time reversal operator T. T acts on the spin operator as

$$T^{-1} S_z(t) T = -S_z(-t). \tag{4.4.6}$$

With this, the result of Eq. (4.4.5) can be expressed as

$$\begin{aligned} C_3(-t_1,-t_2,-t_3) =& \frac{1}{D}\mathrm{Tr}[S_z(-t_1)S_z(-t_2)S_z(-t_3)] \\ =& -\frac{1}{D}\mathrm{Tr}[T^{-1}S_z(t_1)TT^{-1}S_z(t_2)TT^{-1}S_z(t_3)T] \\ =& -C_3(t_1,t_2,t_3). \end{aligned} \tag{4.4.7}$$

This means that $C_3^*(t_1,t_2,t_3) = -C_3(t_1,t_2,t_3)$, which proves that the third-order spin correlation is completely imaginary in the high temperature limit. This reasoning can be extended to any spin-auto correlation function of odd numbered order in a system that is described by a symmetric Hamilton matrix. Since C_3 is imaginary, it cannot be an observable, and is, therefore, of no further interest in this work.

4.5 Fourth-Order Spin Noise and Correlation

The second-order spin correlation has been extensively studied both in the frequency and the time domain [49,53,57]. In contrast, the properties of fourth-order correlation functions remain relatively unknown [73]. In order to separate the information already provided by C_2 from any new information that can be found in C_4, we introduce the fourth-order spin cumulant [99] of $a(\omega)$ in this section.

The fourth-order cumulant of $a(\omega)$ is defined as

$$\begin{aligned} \tilde{S}_4(\omega_1,\omega_2,\omega_3,\omega_4) =& \tilde{C}_4(\omega_1,\omega_2,\omega_3,\omega_4) \\ & - \tilde{C}_2(\omega_1,\omega_2)\tilde{C}_2(\omega_3,\omega_4) \\ & - \tilde{C}_2(\omega_1,\omega_3)\tilde{C}_2(\omega_2,\omega_4) \\ & - \tilde{C}_2(\omega_1,\omega_4)\tilde{C}_2(\omega_2,\omega_3), \end{aligned} \tag{4.5.1}$$

where we neglected the spin polarization in a finite magnetic field which is justified in the high temperature limit. The assumption of a steady state and the limit $T_m \gg T^*$ yields

$$\tilde{C}_4(\omega_1,\omega_2,\omega_3,\omega_4) = \delta_{\omega_1+\omega_2+\omega_3+\omega_4,0} C_4(\omega_1,\omega_2,\omega_3,-(\omega_1+\omega_2+\omega_3)).$$

An interesting special case of the fourth-order cumulant is the bispectrum

$$\begin{aligned} S_4(\omega_1,\omega_2) =& \tilde{S}_4(\omega_1,-\omega_1,\omega_2,-\omega_2) \\ =& C_4(\omega_1,\omega_2) - C_2(\omega_1)C_2(\omega_2) \\ & \times (1+\delta_{\omega_1,\omega_2}+\delta_{\omega_1,-\omega_2}) \end{aligned} \tag{4.5.2}$$

with $C_4(\omega_1,\omega_2) = \tilde{C}_4(\omega_1,-\omega_1,\omega_2,-\omega_2)$. $S_4(\omega_1,\omega_2)$ describes the correlation between two spin noise components at different frequencies. If the observation of a spin component with the frequency ω_1 decreases the likelihood of observing

a spin component with the frequency ω_2, $S_4(\omega_1, \omega_2)$ is going to have a negative value. In the limit $T_m \to \infty$, the last two terms in Eq. (4.5.1) are zero for $S_4(\omega_1, \omega_2)$ unless $\omega_1 = \pm\omega_2$. The bispectrum describes how power spectra at two different frequencies are correlated. Similarly to the second-order spectrum, $C_4(\omega_1, \omega_2)$ also follows a sum rule, in this case

$$\int_{-\infty}^{\infty} d\omega_1 \int_{-\infty}^{\infty} d\omega_2 C_4(\omega_1, \omega_2) = \frac{\pi^2}{4}. \tag{4.5.3}$$

Since the contributions to $S_4(\omega_1, \omega_2)$ containing $\delta_{\omega_1, \pm\omega_2}$ are infinitesimally narrow, it follows from Eqs. (4.3.8) and (4.5.3) that the integral of $S_4(\omega_1, \omega_2)$ over the $\omega_1 - \omega_2$ plane yields zero. This means that there is just as much anti-correlation as correlation in the bispectrum, since

$$\int_{-\infty}^{\infty} d\omega_1 \int_{-\infty}^{\infty} d\omega_2 C_2(\omega_1) C_2(\omega_2) = \frac{\pi^2}{4} \tag{4.5.4}$$

as well.

Similarly to the spin noise in the frequency domain, the spin correlation in real time is defined as

$$C_4(\tau_1, \tau_2, \tau_3) = \langle S_z(\tau_1) S_z(\tau_2) S_z(\tau_3) S_z(0) \rangle \tag{4.5.5}$$

where the fourth time could again be eliminated via the assumption of steady state and the introduction of relative times.

In the long measurement limit $T_m \to \infty$, the Fourier transform of $C_4(\omega_1, \omega_2)$ yields

$$\begin{aligned} \mathcal{F}C_4(\omega_1, \omega_2) =& \frac{1}{T_m} \int_{-T_m/2}^{T_m/2} d\tau \langle S_z(t_1 + \tau) S_z(\tau) S_z(t_2) S_z \rangle \\ =& \frac{1}{T_m} \int_{-T_m/2}^{T_m/2} d\tau C_4(t_1 + \tau, \tau, t_2). \end{aligned} \tag{4.5.6}$$

The integrand describes the correlation of two $C_2(t_{1/2})$ measurements with different starting times $t = 0$ and $t = \tau$, which is then averaged over the time delay between both measurements.

Chapter 5

Methods

This chapter will discuss both the analytical and numerical methods employed in this work. Section 5.1 introduces the semi-classical frozen Overhauser field approximation, which treats the nuclear spin dynamics as static and is very good at describing the systems short term dynamics. In Sec. 5.2 the box model solution is presented, where the CSM can be described exactly for an arbitrary number of spins if the hyperfine coupling constants are assumed to be homogeneous. Section 5.3 shows how second and fourth-order correlation functions can be calculated via full exact diagonalisation of the Hamilton matrix. Sec. 5.4 introduces the Lanczos method with restarts, where the correlation is computed through a numerical time propagation scheme. And lastly, a semi-classical method is presented in Sec. 5.5, employing a numerical solution of the equations of motion of the spins treated as classical magnetic moments.

5.1 Frozen Overhauser Field Approximation

The simplest way to find an analytical expression for the short time spin dynamics is via a mean field approach [31]. The nuclear spins precess at a much slower rate than the central electron spin, since the electron spin is interacting with all nuclear spins, while the nuclear spins see each only the magnetic field generated by the electron spin. For short time scales, the Overhauser field

$$\vec{B}_N = \sum_k A_k \vec{I}_k \tag{5.1.1}$$

can be treated as a frozen classical vector. This is called the frozen Overhauser field approximation (FOA). The Hamiltonian of an electron spin precessing in a static Overhauser field and external magnetic field reads as

$$H = (\vec{B}_N + \vec{B}_{\text{ext}})\vec{S} = \frac{1}{2}\vec{B}\vec{\sigma} = \frac{1}{2}\begin{pmatrix} b_3 & b_1 - \mathrm{i}b_2 \\ b_1 + \mathrm{i}b_2 & -b_3 \end{pmatrix}. \tag{5.1.2}$$

Here, $\vec{B} = \vec{B}_N + \vec{B}_{\text{ext}}$ is the total field with the components $(b_1, b_2, b_3)^T$. We change into the eigenbasis, in order to obtain the time evolution operator

$$U(t) = U_B^\dagger \text{DIAG}\left(\mathrm{e}^{\mp \mathrm{i}\omega_\mathrm{L} t/2}\right) U_B. \tag{5.1.3}$$

Diagonalization of the Hamilton matrix results in the Larmor frequency

$$\omega_\mathrm{L} = |\vec{B}| \tag{5.1.4}$$

and

$$U_B = \sqrt{\frac{|\vec{b}|^2 - b_3^2}{2|\vec{b}|}} \begin{pmatrix} \frac{1}{\sqrt{|\vec{b}|-b_3}} & \frac{1}{\sqrt{|\vec{b}|+b_3}} \\ \frac{\sqrt{|\vec{b}|-b_3}}{b_1 - ib_2} & -\frac{\sqrt{|\vec{b}|+b_3}}{b_1 - ib_2} \end{pmatrix}. \tag{5.1.5}$$

Any spin operator can always be expanded in a linear combination of Pauli spin matrices,

$$S_z(t) = U^\dagger(t) S_z U(t) = \vec{c}(t)\vec{\sigma} \tag{5.1.6}$$

with the time dependent vector $\vec{c}(t) = (c_1(t), c_2(t), c_3(t))^T$ being

$$c_1(t) = \frac{b_3\sqrt{|b|^2 - b_3^2}}{2|b|^2}(1 - \cos(\omega_\mathrm{L} t)) \tag{5.1.7}$$

$$c_2(t) = \frac{\sqrt{|b|^2 - b_3^2}}{2|b|} \sin(\omega_\mathrm{L} t)) \tag{5.1.8}$$

$$c_3(t) = \frac{b_3^2}{2|b|^2} + \frac{|b|^2 - b_3^2}{2|b|^2} \cos(\omega_\mathrm{L} t). \tag{5.1.9}$$

The vector algebra relation

$$(\vec{a}\vec{\sigma})(\vec{b}\vec{\sigma}) = (\vec{a}\vec{b})\mathbb{1} + \mathrm{i}(\vec{a} \times \vec{b})\vec{\sigma} \tag{5.1.10}$$

is used to obtain the second-order spin correlation

$$\begin{aligned} C_2(t_1 - t_2) =& \langle S_z(t_1) S_z(t_2)\rangle \\ =& \frac{1}{Z}\text{Tr}\left((\vec{c}(t_1)\vec{\sigma})(\vec{c}(t_2)\vec{\sigma})\right) \\ =& \vec{c}(t_1)\vec{c}(t_2) \end{aligned} \tag{5.1.11}$$

as well as the fourth-order spin correlation

$$\begin{aligned} \langle S_z(t_1)S_z(t_2)S_z(t_3)S_z(t_4)\rangle =& \frac{1}{Z}\text{Tr}\left((\vec{c}(t_1)\vec{\sigma})(\vec{c}(t_2)\vec{\sigma})(\vec{c}(t_3)\vec{\sigma})(\vec{c}(t_4)\vec{\sigma})\right) \\ =& (\vec{c}(t_1)\vec{c}(t_2))(\vec{c}(t_3)\vec{c}(t_4)) - (\vec{c}(t_2)\vec{c}(t_4))(\vec{c}(t_1)\vec{c}(t_3)) \\ &+ (\vec{c}(t_1)\vec{c}(t_4))(\vec{c}(t_2)\vec{c}(t_3)). \end{aligned} \tag{5.1.12}$$

For the second-order correlation one can easily derive

$$C_2(t) = \frac{1}{4}((n_1^2 + n_2^2)\cos(\omega_{\mathrm{L}} t) + n_3^2) \tag{5.1.13}$$

via Eq. (5.1.11). $\vec{n} = (n_1, n_2, n_3)^T$ is the normalized total magnetic field vector. These derivations of the correlation functions are only for one single fixed Overhauser field. Since nuclear spin bath consists of a large number of magnetic moments with random orientation, the Overhauser field obeys the Gaussian distribution [31]

$$W(\vec{B}_N) = \left(\frac{2}{\pi}\right)^{3/2} (T^*)^3 e^{-2\left(|\vec{B}_N| T^*\right)^2}. \tag{5.1.14}$$

The FOA solution for C_2 is then obtained by averaging over all possible Overhauser field configurations. In the absence of a magnetic field this can be done analytically, yielding [31]

$$C_2(t) = \frac{1}{12}\left\{1 + 2\left[1 - 2\left(\frac{t}{2T^*}\right)^2\right]\exp\left[-\left(\frac{t}{2T^*}\right)^2\right]\right\}. \tag{5.1.15}$$

If an external magnetic field is applied and finding an analytical expression is no longer possible, we generate a large number of Overhauser field configurations from a Gaussian distribution and average the resulting correlations. The FOA describes short time dynamics accurately, but does not feature any long term decay of correlation. This is not surprising since the long-time decay is caused by the nuclear spin dephasing that the FOA neglects.

Fig. 5.1 shows $C_2(t)$ computed in the FOA, averaged over 10^6 Overhauser fields for (a) large and (b) small magnetic field strengths. It is clear to see in Fig. 5.1 a) that for external magnetic fields exceeding the Overhauser field ($b_x > 1$), the correlation quickly decays in $\mathcal{O}(T^*)$. Therefore, long-time dynamics of the system cannot be observed when a transversal magnetic field is applied. Since the distribution of Overhauser fields is Gaussian in the limit of infinite number of nuclear spins the envelope of the oscillation is Gaussian as well. The frequency of the oscillation is the Larmor frequency ω_L. Just for a very small or no external magnetic field the spin correlation does not decay completely. Therefore, it is only this regime where we will be able to investigate features that influence the decay after long times, such as the quadrupolar interaction. The impossibility to investigate the influence of quadrupolar interaction with external magnetic fields $b_x > 1$ in the second-order correlation function will be important later when the advantages of fourth-order correlation are discussed. In the absence of a magnetic field, the curve progression of $C_2(t)$ is described by Eq. (5.1.15). As the exponential term completely decays for $t \gg T^*$, the correlation remains at a constant $C_{\mathrm{lim}} = 1/12$ for large time. The local minimum is governed by the term quadratic in t.

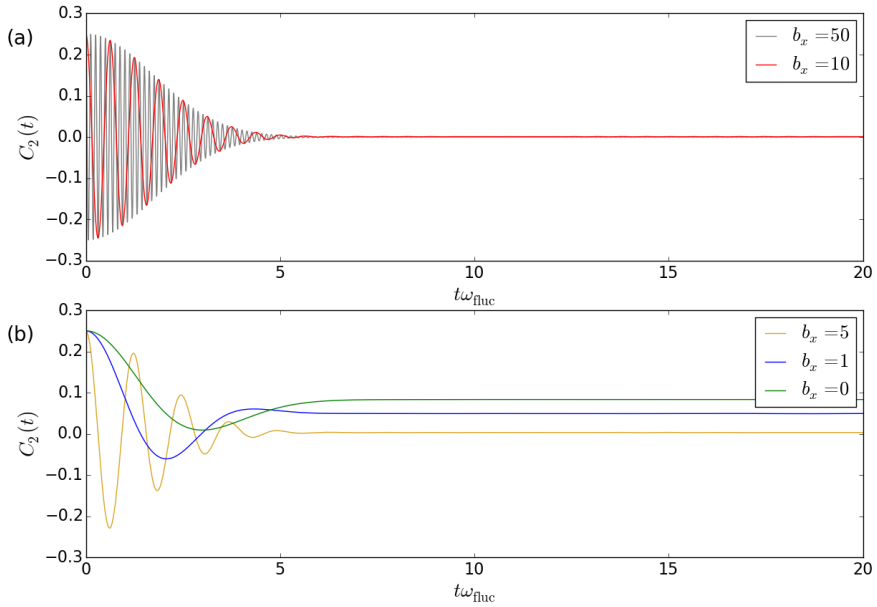

Figure 5.1: $C_2(t)$ computed in the FOA averaged over 10^6 Overhauser fields. Panel (a) shows the behaviour at higher magnetic fields ($b_x = 10$, 50), while panel (b) features $C_2(t)$ at small to intermediate fields ($b_x = 0$, 1, 5).

For the fourth-order spin auto-correlation function one obtains analogously for one Overhauser configuration

$$\begin{aligned} C_4(t_1, t_1+t_2, t_1) =& \frac{1}{16}[n_3^4 + (n_1^2+n_2^2)^2\cos(\omega_L(t_1-t_2)) \\ &+ n_3^2(n_1^2+n_2^2)\{\cos(\omega_L t_2) + \cos(\omega_L t_1)\}]. \end{aligned} \tag{5.1.16}$$

The results of the FOA for specific fourth-order correlations and noise will be discussed in the Chapter 7 and Chapter 8 studying their specific features.

5.2 Exact Solution with Homogeneous Couplings

Now we want to derive an exact solution of the correlation in the CSM under the assumption of homogeneous couplings (box model) $A_k = A_0$ and an external magnetic field $\vec{b}_{\mathrm{ext}} = b_z\vec{e}_z$, proposed by Kozlov [101]. The ratio between nuclear and electron Zeeman energy, ζ, is also assumed to be the same for all bath spins. Unlike the semi-classical approximation, this approach incorporates the bath spin dynamics. However, without a spread of coupling constants, this solution fails to describe the long-time decoherence accurately. For homogeneous coupling constants the bath can be described as one large spin $\vec{I} = \sum_k \vec{I}_k$. This results in the Hamiltonian

$$H = b_z S_z + \zeta b_z I_z + a_0\left(I_z S_z + \frac{1}{2\lambda}(I^+S^- + I^-S^+)\right). \tag{5.2.1}$$

For nuclear spins $I_k = 1/2$, the characteristic time scale is given by

$$T^* = \lambda \left(\sum_k A_k^2 \right)^{-1/2} = \frac{\lambda}{A_0 \sqrt{N}}. \tag{5.2.2}$$

using Eq. (3.3.4) which results in the dimensionless coupling constant of eq. (5.2.1)

$$a_0 = T^* A_0 = \frac{\lambda}{\sqrt{N}}. \tag{5.2.3}$$

The subspace of a given multiplet I is spanned by the Ising states $\{|I,-I\rangle, ... |I,I\rangle$. Adding the central electron spin, we arrive at the basis [101]

$$\begin{aligned} B = \{&|I,-I\rangle|\downarrow\rangle, |I,-I\rangle|\uparrow\rangle, |I,-I+1\rangle|\downarrow\rangle, \\ &|I,-I+1\rangle|\uparrow\rangle, ..., |I,I\rangle|\downarrow\rangle, |I,I\rangle|\uparrow\rangle\} \end{aligned} \tag{5.2.4}$$

for the Hamiltonian. In the special case without magnetic field ($b_z = 0$) or anisotropy ($\lambda = 1$), the Hamiltonian can be written as

$$H = \frac{a_0}{2}(F^2 - I^2 - S^2) \tag{5.2.5}$$

with the total system spin $\vec{F} = \vec{I} + \vec{S}$. The eigenstates and eigenvalues can be derived easily via spin addition [27].
With an anisotropy or an applied magnetic field, exact diagonalization is still possible. In the basis B, the Hamilton matrix is given by

$$H = \begin{pmatrix} E_+(I,0) & & & \dots & & 0 \\ & M_I^{-I+1} & & \dots & & \\ \vdots & & M_I^{-I+2} & & & \vdots \\ \vdots & & & \ddots & & \vdots \\ \vdots & & & & M_I^I & \vdots \\ 0 & & \dots & & & E_-(I,2I+1) \end{pmatrix}. \tag{5.2.6}$$

$E_I^{\pm}(I,n)$ are scalars

$$E_+(I,-I) = \langle I,-I| \langle\downarrow| H |\downarrow\rangle |I,-I\rangle = \frac{a_0 I - b_z}{2} - \zeta b_z I, \tag{5.2.7}$$

$$E_-(I,I+1) = \langle I,I| \langle\uparrow| H |\uparrow\rangle |I,I\rangle = \frac{a_0 I + b_z}{2} + \zeta b_z I, \tag{5.2.8}$$

for $n = 0, 2I+1$ and M_I^L are 2×2 matrices in the basis $\{|L\rangle|\downarrow\rangle, |L-1\rangle|\uparrow\rangle\}$,

$$M_I^L = \begin{pmatrix} -\frac{b_z + a_0 L}{2} + z b_z L & \xi_I^L \\ \xi_I^L & \frac{b_z + a_0(L-1)}{2} + \zeta b_z (L-1), \end{pmatrix} \tag{5.2.9}$$

with

$$\xi_I^L = \frac{a_0}{2\lambda}\sqrt{I(I+1) - L(L-1)}. \tag{5.2.10}$$

Through diagonalization of the 2×2 submatrices M_I^L, the eigenvalues for $n = 1, ..., 2I$

$$E_\pm(I,L) = -\frac{a_0}{4} \pm \frac{1}{2}\sqrt{\left(\frac{a_0}{2}(2L-1) + b_z(1-\zeta)\right)^2 + 4\left(\xi_I^L\right)^2}. \tag{5.2.11}$$

and the eigenstates

$$\begin{aligned} &|I,L,-\rangle = \\ &\quad \mathcal{A}_{I,L,-}\,|I,L\rangle\,|{\downarrow}\rangle + \mathcal{B}_{I,L,-}\,|I,L-1\rangle\,|{\uparrow}\rangle\,, \\ &|I,L,+\rangle = \\ &\quad \mathcal{A}_{I,L,+}\,|I,L\rangle\,|{\downarrow}\rangle + \mathcal{B}_{I,L,+}\,|I,L-1\rangle\,|{\uparrow}\rangle\,. \end{aligned} \tag{5.2.12}$$

are obtained. Here, the pre-factors $A_{I,n,\pm}$ and $B_{I,n,\pm}$ amount to

$$\begin{aligned} \mathcal{A}_{I,L,\pm} &= \frac{2\xi_I^L}{\sqrt{(b_z + a_0 L + 2E_{L,\pm} - 2\zeta b_z L)^2 + (2\xi_I^L)^2}}\,, \\ \mathcal{B}_{I,L,\pm} &= \frac{b_z + a_0 L + 2E_{L,\pm} - 2\zeta b_z L}{\sqrt{(h + a_0 L + 2E_{L,\pm} - 2\zeta h L)^2 + (2\xi_I^L)^2}}, \end{aligned} \tag{5.2.13}$$

and give the mixing of the Ising states of the basis B. The first and last eigenstates in our basis, $n = 0, 2I+1$, are the Ising states with extremal polarization, where no spin flip can occur,

$$|I,0,+\rangle = |I,-I\rangle\,|{\downarrow}\rangle \tag{5.2.14}$$

$$|I,2I+1,-\rangle = |I,I\rangle\,|{\uparrow}\rangle \tag{5.2.15}$$

with the corresponding eigenvalues from eq. (5.2.8).

Now we are able to evaluate the dynamics of any desired observable that can be expressed in the basis B. Here, we are specifically interested in autocorrelation functions of the form $C(t) = \langle O(t)O\rangle$ with

$$\begin{aligned} C(t) =& \frac{1}{Z}\sum_{I=0}^{N/2} N_w(I) \sum_{\sigma,\sigma'=\pm} \sum_{n,m=0}^{2I+1} |\,\langle I,n,\sigma|O_1|I,m,\sigma'\rangle\,|^2 \\ &\times \exp(\mathrm{i}(E_\sigma(I,n) - E_{\sigma'}(I,m))t). \end{aligned} \tag{5.2.16}$$

For the total bath spin length I there are

$$N_w(I) = \frac{(N/2-I)!(2I+1)}{N/2+I+1} \tag{5.2.17}$$

of possible configurations for a bath with an even bath size N. In the high temperature limit all states are equally occupied, and the partition function reads

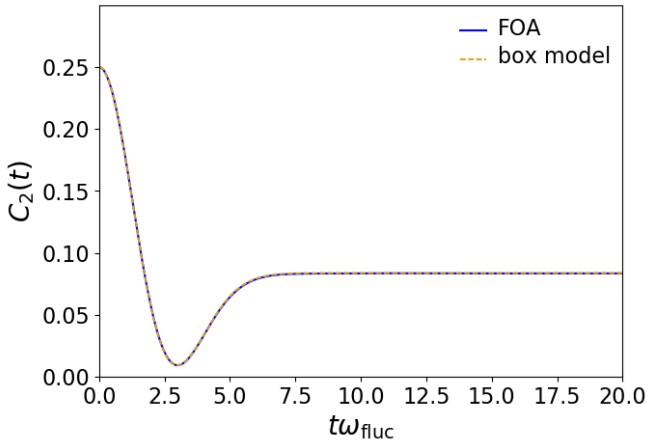

Figure 5.2: $C_2(t)$ computed in the box model for $N = 500$ nuclear spins without magnetic field, plotted alongside the FOA results averaged over 10^6 Overhauser fields.

$Z = 2^{N+1}$ for 1/2 bath spins. For the autocorrelation function of the electronic spin transverse to the magnetic field, one arrives at

$$\begin{aligned}\langle S_x(t)S_x(0)\rangle =&\frac{1}{4Z}\sum_{I=0}^{N/2} N_w(I)\sum_{\sigma,\sigma'=\pm}\sum_{n=0}^{2I} A_{n,\sigma}^2 B_{n+1,\sigma'}^2 \\ &\times\cos((E_\sigma(I,n)-E_{\sigma'}(I,n+1))t).\end{aligned} \tag{5.2.18}$$

To simplify the sum expression, we have defined $A_{I,0,-} = B_{I,0,\pm} = A_{I,2I+1,\pm} = B_{I,2I+1,+} = 0$ and $A_{I,0,+} = B_{I,2I+1,-} = 1$.
The autocorrelation function of the total bath spin transverse to the magnetic field can be computed analogously,

$$\begin{aligned}\langle I_x(t)I_x\rangle =&\frac{1}{4Z}\sum_{I=0}^{N/2} N_w(I)\sum_{\sigma,\sigma'=\pm}\sum_{n=0}^{2I}[A_{n,\sigma}A_{n+1,\sigma'}B_{n,\sigma}B_{n+1,\sigma'} \\ &\times\sqrt{I(I+1)-(-I+n+1)(-I+n)} \\ &\times\sqrt{I(I+1)-(-I+n-1)(-I+n)}]^2 \\ &\times\cos((E_{\sigma'}(n+1)-E_\sigma(n))t).\end{aligned} \tag{5.2.19}$$

This expression can be easily evaluated in a computing time of $\mathcal{O}(N^2)$, which is highly preferable to a computation time of $\mathcal{O}(D)$, since the Hilbert-space dimension grows exponentially with the bath size N.

To obtain the spin noise, the spin correlation is brought in the frequency domain. Fourier transformation of Eq. (5.2.18) yields

$$\begin{aligned}C_2(\omega) =&\frac{\pi^2}{Z}\sum_{I=0}^{N/2} N_w(I)\sum_{\sigma,\sigma'=\pm}\sum_{n=0}^{2I} A_{n,\sigma}^2 B_{n+1,\sigma'}^2 \\ &\times[\delta(\omega-(E_{\sigma'}(n+1)-E_\sigma(n)))]\end{aligned} \tag{5.2.20}$$

with the delta-distribution $\delta(\omega - \Delta E)$. The nuclear spin bath noise is obtained analogously

$$\begin{aligned}(I_x^2)_\omega =& \frac{1}{4Z}\sum_{I=0}^{N/2} N_w(I) \sum_{\sigma,\sigma'=\pm}\sum_{n=0}^{2I}[A_{n,\sigma}A_{n+1,\sigma'}B_{n,\sigma}B_{n+1,\sigma'} \\ &\times \sqrt{I(I+1)-(-I+n+1)(-I+n)} \\ &\times \sqrt{I(I+1)-(-I+n-1)(-I+n)}]^2 \\ &\times [\delta(\omega-(E_{\sigma'}(n+1)-E_\sigma(n)))]\,.\end{aligned} \tag{5.2.21}$$

In order to properly present the spectra, the delta-distributions are represented by the Lorentzian

$$\Gamma(\omega, \Delta E) = \frac{1}{\pi}\frac{\gamma}{(\omega-\Delta E)^2+\gamma^2} \tag{5.2.22}$$

with the broadening factor $T^*\gamma = 0.01$ in all following results.

Fig. 5.2 proves that this method concerning the box model produces congruent results to the FOA. But the exact solution in the box model has the following advantage: With this method the nuclear spin bath dynamics can be investigated for large baths, while it is considered frozen in the FOA.

5.3 Full Exact Diagonalization

So far we discussed two different analytical schemes in order to obtain the spin dynamics. They have the benefit of being computationally advantageous and able to simulate large to infinite number of nuclear spins. They are, however, very limited in the interactions they model, and their predictions are only valid for short times. Therefore, the following two section will present two numerical schemes able to simulate the full quantum mechanical model with inhomogeneous hyperfine interaction and quadrupolar interaction.

Matrix diagonalization schemes are fairly canonical. Here, a pre-existing LAPACK routine was used. What is more interesting is how to compute fourth-order correlation function optimally, once the eigenvalues ϵ_ν and the eigenvectors $|\nu\rangle$ following

$$H|\nu\rangle = \epsilon_\nu|\nu\rangle \tag{5.3.1}$$

are known. The second-order correlation of an arbitrary hermitian operator O can be computed in a straight-forward manner

$$\langle O(t)O\rangle = \frac{1}{D}\sum_{nm}^{D}|O_{nm}|^2 \mathrm{e}^{\mathrm{i}(\epsilon_n-\epsilon_m)t} \tag{5.3.2}$$

with $O_{nm} = \langle n|O|m\rangle$ in a computation time of $\mathcal{O}(D^2)$ and D being the dimension of the Hilbert space. This is not ideal, but since the matrix diagonalization also takes a computation time of $\mathcal{O}(D^3)$, this does not exacerbate the problem. But in the case of a fourth-order correlation of two arbitrary hermitian operators O_1 and O_2, this simple scheme

$$\begin{aligned} O_4(t_1,t_2) =& \langle O_1(t_1)O_2(t_1+t_2)O_1(t_1)O_2\rangle \\ =& \frac{1}{D}\sum_{nmkl}^{D} O^1_{nm}O^2_{mk}O^1_{kl}O^2_{ln}e^{\mathrm{i}(E_n-E_l)t_1}e^{\mathrm{i}(E_m-E_k)t_2} \end{aligned} \tag{5.3.3}$$

results in a computation time of $\mathcal{O}(D^4)$. Since the Hilbert space dimension D grows exponentially with the system size, this computation time is not viable. We can, however, use a matrix multiplication scheme in order to drastically reduce computation time. We can rearrange the term of Eq. (5.3.3) to

$$\begin{aligned} O_4(t_1,t_2) &= \frac{1}{D}\sum_{ml}\left[\sum_k O^2_{mk}e^{\mathrm{i}(E_m-E_k)t_2}O^1_{kl}\right]\left[\sum_n O^2_{ln}e^{\mathrm{i}(E_n-E_l)t_1}O^1_{nm}\right] \\ &= \frac{1}{D}\sum_{ml} A_{ml}(t_2)B_{lm}(t_1) \\ &= \frac{1}{D}\sum_m [A(t_2)B(t_1)]_{mm} \\ &= \frac{1}{D}\mathrm{Tr}[A(t_2)B(t_1)] \end{aligned} \tag{5.3.4}$$

with

$$A_{ml}(t) = \sum_k O^2_{mk}e^{\mathrm{i}(E_m-E_k)t}O^1_{kl} \tag{5.3.5}$$

$$B_{lm}(t) = \sum_k O^2_{lk}e^{\mathrm{i}(E_k-E_l)t}O^1_{km}. \tag{5.3.6}$$

We want to compute these matrices efficiently using pre-existing optimised linear algebra packages. Therefore, we define the auxiliary matrices

$$\tilde{O}^1_{lk}(t) = O^1_{lk}e^{\mathrm{i}E_l t} \tag{5.3.7}$$

$$\tilde{O}^2_{lk}(t) = O^2_{lk}e^{\mathrm{i}E_l t}. \tag{5.3.8}$$

A and B can then be obtained via matrix multiplication of $\tilde{O}^1$ and $\tilde{O}^2$.

$$\begin{aligned} A_{ml}(t) &= \sum_k \tilde{O}^2_{mk}(t)\tilde{O}^1_{kl}(-t) = \left[\tilde{O}^2(t)\tilde{O}^1(-t)\right]_{ml} \\ B_{lm}(t) &= \sum_k \tilde{O}^2_{lk}(-t)\tilde{O}^1_{km}(t) = \left[\tilde{O}^2(-t)\tilde{O}^1(t)\right]_{lm} \end{aligned} \tag{5.3.9}$$

For every time pair (t_1, t_2) the fourth-order spin correlation is evaluated at, the computation time of the auxiliary matrices is $\mathcal{O}(D^k)$, with $2.4 < k < 2.8$ depending on the optimized algorithm. Computation of the matrices A and B

is $\mathcal{O}(D^k)$ as well. It is possible to achieve a considerable speed-up by using a highly optimised LAPACK or BLAS routine for matrix multiplication and trace evaluation. By keeping the computation time per time-pair in $\mathcal{O}(D^3)$ instead of $\mathcal{O}(D^4)$, obtaining a fourth-order correlation function becomes feasible. We sacrifice memory for the speed-up, since the auxiliary matrices as well as A and B need to be stored. The memory requirement also grows exponentially with the number of nuclear spins.

The number of nuclear spins one is able to simulate using exact diagonalization is thus very limited. In order to reduce the effects of this limitation, N_c A_k configurations are generated, and a configuration average obtained. This reduces finite size effects and thus compensates for the small bath size.

This scheme is applicable to both fourth-order correlations we analyze in this thesis. For the correlation function measured by the three pulse measurement $G_4(t_1, t_1 + t_2, t_1)$, $O_1 = O_2 = P_\downarrow$. In the case of the fourth-order correlation measured by the spin echo method, $P_{g_0,g_0}(T, \tau)$, the operators differ $O_1 = S_y$ and $O_2 = S_z$, and the time-pair is casted from (t_1, t_2) to $(T + \tau, T - \tau)$.

5.4 Lanczos Method with Restart

In a large system it is often not numerically viable to evaluate the dynamics exactly, since the dimension of the Hilbert space, D, grows exponentially with system size. In this section we will discuss the Lanczos algorithm, a method to find a representation of the Hamiltonian in a much smaller subspace. This enables us to propagate a state in time without knowing all eigenvalues and eigenstates.

5.4.1 The Lanczos Algorithm and Time Propagation

The time propagation of an arbitrary state $|r\rangle$ can be expressed by Taylor expansion. Terminating the expansion

$$\mathrm{e}^{-\mathrm{i}Ht}\,|r\rangle = |r\rangle - \mathrm{i}Ht\,|r\rangle - \frac{1}{2}H^2t^2\,|r\rangle + \frac{1}{6}\mathrm{i}H^3\,|r\rangle + ... \tag{5.4.1}$$

after $M \ll D$ summands will result in a vector living in

$$\mathcal{K}^M(|r\rangle) = \mathrm{span}(|r\rangle\,, H\,|r\rangle\,, ..., H^{M-1}\,|r\rangle), \tag{5.4.2}$$

the M dimensional Krylov space. The error made in this truncation is of the order of $\mathcal{O}(H^M t^M)$. Therefore it is not exact for arbitrarily large times, like the full exact diagonalization. In order to express a representation of the Hamiltonian within the Krylov space, the Lanczos algorithm [102] constructs an orthonormal base of the subspace. The first base vector is chosen to be $|\phi_0\rangle = |r\rangle$, the normalized vector we want to propagate. The second base vector is obtained by applying the Hamiltonian to the state and subtracting the component parallel to $|\phi_0\rangle$,

$$b_1\,|\phi_1\rangle = |\tilde{\phi}_0\rangle = H\,|\phi_0\rangle - a_0\,|\phi_0\rangle \tag{5.4.3}$$

with $b_n^2 = \langle\tilde{\phi}_n|\tilde{\phi}_n\rangle$ and $a_n = \langle\phi_n|H|\phi_n\rangle$. The next two base vectors can be derived similarly,

$$b_2 |\phi_2\rangle = |\tilde{\phi}_2\rangle = H |\phi_1\rangle - \sum_{i=0}^{1} |\phi_i\rangle \langle\phi_i| H |\phi_1\rangle = H |\phi_1\rangle - a_1 |\phi_1\rangle - b_1 |\phi_0\rangle \quad (5.4.4)$$

$$b_3 |\phi_3\rangle = |\tilde{\phi}_3\rangle = H |\phi_2\rangle - \sum_{i=0}^{2} |\phi_i\rangle \langle\phi_i| H |\phi_2\rangle = H |\phi_2\rangle - a_2 |\phi_2\rangle - b_2 |\phi_2\rangle . \quad (5.4.5)$$

The orthogonalization of the base vectors and Eq. (5.4.3) results in $\langle\phi_2|H|\phi_0\rangle = 0$. Therefore, the last summand in Eq. (5.4.5) vanishes. All further orthonormal base vectors can be obtained analogously,

$$b_{n+1} |\phi_{n+1}\rangle = |\tilde{\phi}_{n+1}\rangle = H |\phi_n\rangle - a_n |\phi_n\rangle - b_n |\phi_{n-1}\rangle . \quad (5.4.6)$$

Rearrangement of Eq. (5.4.6)

$$H |\phi_n\rangle = b_n |\phi_{n-1}\rangle + a_n |\phi_n\rangle + b_{n+1} |\phi_{n+1}\rangle \quad (5.4.7)$$

shows the representation of the Hamiltonian in the Krylov space to be tridiagonal. Diagonalization of

$$\underline{\underline{H}}(M) = \begin{pmatrix} a_0 & b_1 & 0 & 0 & & 0 & 0 \\ b_1 & a_1 & b_2 & 0 & \cdots & 0 & 0 \\ 0 & b_2 & a_2 & b_3 & & 0 & 0 \\ 0 & 0 & b_3 & a_3 & & 0 & 0 \\ & \vdots & & & \ddots & \vdots & \\ 0 & 0 & 0 & 0 & & a_{M-2} & b_{M-1} \\ 0 & 0 & 0 & 0 & \cdots & b_{M-1} & a_{M-1} \end{pmatrix} . \quad (5.4.8)$$

results in the eigenvectors $|\zeta^n\rangle$ and the eigenvalues ϵ_n

$$\underline{\underline{H}}(M) |\zeta\rangle = \epsilon_\zeta |\zeta\rangle . \quad (5.4.9)$$

To transfer the eigenvectors $|\zeta\rangle$ into the original Hilbert space, the transition matrix

$$\Phi = (\phi_1, \phi_2, ..., \phi_M) \quad (5.4.10)$$

is defined. We gain a set of M approximate eigenvectors of H by the base transform

$$|\nu\rangle = \Phi |\zeta\rangle . \quad (5.4.11)$$

This then enables us to propagate the state $|r\rangle$ in time by inserting an identity matrix

$$\mathbf{1} = \sum_{\nu}^{M} |\nu\rangle \langle\nu| , \quad (5.4.12)$$

in the Krylov space. This results in

$$\mathrm{e}^{-\mathrm{i}Ht}\,|r\rangle \approx \sum_{\nu}^{M} \mathrm{e}^{-\mathrm{i}\epsilon_\nu t}\,\langle\nu|r\rangle\,|\nu\rangle\,, \tag{5.4.13}$$

a term that is easily evaluated in a computing time of $\mathcal{O}(M)$, once the eigenvalues and eigenvectors of $\underline{\underline{H}}(M)$ are known. Since $|r\rangle$ is the first base vector of the Krylov space, $\langle\nu^n|r\rangle = \vec{\nu}[0]$. Computing $\underline{\underline{H}}(M)$ for one starting vector $|r\rangle$ and a Hamiltonian H needs a computation time $\mathcal{O}(DM)$, since one needs to apply H M times to a state. The diagonalization takes a computation time of $\mathcal{O}(M^3)$. In the case of $M \ll D$, this constitutes a great decrease in computation time and memory requirement compared to full exact diagonalization. The Lanczos method, however, is not always stable and can suffer from a loss of orthogonalization, where a larger M does not translate into a longer time one is able to correctly simulate. In the following sections we will discuss a scheme that allows us to evolve the state in discrete time steps.

Fast dynamics, such as a large external magnetic field $b_x \gg 1$, limit the maximum time the Lanczos algorithm can simulate while keeping the accumulating error minimal. If the external magnetic field b_x is high and the hyperfine and quadrupolar interactions can be neglected, the eigenvalues become degenerate, taking the form $E_\pm = \pm b_x(1-\zeta)/2$, see Eq. (5.2.11). Since the Taylor expansion is terminated after the Mth summand, the $M+1$ summand should fulfil the relation

$$\frac{1}{(M+1)!}(E_+ t)^{M+1} < 1, \tag{5.4.14}$$

which, solved for t, becomes

$$t_{\max} = \frac{2}{b_x(1-\zeta)}\,\sqrt[M+1]{(M+1)!}. \tag{5.4.15}$$

In the case of an external field $b_x = 100$, with a Lanczos depth of $M = 200$ and $\zeta = 0$, the maximum simulation time becomes $t_{\max} = 1.85T^*$, which is why the method of 'restarting' the algorithm will be introduced in the following chapters. Note that simply increasing M will not work limitlessly, since errors in the orthogonalization process accumulate. Generally speaking, decreasing the simulated time is better than increasing M.

5.4.2 Stochastic Evaluation of the Trace

While the Lanczos method yields M approximate eigenvalues and eigenstates in a time $\mathcal{O}(M^3)$, the expectancy value of an arbitrary operator O has to be obtained. In order to do this, we have to evaluate the trace without knowing all

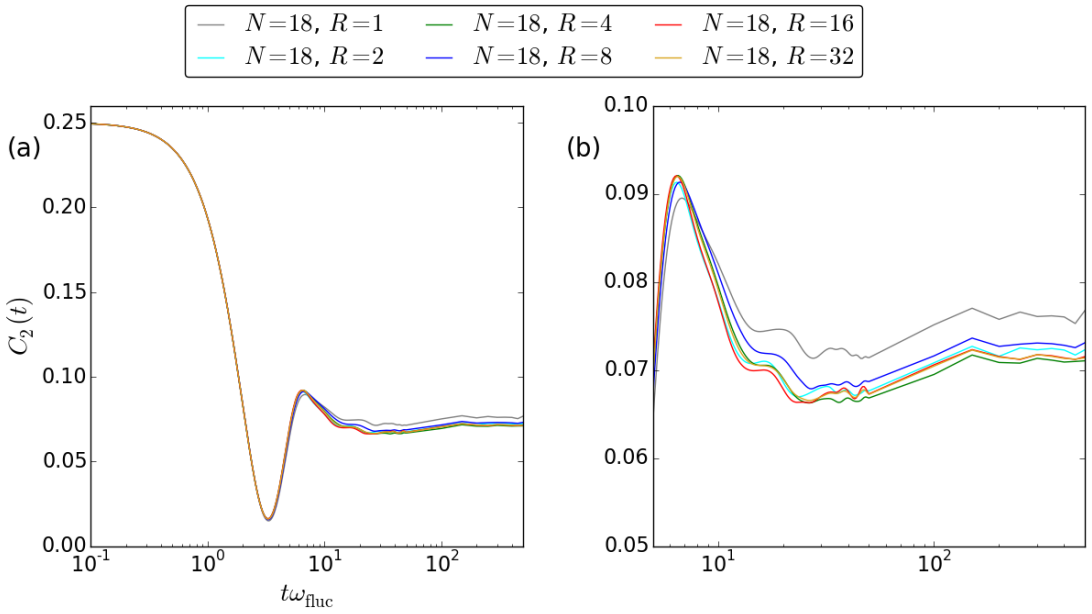

Figure 5.3: Panel (a) depicts $C_2(t)$ computed with Lanczos for $N = 18$ spins $I = 1/2$ without a magnetic field. The number of random starting vectors R is varied. Each starting vector is time evolved with a different configuration of hyperfine coupling constants. Panel (b) shows a detailed plot to make the convergence wit R more visible.

D eigenstates. Therefore, it is advantageous to use stochastic trace approximation [103]. Here, we chose a small number $R \ll D$ of random vectors $|r\rangle$

$$|r\rangle = \sum_{i=1}^{D} \xi_i^r \, |i\rangle \tag{5.4.16}$$

where $|i\rangle$ is an orthonormal base spanning the entire Hilbert space, and the random coefficients ξ_i^r obey the statistics

$$\langle\langle \xi_i^r \rangle\rangle = 0 \tag{5.4.17}$$

$$\langle\langle \xi_i^r \xi_i^r \rangle\rangle = \delta_{ij}/\sqrt{D} \tag{5.4.18}$$

Then the trace is approximated by

$$\mathrm{Tr}[O] = \sum_i \langle i|O|i\rangle = \frac{1}{R}\sum_{r=1}^{R} \langle r|O|r\rangle + \mathcal{O}\left(\frac{1}{\sqrt{DR}}\right). \tag{5.4.19}$$

The relative error made by this approximation is of the order $\mathcal{O}(1/\sqrt{DR})$ [103]. This is fortuitous, as in large systems the relative error actually decreases. The larger the Hilbert space, the less random states need to be evaluated to achieve the same accuracy. This is evidenced in Fig. 5.3, where the total number of randomly generated starting vectors does not have to be large for the results to converge, due to the large Hilbert space ($N = 18$, $I = 1/2$).

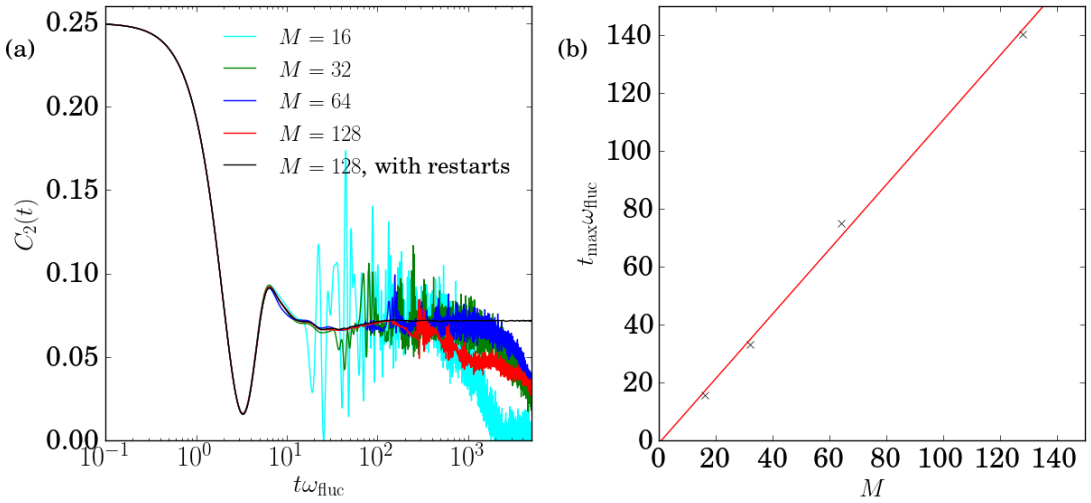

Figure 5.4: Panel (a) shows $C_2(t)$ in the absence of a magnetic field and a bathsize of $N = 18$ computed with different Lanczos depths M. For comparison, $C_2(t)$ resulting from a Lanczos algorithm with a restart performed in intervals of $\delta t = 50T^*$ with a depth of $M = 128$ is shown alongside. Panel (b) the maximum time at which the results of the Lanczos method are still valid is plotted in relation to the Lanczos depth M.

5.4.3 Application to Second Order Correlation Functions

It is now the goal to apply the aforementioned technique to a second-order autocorrelation function,

$$\langle O(t)O\rangle = \frac{1}{D}\mathrm{Tr}[O(t)O] \approx \frac{1}{RD}\sum_{r=1}^{R}\langle r|\mathrm{e}^{\mathrm{i}Ht}O\mathrm{e}^{-\mathrm{i}Ht}O|r\rangle\,. \tag{5.4.20}$$

Since we are interested in second-order correlations of different operators, we will use an arbitrary operator O as a placeholder. The Lanczos method is used to propagate the initial states $|r_1\rangle = |r\rangle$ and the normalized starting vector $|r_2\rangle = O|r\rangle / \sqrt{\langle r|O^2|r\rangle}$. The second starting vector $|\tilde{r}_2\rangle = O|r\rangle$ needs to be normalized in order to correctly perform the Lanczos method, the first starting vector is already normalized by definition of the stochastic trace evaluation. The time propagation results in the term

$$\langle O(t)O\rangle = \frac{\sqrt{\langle r|O^2|r\rangle}}{RD}\sum_{r}^{R}\sum_{\nu_1}^{M}\sum_{\nu_2}^{M}\mathrm{e}^{\mathrm{i}(\epsilon_\nu^1-\epsilon_\nu^2)t}\,\langle\nu_1|r_1\rangle\,\langle\nu_2|r_2\rangle\,\langle\nu_1|O|\nu_2\rangle\,, \tag{5.4.21}$$

where the prefactor $\sqrt{\langle r|O^2|r\rangle}$ accounts for the normalization of $|r_2\rangle$.

However, as previously mentioned, the maximum time that can be simulated with sufficient accuracy through this method is limited. The Lanczos algorithm, through an accumulation of numerical inaccuracies, can lose orthogonality of the basis vectors $|\phi_n\rangle$ for large M. If we want to simulate large times, we cannot

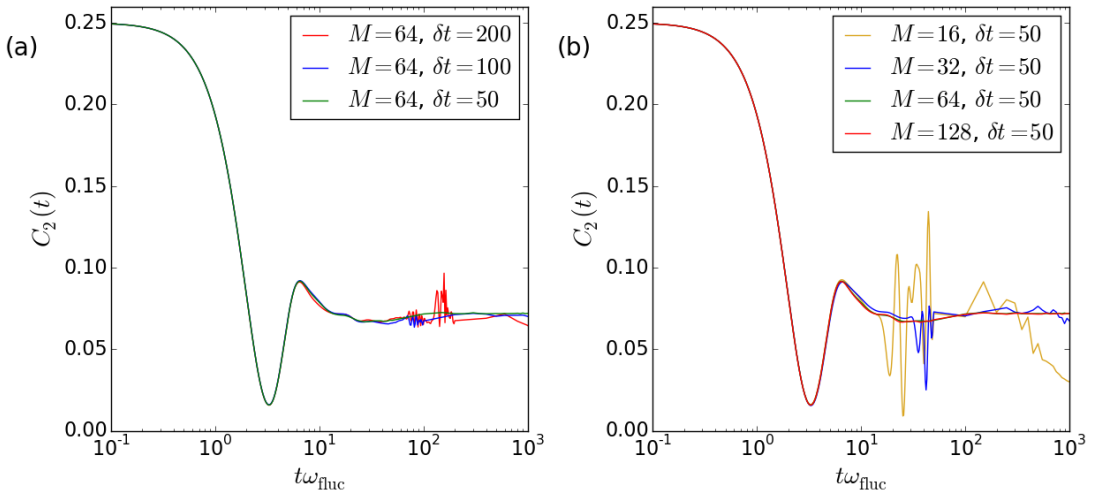

Figure 5.5: In the left panel (a) $C_2(t)$ is plotted in the absence of a magnetic field and a bathsize of $N = 18$ computed with the Lanczos depth $M = 64$ and different distances between restarts δt. The right panel, (b), shows $C_2(t)$ obtained for $\delta t = 50$ with different Lanczos depths M.

simply increase M, since the accuracy does not improve after a threshold M. The loss of accuracy with time is shown in Fig. 5.4. The maximum simulation time for which the results of the Lanczos method are still reliable grows linear with the Lanczos depth M. Therefore, we have to employ the Lanczos method with restarts, in which the second-order auto-correlation function is written as

$$\langle O(t)O\rangle = \frac{1}{RD}\sum_{r}^{R}\langle 1_r(t)|O|2_r(t)\rangle \tag{5.4.22}$$

with

$$|1_r(t)\rangle = \mathrm{e}^{-\mathrm{i}Ht}\,|r\rangle \tag{5.4.23}$$

$$|2_r(t)\rangle = \mathrm{e}^{-\mathrm{i}Ht}O\,|r\rangle\,. \tag{5.4.24}$$

The time is discretized to $t_n = n\tau$, $n \in \mathbb{Z}$ and the recursion relation

$$|\psi(t_n)\rangle = \mathrm{e}^{-\mathrm{i}H\tau}\,|\psi(t_{n-1})\rangle \tag{5.4.25}$$

is used to propagate a state $|\psi(t_n)\rangle$ in reasonable small time increments τ. This incremental time propagation calculated through the Lanczos algorithm and expressed as

$$|1_r(t_n)\rangle = \mathrm{e}^{-\mathrm{i}H\tau}\,|1_r(t_{n-1})\rangle = \sqrt{\langle 1_r(t_{n-1})|1_r(t_{n-1})\rangle}\sum_{\nu}^{M}\mathrm{e}^{-\mathrm{i}\epsilon_\nu^n\tau}c_n^1(t_{n-1})\,|\nu_1^n\rangle \tag{5.4.26}$$

where $c_n^1(t_{n-1}) = \langle\nu_1^n|1_r(t_{n-1})\rangle$. The result becomes exact for $\tau \to 0$. The normalized state $|1_r(t_{n-1})\rangle\,/\sqrt{1_r(t_{n-1})|1_r(t_{n-1})}$ is used as the starting vector for

the algorithm. To arrive at $|1_r(t_{N_t})\rangle$, N_t Lanczos time evolution steps have to be computed. The same time evolution is needed for the vector $|2_r(t)\rangle$,

$$|2_r(t_n)\rangle = \mathrm{e}^{-\mathrm{i}H\tau}\,|2_r(t_{n-1})\rangle = \sqrt{\langle 2_r(t_{n-1})|2_r(t_{n-1})\rangle}\sum_{\nu}^{M}\mathrm{e}^{-\mathrm{i}\epsilon_\nu^n\tau}c_n^2(t_{n-1})\,|\nu_2^n\rangle\,, \tag{5.4.27}$$

where $c_n^2(t_{n-1}) = \langle\nu_2^n|2_r(t_{n-1})\rangle$ and the normalized starting vector of the algorithm $|2_r(t_{n-1})\rangle\,/\sqrt{2_r(t_{n-1})|2_r(t_{n-1})}$. Having gained both $|1_r(t_n)\rangle$ and $|2_r(t_n)\rangle$, we can calculate the auto-correlation function $\langle O(t)O\rangle$ using Eq. (5.4.22). $2N_t$ Lanczos iterations are needed for N_t time steps. We can obtain intermediate time points by substituting τ with Δt ($0 < \Delta t < \tau$) in Eq. (5.4.26) and (5.4.27), calculating correlation function at $t_{n-1} + \Delta t$. This way, several time steps between t_{n-1} and t_n can be obtained without having to perform the Lanzcos algorithm with a different starting vector. This gives us the flexibility to chose τ smaller or larger depending on the dynamics of the system, while keeping the same time resolution. The advantage of this method can be seen in Fig. 5.5, where the results converge for $M = 64$ and a distance between restarts of $\delta = 50$.

5.4.4 Application to Fourth Order Correlation Functions

In this section we review how to use the Lanczos method with restarts on fourth-order correlation C_4 in the special case of $\tau_1 = \tau_3 = t$, $\tau_2 = 2t$

$$\begin{aligned} C_4(t,2t,t) &= 2\,\langle S_z(t)S_z(2t)S_z(t)S_z\rangle \\ &= \frac{2}{RD}\sum_{r}^{R}\langle 1_r(t)|S_z e^{\mathrm{i}Ht}S_z e^{-\mathrm{i}Ht}S_z|2_r(t)\rangle \end{aligned} \tag{5.4.28}$$

as introduced in Chapter 4. $|1_r(t)\rangle$ and $|2_r(t)\rangle$ are the time propagated vectors

$$|1_r(t)\rangle = e^{-\mathrm{i}Ht}\,|r\rangle \tag{5.4.29}$$

$$|2_r(t)\rangle = e^{-\mathrm{i}Ht}P_\downarrow\,|r\rangle \tag{5.4.30}$$

and we proceed analogous to the time propagation in Sec. 5.4.3 arriving at

$$|1_r(t_n)\rangle = \mathrm{e}^{-\mathrm{i}H\tau}\,|1_r(t_{n-1})\rangle = \sum_{n}^{M}\mathrm{e}^{-\mathrm{i}\epsilon_\nu^n\tau}c_n^1(t_{n-1})\,|\nu_1^n\rangle\,, \tag{5.4.31}$$

where $c_n^1(t_{n-1}) = \langle\nu_1^n|1_r(t_{n-1})\rangle$ and a discretized time $t_n = n\tau$, $n \in \mathbb{Z}$. The same time evolution is needed for the vector $|2_r(t)\rangle$,

$$|2_r(t_n)\rangle = \mathrm{e}^{-\mathrm{i}H\tau}\,|2_r(t_{n-1})\rangle = \sum_{n}^{M}\mathrm{e}^{-\mathrm{i}\epsilon_\nu^n\tau}c_n^2(t_{n-1})\,|\nu_2^n\rangle\,, \tag{5.4.32}$$

where $c_n^2(t_{n-1}) = \langle \nu_2^n | 2_r(t_{n-1}) \rangle$. Until now the procedure is the same as for the second-order correlation function. But now we need to additionally propagate

$$|3_r(t_n)\rangle = e^{-\mathrm{i}Ht_n} |3_r(0)\rangle \tag{5.4.33}$$

$$|4_r(t_n)\rangle = e^{-\mathrm{i}Ht_n} |4_r(0)\rangle \tag{5.4.34}$$

in time, where the starting points are $|3_r(0)\rangle = S_z |1_r(t_n)\rangle$ and $|4_r(0)\rangle = S_z |2_r(t_n)\rangle$. For each point t_n in time, two Lanczos propagations have to be performed. The fourth-order correlation function

$$C_4(t, 2t, t) = \frac{2}{RD} \sum_r^R \langle 3_r(t) | S_z | 4_r(t) \rangle \,. \tag{5.4.35}$$

can then be easily evaluated, since the S_z is diagonal in the original Ising basis. In conclusion, $4n$ Lanczos time evolutions are necessary to arrive at the single value of $C_4(t_n, 2t_n, t_n)$. Here we first calculate a set of N vectors $|1_r(t_n)\rangle$ and $|2_r(t_n)\rangle$, then compute $G_4(t_n, 2t_n, t_n)$ by a parallelized algorithm for obtaining $|3_r(t_n)\rangle$ and $|4_r(t_n)\rangle$.

5.5 Classical Equations of Motion

Results obtained by the classical equations of motion method [67,69] are compared to fourth and second-order correlation within the fully quantum mechanical model in this work. Therefore, this section briefly reviews this method for completeness. For a more details see Refs. [67, 69, 104].

Comparing quantum mechanical observables with their classical equivalents can be useful to ascertain if a feature is uniquely quantum mechanical in nature. Classically, spins can be imagined as magnetic dipoles rotating freely in a magnetic field. The classical limit is most accurate for very long spins or very large spin baths. In this chapter we will derive classical equations of motion that describe the spin dynamics in the central spin model. In quantum physics, the dynamics of an arbitrary operator $\hat{O}(t)$ can be expressed using the Heisenberg equation

$$\frac{\mathrm{d}\hat{O}}{\mathrm{d}t} = i[H, \hat{O}]. \tag{5.5.1}$$

After the commutators $[H, \vec{S}]$ and $[H, \vec{I}_k]$ are derived employing quantum mechanical commutator relations, we shift from the quantum mechanical to the classical model. Then the spin components can be expressed as the magnetic dipole's spatial orientations. If the quadrupolar interaction is completely isotropic ($\eta = 0$),

the dynamics of the spins are described by the equations of motion

$$\frac{\mathrm{d}\vec{S}}{\mathrm{d}t} = \vec{b}_{\mathrm{tot},S} \times \vec{S} \tag{5.5.2}$$

$$\frac{\mathrm{d}\vec{I}_k}{\mathrm{d}t} = \vec{b}_{\mathrm{tot},I_k} \times \vec{I}_k \tag{5.5.3}$$

with

$$\vec{b}_{\mathrm{tot},S} = \vec{b}_{\mathrm{ext}} + \sum_k a_k \vec{I}_k \tag{5.5.4}$$

and

$$\vec{b}_{\mathrm{tot},I_k} = \zeta \vec{b}_{\mathrm{ext}} + a_k \vec{S} + 2q_k(\vec{n}_k \vec{I}_k)\vec{n}_k. \tag{5.5.5}$$

The same result can likewise be derived via path integral formalism [37,105]. With a bath of N spins, we end up with a system of $3(N+1)$ coupled linear differential equations. This can be solved by a number of schemes, but the results shown in this work were derived by a 4th order Runge-Kutta method[1].

Since the spins are modelled as freely rotating magnetic moments in the classical EOM, the spin length does not influence the dynamics except for a scaling factor.

Of course the expectation value cannot be computed quantum mechanically in the case of classical equation of motion. Here, the expectation value is obtained via a configuration average over all initial cofigurations [69,105]. The integral over the Bloch sphere [31,106] of each spin is realized in good approximation by taking the mean over a finite number N_c of randomly generated spin configurations.

[1]This was done by Natalie Jäschke. All results from the method of classical equations of motion in this work are her intellectual property and are presented in this thesis with her permission.

Chapter 6

Second-Order Correlation and Spin Noise

Second-order spin correlation is a well known quantity that has been extensively investigated in both theory and experiment. While the main focus of this thesis is fourth-order correlation functions, understanding the second-order electron spin correlation and electron spin noise is necessary for analyzing fourth-order correlation. This helps to identify which features of fourth-order correlation actually carry new information. Because second-order correlation is well studied, we can also use it to choose realistic parameters for simulation. A part of the results presented here have already been published or are currently in print, see Ref. [104, 107].

6.1 Distribution of Hyperfine Coupling Constants

As discussed in Sec. 3.1, the hyperfine coupling constants are given by the probability of the electron being at the location of the nuclei, see Eq. (3.1.20). We assume that in a d-dimensional QD the envelope of the electron wave function reads

$$\psi_e(\vec{r}) = C L_0^{-d/2} \exp\left(-\frac{|\vec{r}|^m}{2L_0^m}\right), \tag{6.1.1}$$

with $m = 1$ describing a hydrogen-like wave function and $m = 2$ a Gaussian envelope of the wave function. C is the dimensionless normalization constant. The dimension $d = 2$ describes self-assembled QDs where the size quantization along the growth axis is much stronger than that in the QD plane, while $d = 3$ is applicable to isotropic QDs. The distribution of the hyperfine coupling constants thus becomes

$$A_k = A_{\max} \exp\left(-\frac{|\vec{r}|^m}{L_0^m}\right). \tag{6.1.2}$$

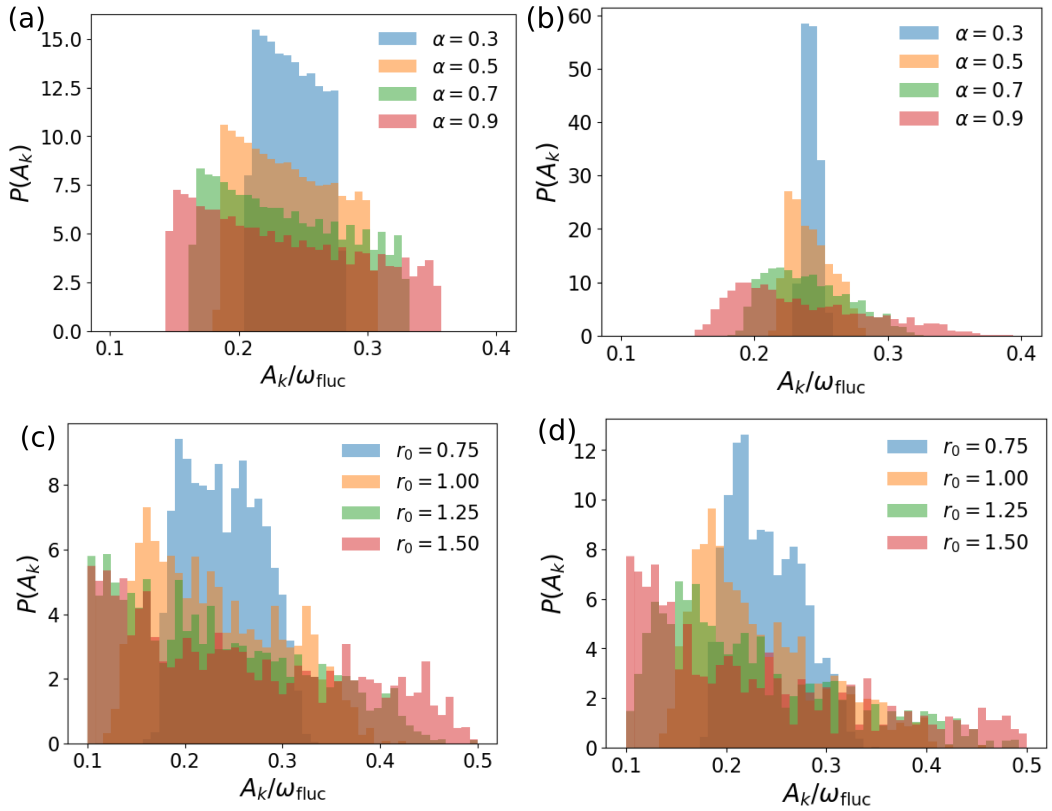

Figure 6.1: The empirical probability distribution of the coupling constants A_k for a bath of $N = 17$ nuclear spins, obtained by generating 10^6 sets of A_k. (a) and (b) show the distribution $A_{k,2}$ defined in Eq. (6.1.8) with a) $d = 2$ and b) $d = 3$. In (c) and (d) the distribution $A_{k,1}$ defined in Eq. (6.1.5) is presented, for (c) $d = 2$ and d) $d = 3$. A Gaussian envelope function is assumed ($m = 2$) in all panels.

There are several ways to implement an A_k distribution that fulfils Eq. (6.1.2), of which this work utilizes two.
First we present the coupling constant distribution derived and applied in [58]. We randomly pick a nuclear spin within a cut-off distance R_0 from the electron. That this random nuclear spin is at a distance r from the electron has the probability of $P(r) = dr^{d-1}R_0$. Using the relation $P(r)\mathrm{d}r = P(A)\mathrm{d}A$ yields

$$P(A) = \frac{d}{m}\left(\frac{L_0}{R_0}\right)^d \frac{1}{A}\left(\ln\left(\frac{A}{A_{\max}}\right)\right)^{d/m-1}, \tag{6.1.3}$$

the probability of picking a nuclear spin with the coupling constant A. This probability distribution is only defined between $A_{\min} = A_{\max}\exp(-R_0^m/L_0^m)$, since all nuclear spins beyond the cut-off radius R_0 are neglected, and the maximal possible coupling constant $A_{\max} = A_s\Omega C^2/L_0^d$. We define

$$\gamma(A_k) = \int_{A_k}^{A_{\max}} P(A)\mathrm{d}A \tag{6.1.4}$$

the probability of the selected nuclear spin having a coupling constant between A_k and $A_{\max}$. $\gamma(A_k)$ is a monotonous increasing function in the value range $[0, 1]$.

Rearranging for A_k yields

$$A_{k,1} = A_{\max} \exp(-r_0^m \gamma^{m/d}) \tag{6.1.5}$$

with $r_0 = R_0/L_0$. In this work, γ is randomly selected from a uniform distribution $[0, 1]$. The distribution of Eq. (6.1.5) was applied in Refs. [57–60].

The second approach to the coupling constant distribution proposed in Ref. [32] allows for a tighter control of the hyperfine couplings, which makes sure that a single particularly strong A_k doesn't dominate the dynamic. This makes it more suited for very small baths ($N < 10$). If the k-th nuclear spin lies at the distance r_k to the electron, and we assume that the nuclei density in the volume $r < L_0$ is by a factor α smaller than in the volume $r < r_k$, we obtain

$$\left(\frac{r_k}{L_0}\right)^d = \alpha \frac{k}{N}. \tag{6.1.6}$$

While it is not physical reality that the density of nuclear spins decreases with the distance to the electron, the density of non-negligible spins certainly does. Introducing the factor α allows us to discard more negligibly contributing nuclear spins, which is especially necessary for small baths. Inserting this relation into Eq. (6.1.2) yields

$$A_k = A_{\max} \exp\left(-\left(\alpha \frac{k}{N}\right)^{m/d}\right). \tag{6.1.7}$$

In order to introduce randomness, the exponent is varied by a uniformly distributed random number $z_k \in [0.5 : 0.5]$, which results in

$$A_{k,1} = A_{\max} \exp\left(-\left(\alpha \frac{k - z_k}{N}\right)^{m/d}\right) \tag{6.1.8}$$

and enables us to average over different sets of A_k. This randomisation preserves the relation $A_k > A_{k+1} \forall\, k$. If not otherwise specified, a 2-dimensional QD with a Gaussian electron wave function is studied, leading to an exponential $A_{k,2}$ distribution.

6.2 Central Spin Correlation

The second-order spin correlation $C_2(t) = \langle S_z(t) S_z \rangle$ and its features have been amply discussed in Ref. [85]. If no external magnetic field or interactions beyond the hyperfine interaction are present, $C_2(t)$ decays on the scale of $\mathcal{O}(T^*)$ and exhibits a local minimum at $t_{\text{dip}} \approx 3T^*$. After that it increases again to a value of about 1/12. Further decorrelation is governed by the distribution of the hyperfine coupling constants. If the hyperfine interaction constants are homogeneous ($A_k =$

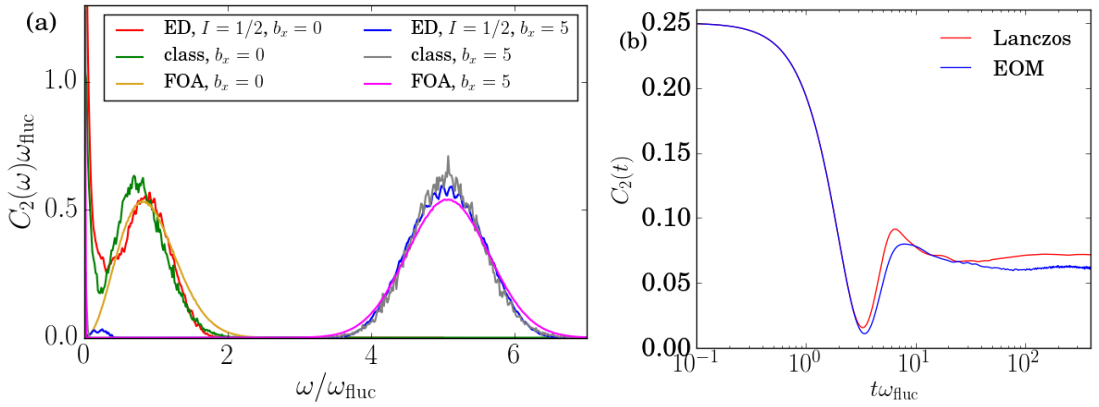

Figure 6.2: Panel (a): Comparison between the spin noise $C_2(\omega)$ for different approaches: the quantum mechanical ED simulation with $N = 13$ $I = 1/2$ nuclear spins, a classical EOM simulation of $N = 100$ spins and $C_2(\omega)$ computed in the FOA. Panel (b): $C_2(t)$ for $b_x = 0$ computed with a Lanczos with restarts for $N = 18$ spin $I = 1/2$ and an EOM simulation for $N = 100$ spins. Both have the same A_k distribution, following (6.1.5) with $r_0 = 1.5$. The EOM and the FOA data in the left panel has previously been published in Ref. [104].

$A_0 \, \forall k$) or the FOA holds, $C_2(t)$ stays at a constant $C_{\mathrm{lim}} = 1/12$. This has previously been discussed in Sec. 5.1 and Sec. 5.2.

A non-homogeneous distribution of hyperfine couplings leads to a long-time $\mathcal{O}(10^4 T^*)$ decay of correlation, whose exact dynamics depends on the spread of the hyperfine couplings [85, 108]. It has been shown [31] that the long-time limit of the central spin correlation depends solely of the ratio $u = \langle A_k^2 \rangle \, / \, \langle A_k \rangle^2$,

$$\begin{aligned} C_{\mathrm{lim}}(u) = & \frac{1}{6\pi}(u-1)^3 \int_0^\infty \mathrm{d}y\mathrm{d}z \frac{[2y\cosh(2y) - \sinh(2y)]^2}{yz\sinh(2y)} \\ & \times \exp\left[-(1+(u-1)^2)z^2 - \frac{y^2}{z^2}\right]. \end{aligned} \tag{6.2.1}$$

For $u = 1$, the limit becomes $C_{\mathrm{lim}} = 1/12$. This describes a system with homogeneous hyperfine couplings (box model). For an infinite spread of hyperfine couplings, $u \to \infty$, the limit of $C_2(t)$ is $C_{\mathrm{lim}} = 0$. Between $u = 1$ and $u \to \infty$, $C_{\mathrm{lim}}(u)$ monotonically decreases, as an increasing spread of hyperfine couplings leads to an increasing decorrelation. Introducing a larger transversal magnetic field ($b_x > 1$) changes this long-time behaviour, as $C_2(t)$ oscillates with the Larmor frequency around zero and decays with a Gaussian envelope in $\mathcal{O}(1T^*)$.

A basic understanding of spin noise, thoroughly investigated in Refs. [54, 57–59], can be achieved when using the Fourier transformation of the results from the FOA [31] expressed in Eq. (5.1.15) for $C_2(t)$, which is performed analytically in the case of $\vec{b} = 0$, resulting in

$$C_2(\omega) = \frac{1}{12}\left[2\pi\delta(\omega) + \omega^2(\sqrt{8}T^*)^3\sqrt{\pi}\mathrm{e}^{-2(\omega T^*)^2}\right]. \tag{6.2.2}$$

The spin noise spectrum was calculated for arbitrary magnetic fields by averaging the results of Eq. (5.1.13) over the number of configurations N_c.

Figure 6.2 (a) provides a comparison between $C_2(\omega)$ computed in the FOA, the classical EOM for $N = 100$ and ED for a small bath ($N = 13$) of $I = 1/2$ spins. The quantum mechanical ED and the classical EOM simulations show good agreement with the solution of the FOA for $b_x = 5$. The classical calculation traces the Gaussian envelope of the quantum mechanical spectrum and also differs from the FOA at $b_x = 0$. This is due to the nuclear spin dynamics included in Eq. (5.5.5) that causes an additional long-time decay in the time domain not included in the FOA. Therefore, the spectral weight shifts from the delta-peak at $\omega = 0$ to the Gaussian as the non-decaying fraction of $\langle S_z(t)S_z(0)\rangle$ decreases. At transversal magnetic fields $b_x > 1$, the spectrum takes the form of a Gaussian distribution $\mathcal{N}(\sqrt{b_x^2 + 1/2}, (\omega_{\text{fluc}}/2)^2)$.

$C_2(t)$ is shown for $b_x = 0$ and an A_k distribution following Eq. (6.1.5) with $r_0 = 1.5$ in Fig. 6.2 (b). Two different methods are compared, the Lanczos method with restarts and $N = 18$ nuclear spins (red) and classical EOM calculation for $N = 100$ spins. The difference in the dynamics is due to the relatively broad A_k distribution, that causes the number of effectively contributing spins to be lower than the actual number of simulated bath spins. While this does not influence the dynamics in a large bath of $N = 100$, it does cause a noticeable difference for $N = 18$.

6.2.1 Influence of the Hyperfine Coupling Distribution on Long-Time Spin Decay

Since the distribution of the hyperfine interaction constants governs the long-time decay of $C_2(t)$) for $b_x = 0$, it is sensible to investigate how the A_k distribution influences the spin dynamics.

Figure 6.3 presents the second-order correlation function $C_2(t)$ in the absence of a magnetic field, so that the long-time influence of the hyperfine distribution on the spin decay is made evident. The distribution is given by Eq. (6.1.5) with $d = 3$ and $m = 2$, for different relative cut-off radii r_0. It can be clearly seen that a broader A_k distribution (a larger r_0) causes a more pronounced decay.

It could be naively said that a large cut-off radius r_0 is better than a small one, since a larger variety of hyperfine couplings is taken into account. But when the bath size is limited, and a lot of small A_k are included, then only a few large A_k dominate the dynamics, reducing the effective bath size. For $N = 18$ and $r_0 = 1.5$, the biggest hyperfine coupling accounts for 25% of the dynamic. This has been successfully employed to model experimental results [59]. Therefore, $r_0 = 1.5$ is used when the influence of the bath size N is investigated in Fig. 6.4. On panel (a) the spin correlation for different bath sizes is shown for a nuclear spin length $I = 1/2$. While the curve progression of $C_2(t)$ is indistinguishable

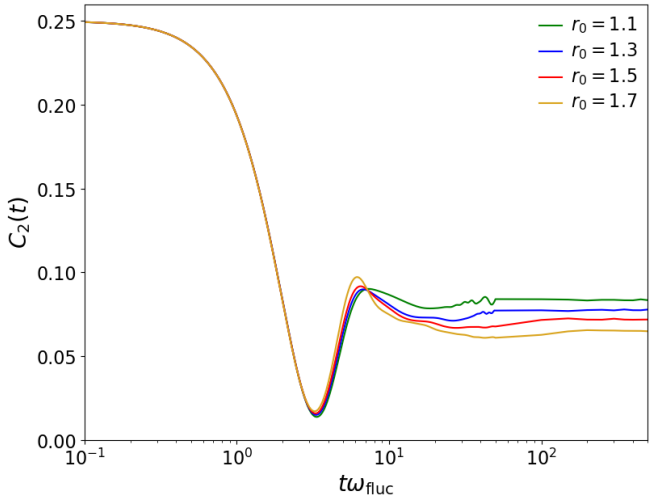

Figure 6.3: $C_2(t)$ for $I = 1/2$ computed via the Lanczos method with a Krylov depth of $M = 64$ and a distance between restarts of $\delta t = 50$. The magnetic field is absent and a hyperfine distribution following Eq. (6.1.5) with $d = 3$ and $m = 2$ was employed. The plot shows the influence of the relative cut-off radius r_0 with a bath size of $N = 18$. The curves result from a configuration average over 32 A_k distributions.

for the larger bath sizes $N = 15$ and $N = 18$, lower bath sizes show quite noisy behaviour. This is, however, not due to a low number of A_k, but a finite size effect caused by a small Hilbert space, as is shown in Fig. 6.4 (b). Here the results for $I = 3/2$ and different bath sizes are presented. While the finite size induced noise is absent, the spin correlation shows the effects of the limited bath size – $C_2(t)$ actually dips below zero for small N . This phenomenon is not observed in experiment in the absence of a magnetic field [53]. In a small bath, a broad hyperfine distribution causes a few nuclear spins to interact strongly with the electron, while the rest can be neglected. This reduces the effective bath size of contributing spins further. If the actual bath is small already, the effective bath size can come down to one or two nuclear spins that dominate the electron spin dynamic. In the extreme case of one electron and one nuclear spin, the result would be for $C_2(t)$ not to decay, but to oscillate around zero. The dip below zero in Fig. 6.4 (b) is a sign of one spin dominating at least in the short time regime, leading to the beginning of an oscillation.

Including quadrupolar interaction requires nuclear spin lengths larger than $I = 1/2$, which causes for a faster increase of the Hilbert space dimension with the bath size. The computation of higher order correlation limits bath size even further. Therefore, an A_k distribution has to be found that can deal better with small baths. An exponential hyperfine distribution was already used in Ref. [108] and has been derived in Eq. (6.1.8) for $m = 2$ and $d = 2$. The results are given by Fig. 6.5. In Fig. 6.5 (a) one can see the behaviour of $C_2(t)$ with an exponential hyperfine coupling distribution for different parameter α. The decay of the spin correlation once again is stronger for a broader distribution (larger α), but the effect is not as pronounced as seen in Fig. 6.3. For $\alpha = 0.3$ finite size effects are

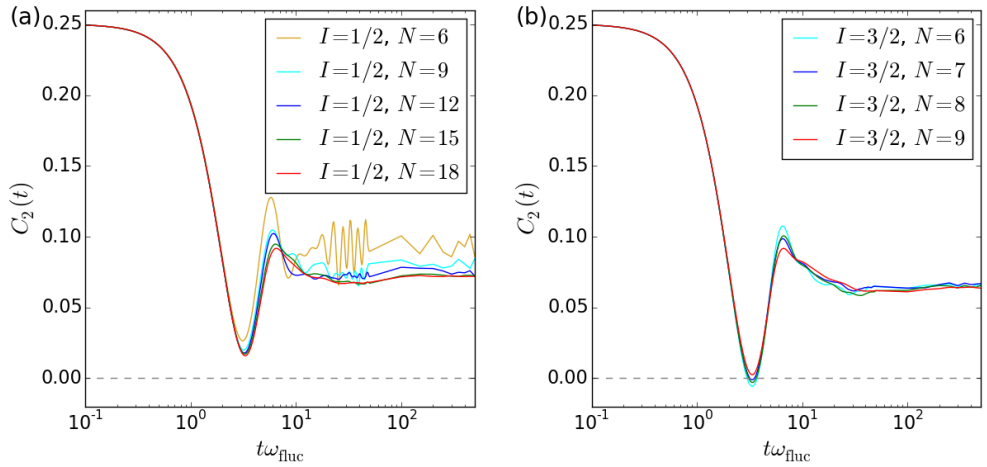

Figure 6.4: $C_2(t)$ computed with the same parameters M, δt and the same A_k distribution as in Fig. 6.3 for $r_0 = 1.5$. Panel (a) shows different bath sizes for the nuclear spin length $I = 1/2$, while panel (b) does the same for $I = 3/2$.

clearly visible. At $\alpha = 0.3$ the distribution is quite close to homogeneous coupling $A_k = A_0$, which causes stronger finite size effects.

It becomes clear why the exponential distribution is preferable to the previously discussed distribution in the case of small bath sizes. In Fig. 6.5 the resulting spin correlation for $I = 3/2$, $\alpha = 0.5$ and different bath sizes are plotted. While the $N = 6$ curve does betray some finite size effects, the spin correlations show a more homogeneous curve progression than seen in Fig. 6.4 (b). Furthermore, the correlation never dips below zero, meaning that a significant number of nuclear spins contribute effectively to the dynamic. In order to produce relevant result and to minimize the influence of the limited bath size, the exponential hyperfine coupling distribution as defined in Eq. (6.1.8) is used for bath sizes $N < 10$, unless otherwise stated. Since the hyperfine coupling distribution derived for the three dimensional QD as shown in Eq. (6.1.5) has produced good results for large baths [58], this distribution will be occasionally presented as well, to form a connection to previous work using it. A more in-depth discussion on the influence of the A_k distribution on the long-time decay of $C_2(t)$ can also be found in Refs. [54, 58, 106].

6.2.2 Influence of Quadrupolar Coupling on Spin Correlation

Quadrupolar interaction only plays a role for bath spin lengths $I \geq 3/2$, since the quadrupolar moment of $I = 1/2$ is zero. As the Hilbert space grows with $(2I+1)^N$, less bath spins can be simulated for larger I. Where the computations without quadrupolar coupling were done with $N = 18$ spins of length $I = 1/2$, the computations with quadrupolar coupling simulate a system with $N = 9$ spins and $I = 3/2$.

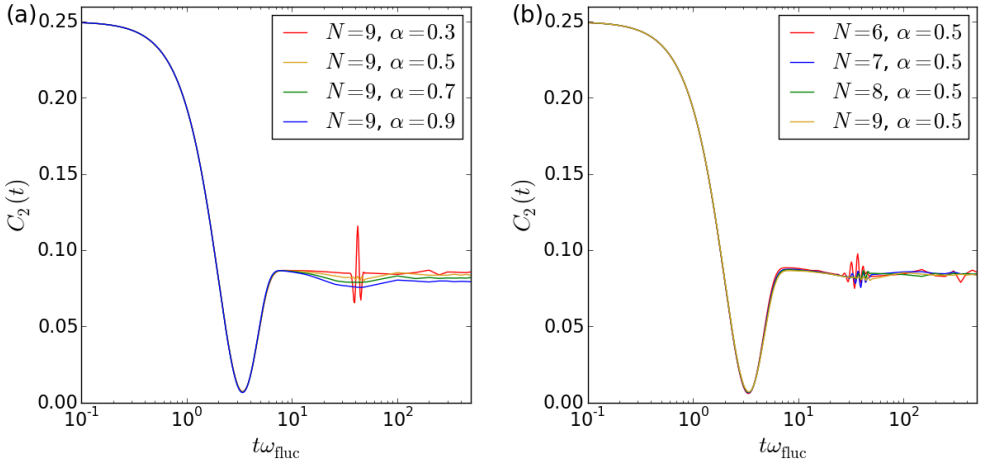

Figure 6.5: $C_2(t)$ for $I = 3/2$ computed with the same parameters M, δt and the A_k distribution given in Eq. (6.1.8). Panel (a) shows $C_2(t)$ for $N = 9$ and varied α, while in panel (b) N is varied while $\alpha = 0.5$.

The effect of the quadrupolar interaction included in H_Q, Eq. (3.3.7), is determined by the overall quadrupolar strength Q_r, the distribution of the quadrupolar coupling constants q_k, the anisotropy η, the distribution of the local nuclear easy axis and the nuclear spin length I. For the distribution of q_k, the anisotropy η and the nuclear easy axis $\vec{n}_k^z$ this work follows Refs. [59, 87] by using the parameters $\eta = 0.5$ and $\theta_{\max} = 35^\circ$ as stated in Sec. 3.2.

When adding the quadrupolar coupling to the central spin model, it is important to understand its influence on the long-time decay of $C_2(t)$ as a function of the nuclear spin length I. The relative strength Q_r defined in Eq. (3.3.8) has been originally introduced in Ref. [59] to minimize the dependency on the bath size N. There is clear experimental evidence [59, 72] that H_Q induces a decay of $C_2(t)$ on time scales of $200 - 600$ns that depends on the growth conditions of the QD ensemble.

The long-time behavior of $C_2(t)$ under the influence of the quadrupolar interaction in the absence of an external magnetic field can be accurately computed by the Lanczos method with restart as detailed in Sec. 5.4.3. The time evolution is shown for five different values for Q_r for a relatively large bath of N=9 nuclear spins with $I = 3/2$ in Fig. 6.6 (a) on a logarithmic time scale. The Lanczos results reproduce the previous results obtained with Chebychev polynomial approach [59]. Comparing theoretical curves for the spin-spin correlation function with the direct measurement of C_2 [53] yields $Q_r \approx 0.15$. This value for the quadrupolar coupling strength is very close in magnitude to the parameter used in Ref. [57] to explain spin-noise data obtained for modeling different InGaAs QD samples.

The influence of the quadrupolar interaction is not only determined by the quadrupolar coupling strength Q_r, but also by the nuclear spin length I. In Fig. 6.6 (b) the value of Q_r is chosen for each spin length I such that $C_2(t)$ remains

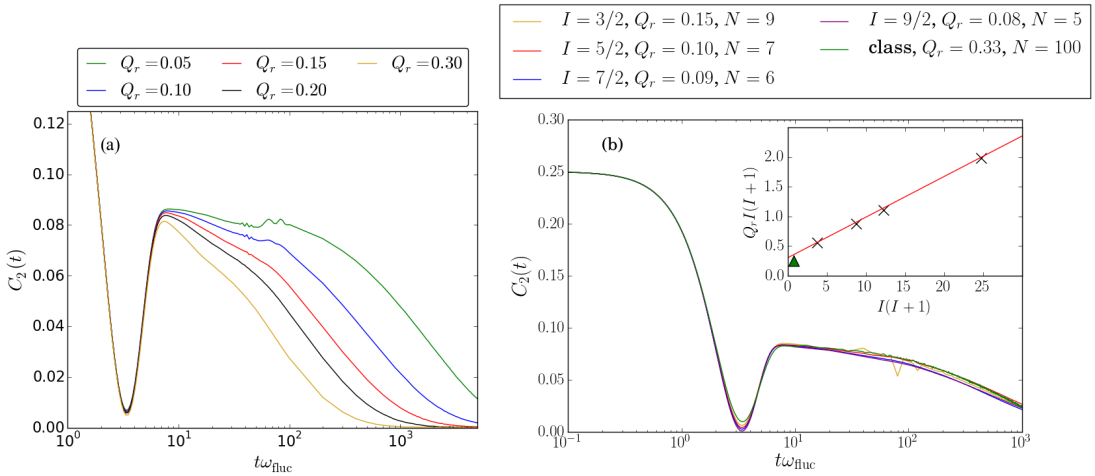

Figure 6.6: Panel (a): $C_2(t)$ computed by Lanczos method with restart with $N = 9$ nuclear spins and no magnetic field. The strength of the quadrupolar interaction is varied to determine an experimentally relevant value of Q_r. Panel (b): The second-order spin correlation in the absence of a magnetic field computed by a Lanczos algorithm, with different spin lengths I, bath sizes N and interaction strengths Q_r, chosen for similar long-time decay. The inset plot shows the dependence of $Q_r I(I+1)$ on the squared spin length $I(I+1)$. The hyperfine couplings are homogeneous. In both panels $C_2(t)$ is the result of averaging over 32 sets of hyperfine coupling constants. Figures taken from [104, 107].

invariant. Establishing this gauge will help to compare the differences in the fourth-order correlation with different bath spin lengths I. Figure 6.6 (b) depicts the second-order correlation function $C_2(t)$ for different I but similar Hilbert space dimensions $\mathcal{D}$, with an adjusted Q_r. In order to connect the quantum mechanical Lanczos results to the classically computed $C_2(t)$, the anisotropy factor is set to $\eta = 0$. This is because the classical EOM method only simulated isotropic quadrupolar coupling in Ref. [104]. Plotted alongside the results of the Lanczos method for different I is the $C_2(t)$ computed with a classical EOM method as detailed in Eqs. (5.5.3) to (5.5.5). When the spin is modelled as a classical magnetic moment, spin length becomes just a scaling factor in the EOM. Here it is set to $I_{\mathrm{eom}} = 1/2$. It turns out that a classical approach is very much able to model the influence of quadrupolar interaction on the second-order spin correlation with a properly adjusted Q_r. To make sure that only the quadrupolar interaction influences the long-time dephasing for $t \gg T^*$, the data in Fig. 6.6 (b) was computed in a box model.

For $I = 3/2$, the quadrupolar coupling strength is set to $Q_r = 0.15$. Q_r was chosen for $I = 5/2$, $7/2$ and $9/2$ (marked by 'x' in the inset of Fig. 6.6 (b)) so that all correlation functions exhibit a similar long-time decay. Interestingly, the Q_r that achieve this agreement of $C_2(t)$ for these different combinations of I and

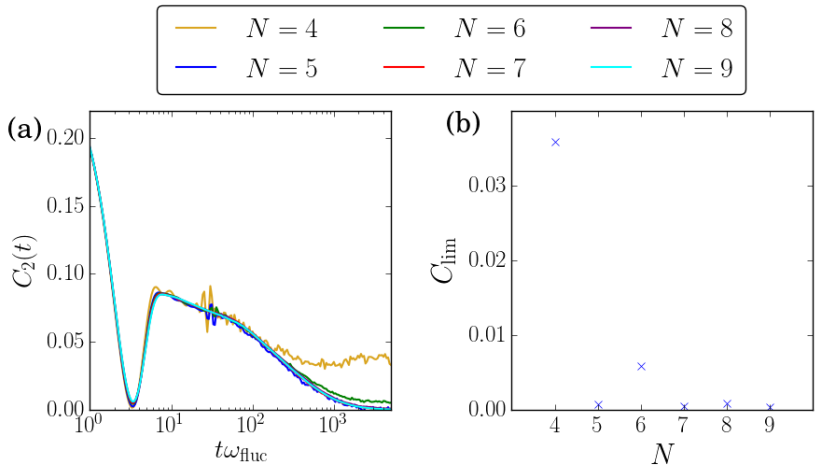

Figure 6.7: Panel (a): $C_2(t)$ with a quadrupolar coupling strength of $Q_r = 0.15$, no magnetic field and a varying number of nuclear spins with the length $I = 3/2$. It was averaged over the results of $N_a = 32$ different sets of A_k. The long-time limit shows an even-odd behavior in regard to bath size, as shown panel (b). The data in both panels has been published in [107].

N obey the phenomenological relation

$$Q_r I(I+1) = aI(I+1) + b, \tag{6.2.3}$$

with $a = 0.068 \pm 0.002$ and $b = 0.30 \pm 0.03$ obtained via linear regression. The classical computations of $C_2(t)$ that have been made for an effective spin vector length of $I = 1/2$ follow this relation roughly (marked by a triangle in the inset plot).

Due to computational constraints, the number of nuclear spins that can be computed with a full quantum mechanical central spin model is limited. Therefore, it is advisable to determine the finite size effects of a small nuclear bath. In Fig. 6.7 (a) the second-order correlation for different bath sizes, a spin length $I = 3/2$ and a fixed quadrupolar coupling of $Q_r = 0.15$ is compared. It demonstrates the fast convergence of $C_2(t)$ with N, as all $C_2(t)$ for $N \leq 7$ are indistinguishable. While $C_2(t)$ can be calculated exactly for a bath size as large as $N = 9$ with a Lanczos method with restart without any problem, this is impossible for fourth-order correlation functions due to the scaling of the nested Lanczos algorithm with the exponential growth of the Hilbert space with N. A finite size analysis for $C_{\text{lim}} = C_2(t \to \infty)$ is depicted in Fig. 6.7 (b). Clearly visible are even-odd oscillations which approach $C_{\text{lim}} = 0$ at large N within a numerical error of $\mathcal{O}(10^{-4})$. Odd numbered bath sizes converge at much smaller bath sizes. For odd numbered bath sizes $C_2(t)$ shows a full decay, since an even total number of spins allows for singlets to form. This is something to keep in mind when computing and discussing fourth-order correlation.

6.3 Nuclear Spin Bath Auto-Correlation

While we focused on electron spin decay before, nuclear spins also provide a sizable contribution to the Faraday effect in semi-conductors [109,110]. Nuclear spin fluctuations have recently been observed in a GaAs bulk sample with electrons bound to Si-donors [52]. Similarly to QDs, such a system can be described via the CSM, as long as the donors are spaced far enough apart so that the electron wave functions do not overlap.

The observation of nuclear spin contributions in spin noise spectra motivates us to investigate the nuclear spin fluctuations in a system where an electron is either localized in a QD or bound to a neutral donor. While electron spin noise has been widely studied, nuclear spin fluctuations in the central spin model have not been.

In this chapter, two analytical methods and one numerical method are employed in order to describe the behaviour of the nuclear spin bath correlation and noise. The results presented in this section have been published before in Ref. [111].

6.3.1 Nuclear Spin Bath Auto-Correlation in the Box Model

The nuclear spin bath dynamics, characterized via the sum of all nuclear spins $\vec{I} = \sum \vec{I}_k$, is influenced by two fields: the Knight field generated by the hyperfine coupling with the electron spin and the external magnetic field due to the nuclear Zeeman energy. We derived an analytical expression for the total spin bath correlation $\langle I_x(t) I_x \rangle$ with a transversal field in the box model, see Eq. (5.2.19). Fourier transformation of the spin bath correlation yields the spin bath noise.

The nuclear spin noise is shown in the absence of a nuclear Zeeman term ($\zeta \equiv 0$) for different magnitudes of the transversal magnetic field in the left panel of Fig. 6.8. As the spectra are even functions, only the region $\omega \geqslant 0$ is plotted. In the box model, $a_k \propto 1/\sqrt{N}$. Both the correlation of the total nuclear spin bath $\langle I_x(t) I_x \rangle$ and the bath spin noise $(I_x^2)_\omega$ grow linear with the bath size. To ensure comparability between results from different bath sizes, the spin noise and the spin correlation are scaled with N.

The influence of the hyperfine interaction on the nuclei is negligible without a magnetic field. This can be inferred from the spectrum, since its only feature is a single Lorentzian peak at $\omega = 0$, broadened as described in Eq. (5.2.22). In the absence of a magnetic field the total spin $\vec{F}$ is conserved at $F^2 = (N+1)/4$ and the electron spin correlation stays constant at $1/12$ for long times in the box model. Therefore, $\langle I_x(t) I_x \rangle$ is constant as well for times $t\omega_{\text{fluc}} > 10$, remaining at a value of $I^2 = (3N+2)/12$.

Figure 6.8 (a) shows that the peak shifts frequency without nuclear Zeeman splitting and with increasing magnetic field strength. At high magnetic field

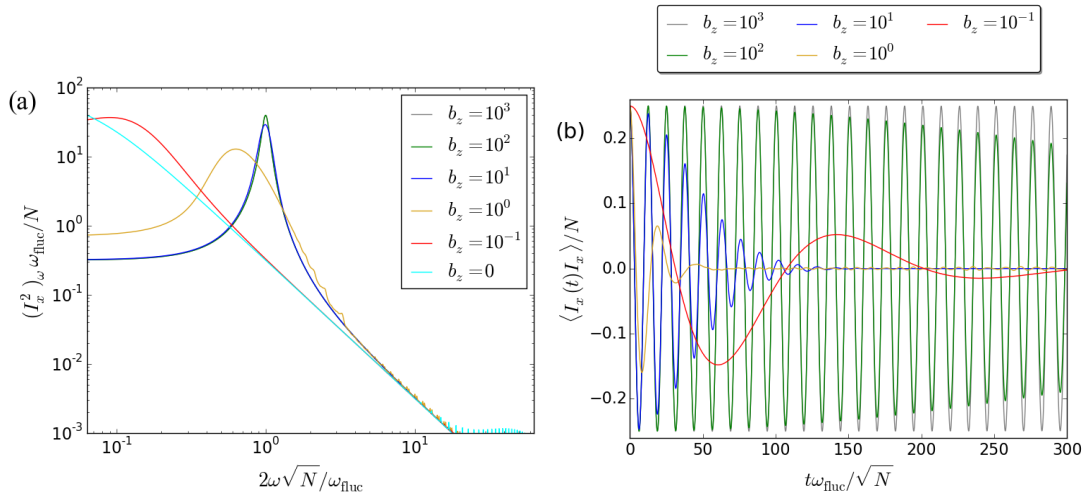

Figure 6.8: The nuclear spin noise $(I_x^2)_\omega$ (panel (a)) and the spin bath correlation (panel (b)) for different transversal external magnetic fields b_z and a bath size of $N = 1000$, computed within the box model as derived from a Fourier-transformation of Eq. (5.2.19). The nuclear Zeeman splitting is set to zero. Data shown in panel (a) has been previously published in [111].

$h \gg 1$, the peak in the spectrum shifts to $\omega^* = a_0/2$ $[\omega^* T^* = 1/(2\sqrt{N})]$, which shows the precession in the Knight field.

The dynamics of the total spin bath in the time domain can be seen in Fig. 6.8 (b). At strong magnetic fields, decoherence is suppressed in favour of the Knight field precession. At $b_x = 1000$, no decay of the maximum amplitude is observed on a given time scale, while the envelope of $b_x = 10, 100$ still decreases noticeably in the plotted time frame. Note that quite small transversal magnetic fields ($b_x = 0.1$) already cause a total decay of the spin bath correlation, when in the absence of a magnetic field it remains at a constant non-zero value. This is because the total spin is no longer conserved and the nuclear spins precesses in the Knight field generated by the electron spin.

Figure 6.9 (a) depicts the nuclear spin noise obtained from the Fourier transformation of Eq. (5.2.19), with the finite Zeeman ratio $\zeta = 0.001$. For weak magnetic fields, $\zeta b_z \ll a_0$, the influence of the nuclear Zeeman term on the nuclear spin noise spectra is negligible. The effect of ζ can be observed as a shift of the peak only for $\zeta b_z > 1/\sqrt{N}$. When increasing the magnetic field, a double peak structure centred around $\omega = a_0/2$ emerges, with the peak splitting determined by the nuclear Zeeman energy. At higher magnetic fields, $\zeta b_z \gg a_0$, the spin noise spectrum exhibits two closely lying peaks centered at $\omega = \zeta b_z$, where the distance between the peaks is equal to a_0. This can be derived analytically, when applying the high magnetic field limit as shown in the next section.

In Fig. 6.9 (v) the time dependent dynamics of the total spin bath correlation is shown. While the nuclear Zeeman splitting has no effect for small fields, at

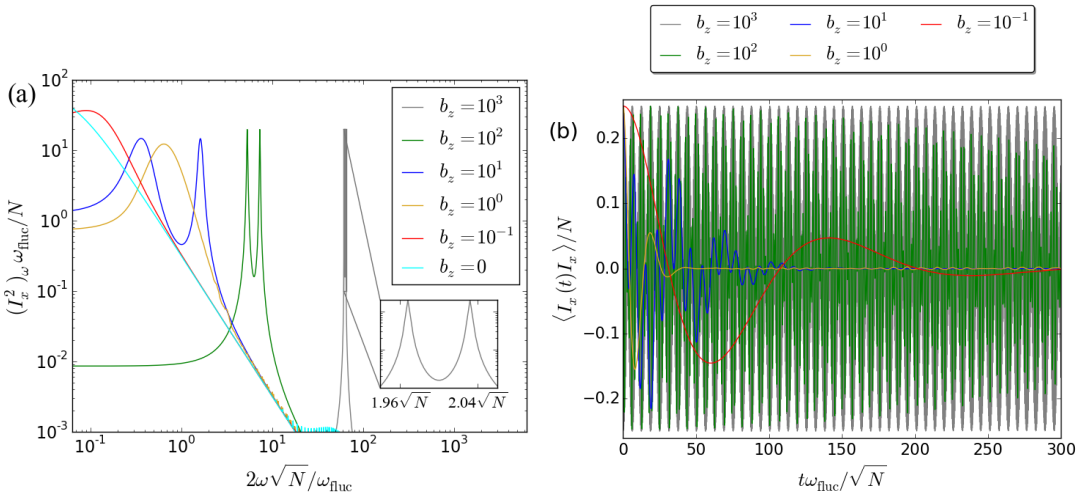

Figure 6.9: The nuclear spin noise $(I_x^2)_\omega$ (panel (a)) and the spin bath correlation (panel (b)) as plotted in Fig. 6.8, but the ratio of nuclear to electron Zeeman splitting is $\zeta = 10^{-3}$. This plot in panel (a) has been previously published in [111].

high magnetic fields a beat can be observed due to the precession in both the Knight field and the external magnetic field. The nuclear spin noise is not only dependent on applied magnetic field strength or nuclear Zeeman energy, but on total bath size as well, since the characteristic energy scale of the hyperfine coupling decreases with $a_k \propto 1/\sqrt{N}$. This is illustrated in Fig. 6.10. It shows the Fourier transform of Eq. (5.2.19) for the constant product $b_z\sqrt{N} = 300$. An increasing number of bath spins causes the energy spectrum to broaden, reflecting the bath noise spectrum.

The disadvantage of the box model is obviously that it cannot include a distribution of coupling constants. Also, it is not possible to extend the Hamiltonian to additional interactions such as quadrupolar interaction if necessary and still employ this analytical method.

6.3.2 Nuclear Spin Bath Auto-Correlation in the High Magnetic Field Limit

In this section an analytical approach for describing spin correlation and noise in the limit of large magnetic fields and a distribution of hyperfine coupling constants is presented. At very high magnetic fields, spin flips are suppressed, leading to the effective Hamiltonian

$$H_{\mathrm{hmf}} = b_z S_z + b_z \sum_k \zeta I_z + \sum_k a_k I_z S_z. \tag{6.3.1}$$

describing the high magnetic field limit (hmf). This Ising-like coupling can also be used to model QDs with very heavy holes in an arbitrary magnetic field, see

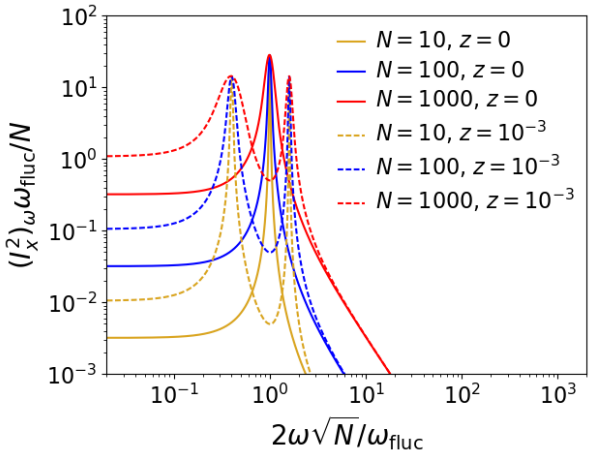

Figure 6.10: The nuclear spin noise for different bath sizes, with and without nuclear Zeeman splitting, obtained by the Fourier transformation of Eq. (5.2.19). The external magnetic field is varied with the bath size, $h\sqrt{N} = 300$ being kept constant. The spin noise is scaled with N in order to make the plots comparable. Data here has been previously published in [111].

Eq. (3.1.15) and Ref. [34,38,112]. In this case, the Hamiltonian (6.3.1) is diagonal in the Ising basis and $\langle I_x(t) I_x(0)\rangle$ is given by

$$\begin{aligned}\langle I_x(t) I_x(0)\rangle =& \frac{1}{4Z} \sum_{\substack{k=1,\\ L_k=\uparrow,\downarrow,\sigma=\uparrow,\downarrow}}^{N} \langle \sigma, \{L_k\}| I_k^x(t) I_k^x(0) |\sigma, \{L_k\}\rangle \\ =& \frac{1}{4}\sum_k^N \cos(a_k t/2)\cos(\zeta b_z t).\end{aligned} \tag{6.3.2}$$

For homogeneous hyperfine couplings, $a_k = a_0\, \forall k$, the nuclear spin noise spectrum exhibits four peaks at $\pm(a_0/2 \pm \zeta b_z) = \pm a_0(1/2 \pm \zeta b_z\sqrt{N})$. This explains the peak structure emerging for large fields seen in the last section in Fig. 6.9 (a). The nuclear spin bath precesses in the Knight field of the strength a_0 for $\zeta = 0$.

In the high magnetic field limit the summation over k in Eq. (6.3.2) can be performed analytically in the large N limit, and nuclear spin noise spectrum acquires the form

$$(I_x^2)_\omega = \frac{\pi N}{4}\int da \mathcal{P}(a)\left[\delta(\omega - a/2) + \delta(\omega + a/2)\right], \tag{6.3.3}$$

where $\mathcal{P}(a)$ is the distribution function of the coupling constants a_k, as defined by Eq. (6.1.3).

The Fourier transformation of Eq. (6.3.2) yields the nuclear spin noise, which is plotted without nuclear Zeeman splitting in Fig. 6.11 (a). The results of the box model at $b_z = 1000$ including all spin flips matches the high magnetic field limit

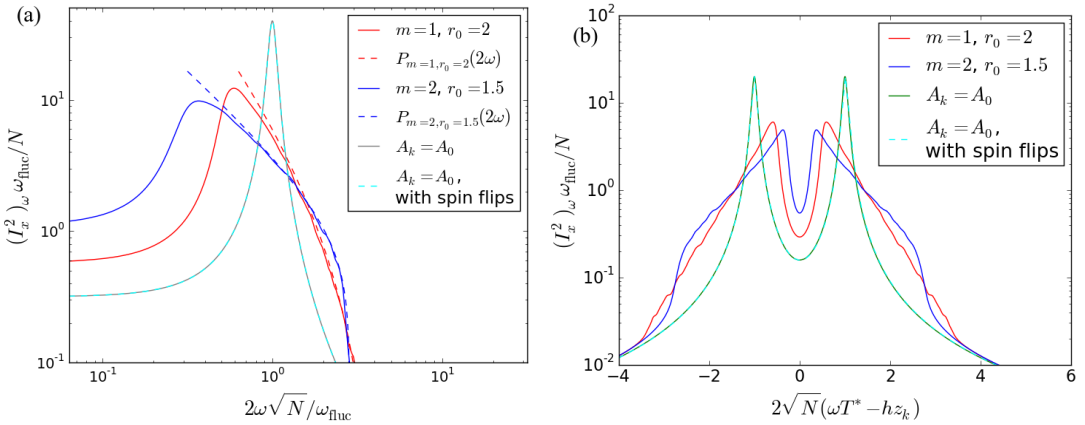

Figure 6.11: The nuclear spin noise obtained from the Fourier transformation of Eq. (6.3.2) at the high magnetic field limit for Ising coupling (continuous lines) and a bath size of $N = 1000$. In panel (a), ζ is zero, in panel (b) $\zeta = 10^{-3}$. Plotted are three different hyperfine coupling distributions, one with constant couplings and another one following Eq. (6.1.5) with $m = 1, r_0 = 2$ and $m = 2, r_0 = 1.5$. For comparison, the spin noise with spin flips, $b_z = 1000$, and constant $a_k \equiv a_0$ is added with a dashed light blue line. In panel (a) the a_k distribution function $\mathcal{P}(2\omega)$ obtained via Eq. (6.1.3) is also provided for $m = 2, r_0 = 1.5$ (blue dashed line) and $m = 1, r_0 = 2$ (red dashed line). The spin noise was averaged over 10 sets of a_k distributions. Plots are taken from Ref. [111].

perfectly, justifying the use of the Ising model. The nuclear spin noise calculated within the box model with (light blue dashed curve) and without (green curve) spin flips can be found in the Fig. 6.11 (a). One can infer from Eq. (6.3.3) that the nuclear spin noise spectrum becomes

$$(I_x^2)_\omega = \frac{\pi N}{2}\mathcal{P}(2\omega), \quad \omega > 0 \tag{6.3.4}$$

for $\gamma \to 0$. Analogous to the approach in the box model, the δ-peaks of the nuclear spin noise were broadened to a Lorentzian with $\gamma T^* = 0.001$.

Figure 6.11 (a) also presents a comparison of the nuclear spin noise between the Fourier transformation of Eq. (6.3.2) for $N = 1000$ nuclear spins with $\zeta = 0$ and the continuum limit of Eq. (6.3.4). The analytical curves calculated via Eqs. (6.1.3) and Eq. (6.3.4) are plotted as dashed lines of the same color. They are congruent with the numerical results of Fourier transformation of Eq. (6.3.2) for $\omega > 0.01$. The dimensionless cut-off radius r_0 defines the smallest a and the distribution function of hyperfine couplings is only valid for $a > a_{\rm min}$, having a singularity at $a = 0$ [58]. The analytical and numerical solutions agree very well for the same hyperfine coupling parameter m and r_0 at high frequencies. The difference for $\omega \to 0$ arises from the hard cut-off of $\mathcal{P}(a)$ versus finite Lorenzian broadening of the numerical solution for a finite number of nuclei.

Figure 6.11 (b) shows the nuclear spin noise in the high magnetic field limit including a finite $\zeta = 0.001$, again derived through the Fourier transformation

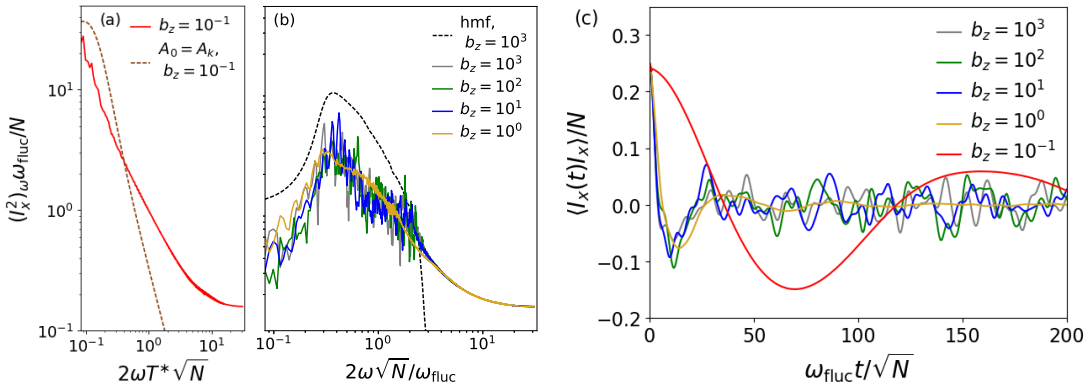

Figure 6.12: The transversal nuclear spin noise computed with the Lanczos method for $N = 17$ nuclear spins and a Krylov space dimension of $M = 800$ and $\zeta = 0$. The a_k distribution is based on a Gaussian electron wave function $m = 2$. For better comparison the results for a low magnetic field are shown in (a) as well as the spectra obtained for the box model at a small magnetic field of $b_z = 0.1$ (in a brown dashed line). In (b) the spin noise for higher magnetic fields is depicted, along with the high magnetic field limit in a black dashed line. Panel (c) shows the corresponding real time dynamics of the spectra calculated with the Lanczos method. The data plotted in panel (a) and (b) has been published previously in Ref. [111].

of Eq. (6.3.2). As for $\zeta = 0$, the box model results with and without spin flips agree perfectly, which stresses the validity of the use of the Ising model for high magnetic fields.

The spectra again exhibit a two peak structure centred at the nuclear Zeeman energy $b_z\zeta$. The distribution of hyperfine couplings generates an additional broadening, which is clearly observable in the modified shape of curves for the two distributions of a_k, with $m = 1$ and $m = 2$.

An interesting takeaway of this analysis of the high magnetic field limit is the possibility of measuring the distribution of the hyperfine coupling constants at high magnetic fields directly via spin noise spectroscopy, using Eq. (6.3.4). Since the peaks are centred around $b_z\zeta$, the hyperfine coupling distributions can even be assigned to the different isotopes present in the probe.

6.3.3 Nuclear Spin Correlation in the Central Spin Model

While the high magnetic field limit and the analytical solution of the box model have the advantage of simulating a large number of spins at low computational cost, a numerical approach based on the Lanczos method with restart can model inhomogeneous hyperfine couplings at arbitrary magnetic fields, and also allows to incorporate additional interactions, such as the nuclear quadrupolar electric coupling [59,61,107]. Since the Hilbert-space dimension grows exponentially with the bath size, the number of nuclear spins is severely limited in this approach.

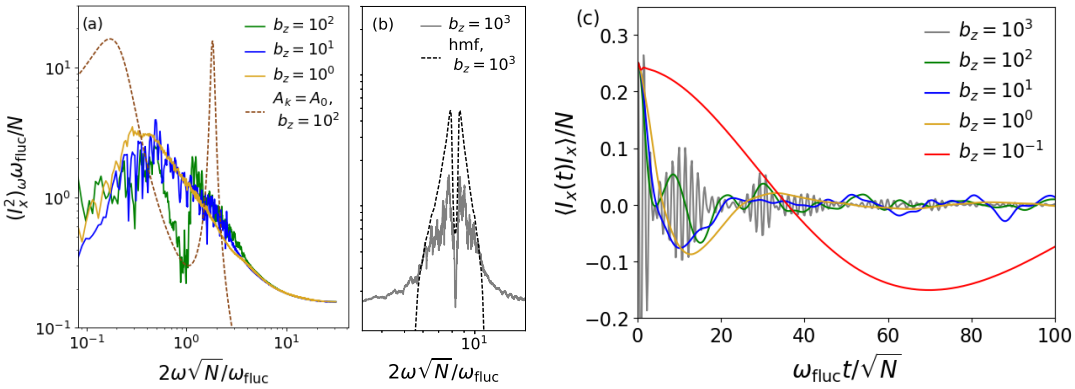

Figure 6.13: The transversal nuclear spin noise computed for the same parameters as in Fig. 6.12, but including the electron Zeeman splittings by setting $\zeta = 10^{-3}\,\forall\, k$. As with Fig. 6.12, the low magnetic field spin noise is plotted in (a), while the high magnetic field spin noise, exemplary for $b_z = 10^3$, is shown in (b). Also depicted in (a) is the box model solution for $b_z = 10^2$ in a dashed brown line. The high magnetic field limit is added to (b) for $b_z = 10^3$ for comparison with the full model. Panel (c) shows the corresponding real time dynamics of the spectra calculated with the Lanczos method. The data plotted in panel (a) and (b) has been published previously in Ref. [111].

Here, $N = 17$ spins with $I = 1/2$ are simulated, and the a_k distribution introduced in Eq. (6.1.3) is used with a cut-off radius of $r_0 = 1.5$ and $m = 2$.

A numerical Fourier transformation is performed over the real-time dynamics of the nuclear spin bath, which yields the corresponding nuclear spin noise spectra. This is different from the previous analytical methods where the spectra were obtained directly. In order to counteract finite size problems caused by the limited number of nuclear spins, 25 different sets of hyperfine couplings were generated to perform a configuration average over the resulting spectra.

The nuclear spin noise spectra in a transversal magnetic field obtained by the Lanczos method are plotted with $\zeta = 0$ in Fig. 6.12 and with $\zeta = 0.001$ in Fig. 6.13.

Figures 6.12 (a) and (b) show the spin bath spectra for small and large magnetic fields, respectively. In Fig. 6.12 (a) the box model spectrum Eq. (5.2.19) is plotted alongside for comparison.

For high magnetic fields, as seen in Fig. 6.12 (b), the spectra qualitatively resemble the analytical results given previously in the high magnetic field limit for $b_z > 1$ and the same hyperfine distribution. Without a nuclear Zeeman term, the bath spin noise spectra center around the Knight field frequency, as shown in Eq. (6.3.2). At a fixed Overhauser frequency ω_{fluc}, the Knight field strength decreases relative to the Overhauser field with an increasing number number of nuclear spins. Therefore, the main spectral weight is centered around a smaller frequency for $N = 1000$ bath spins compared to $N = 17$. Thus the frequency axis is rescaled with the factor $2T^*\sqrt{N}$. While the full numerical solution shows a

broader spectrum than the box model results, for $b_z > 1$ the high magnetic field limit exhibits the same qualitative form as the nuclear spin noise results from the full model. Since the smaller number of nuclear spins severely decreases the number of discrete eigenvalues of the system, and the fast Fourier transformation of the real time dynamics from the Lanczos algorithm was not smoothed by additional Lorentz broadening, the resulting spectra are more noisy than those discussed in the two previous sections. Panel (c) of Fig. 6.12 shows the Lanczos real time dynamics. While in smaller magnetic fields the spin bath correlation is similar to the box model solution, at higher magnetic fields the decay caused by the inhomogeneity of the hyperfine couplings becomes apparent.

Accounting for the nuclear Zeeman splitting causes significantly different spectra for $b_z > 10$. In Fig. 6.13 (a) and (b) the transversal nuclear spin noise is depicted with a finite $\zeta = 10^{-3}$ and otherwise identical parameters. A local minimum becomes apparent in Fig. 6.13 (a) for $b_z\zeta = 0.1$, a feature shared with the box model result added in a dashed brown line. For $b_z\zeta = 1$ the nuclear Zeeman splitting causes the same two-peaked structure already observed by the analytical results in the high magnetic field limit. To stress this point, the analytically calculated spectrum for $b_z = 1000$ and the same hyperfine coupling distribution is plotted in a dashed black line alongside the Lanczos result in Fig. 6.13 (b).

When comparing the results of the full CSM with the two analytical approximations presented, one can conclude that both the box model and the high magnetic field limit allow for an adequate understanding of the features of the bath spin noise. An immense advantage of the analytical techniques is the severely decreased computational cost even at much larger bath sizes, while the Lanczos method allows for greater flexibility in both the interactions included and the parameter range evaluated.

6.4 Chapter Conclusion

In this chapter two kinds of second-order spin correlation, the correlation of the electron spin and the correlation of a component of the total nuclear spin vector in a nuclear spin bath, were examined for a transversal external magnetic field.

Two kinds of hyperfine distribution function were derived in Sec. 6.1, both useful for simulating the systems dynamics with only a limited bath size. The distribution given by Eq. (6.1.5) describes accounting for all spins within a relative cut-off radius r_0, while the distribution presented in Eq. (6.1.8) assumes that the density of non-negligibly contributing spins decreases by a factor $\alpha < 1$ with the distance to the electron.

Sec. 6.2 deals with the second-order correlation $C_2(t) = \langle S_z(t)S_z\rangle$ and its counterpart in the frequency domain, the spin noise spectrum $C_2(\omega)$. Firstly, their general features were presented. Then the influence of the two different hyperfine coupling distributions on the systems dynamics were investigated. Both have

their merits and shortcomings, with the exponential A_k distribution defined in Eq. (6.1.8) with $\alpha = 0.5$, $d = 2$ being more advantageous for small baths $N < 10$, and the non-exponential distribution as given by Eq. (6.1.5) with $r_0 = 1.5$ and $d = 3$ being better for simulating large baths $N > 10$. Secondly, the influence of the quadrupolar coupling on the electron spin correlation function was examined. The long-time decay of $C_2(t)$ for different quadrupolar coupling strengths Q_r, nuclear spin lengths I and bath sizes N was discussed. A phenomenological connection between the nuclear spin length I and Q_r was found and quantified. An even-odd behaviour of the long-time decay of $C_2(t)$ regarding the bath size was observed.

In Sec. 6.3 the nuclear spin bath auto-correlation $I(t)$ and the spin bath noise $(I_x^2)_\omega$ were investigated. While the nuclear spin dynamics are frozen in the FOA, an analytical method for describing the spin bath correlation can be found in the case of homogeneous hyperfine couplings. It reveals that the nuclear spins precess in the Knight field generated by the hyperfine coupling with the electron. In the case of a finite nuclear Zeeman energy and a sufficiently large external magnetic field, the nuclear spin correlation is dominated by the Zeeman splitting. Even for inhomogeneous hyperfine coupling constants, an analytical solution exists for large magnetic fields, as the magnetic field induced suppression of spin flips creates an Ising-like system. We have shown that this makes it possible to measure the distribution of hyperfine coupling constants directly via spin noise spectroscopy as the broadening of the Zeeman energy peak. Quantum mechanical simulation for a limited nuclear spin bath was able to show the veracity of both analytical methods in their respective regimes.

Chapter 7

Fourth-Order Spin Noise

The electron spin, which is a candidate for a qubit, is coupled to a noisy environment that causes information loss. Therefore, we need to gain precise knowledge of the noise as a probe for the system dynamics. Higher order spectra extend upon our current noise characterization methods and provide new information on the spectral properties of the system. This has been exploited for quantum systems in recent publications [74, 75].

This chapter will focus on the bispectrum $S_4(\omega_1, \omega_2)$ as it was defined in Eq. (4.5.2). The bispectrum $S_4(\omega_1, \omega_2)$ quantifies the correlation between two spin noise components at different frequencies, ω_1 and ω_2. If the existence of a component of the frequency ω_1 in the spin noise signal increases (decreases) the probability of a component with the frequency ω_2 being present as well, $S_4(\omega_1, \omega_2)$ will be positive (negative). $S_4(\omega_1, \omega_2)$ is zero if spin noise components of these frequencies are not correlated. The main focus of this chapter will be the features of the bispectrum, and where we can expect to find information not provided by the second-order spin noise $C_2(\omega)$. To this end, results from a classical EOM approach as well as the results of fully quantum mechanical ED calculations are presented. Most of the data analyzed here is also part of a publication currently in pre-print [104].

7.1 Fourth-Order Spin Noise in the FOA

This section describes the basic features of $S_4(\omega_1, \omega_2)$ in the central spin model, calculated in the FOA. The fourth-order cumulant $S_4(\omega_1, \omega_2)$ consists of two parts according to its definition Eq. (4.5.2): $C_4(\omega_1, \omega_2)$ and the product $C_2(\omega_1)C_2(\omega_2)$. Both terms are plotted in Fig. 7.1. They can only be equal or greater than zero for all frequencies ω_1 and ω_2.

The behaviour of $C_2(\omega)$ is well known and was succinctly summarized in Sec. 5.4.3. In the absence of a magnetic field the correlator C_2 features a delta-peak at $\omega = 0$, as seen in Fig. 6.2. In the FOA and in the case of homogeneous coupling

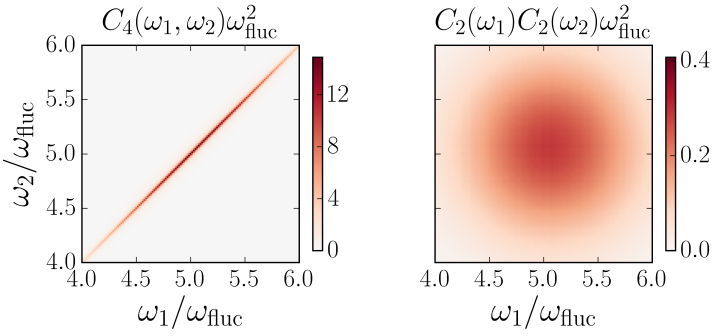

Figure 7.1: $C_4(\omega_1,\omega_2)$ and $C_2(\omega_1)C_2(\omega_2)$ calculated by FOA. The results were averaged over 10^6 randomly generated Overhauser fields. The cumulate S_4 spectrum is shown in Fig. 7.2. The external magnetic field is $b_x = 5$. The peaks were broadened with $\gamma/\omega_{\text{fluc}} = 0.01$.

constants the spectral weight of the $\omega = 0$ peaks is maximal, totaling one third of the total spectral weight of $C_2(\omega)$ [31]. When the magnetic field strength is larger than zero, the position of the Gaussian shifts depending on the external magnetic field and the spectral weight is transferred from the delta-peak to the Gaussian. For higher magnetic fields, $b_x > 1$, the contribution at $(0,0)$ vanishes, and only the Gaussian remains. This is why in Fig. 7.2 the anti-correlation at the axes is prominent for $b_x = 0, 1$ but disappears for higher magnetic fields. For $b_x > 1$ $C_2(\omega)$ can be approximated as a Gaussian with the mean given by $\sqrt{b_x^2 + 1/2}$ [58]. Its variance σ^2 is $\sigma^2 = (\omega_{\text{fluc}}/2)^2$ [31]. ω_1 and ω_2 are independent variables, so $C_2(\omega_1)C_2(\omega_2)$ can be expressed by a multivariate Gaussian, as presented in the right panel of Fig. 7.1. In the left panel of Fig. 7.1 $C_4(\omega_1,\omega_2)$ is plotted. It only contributes on the diagonal $\omega_1 = \omega_2$ for $\omega_{1/2} > 0$. This can be seen immediately when performing an analytic Fourier transformation on Eq. (5.1.16), which yields

$$\begin{aligned} C_4(\omega_1,\omega_2) =& \frac{\pi^2}{8}\big[2n_3^4\delta(\omega_1)\delta(\omega_2) \\ &+ (n_1^2+n_2^2)^2\{\delta(\omega_1+\omega_L)\delta(\omega_2+\omega_L)+\delta(\omega_1-\omega_L)\delta(\omega_1-\omega_L)\} \\ &+ n_3^2(n_1^2+n_2^2)(\delta(\omega_1)\{\delta(\omega_2-\omega_L) \\ &+ \delta(\omega_2+\omega_L)\}+\delta(\omega_2)\{\delta(\omega_1-\omega_L)+\delta(\omega_1+\omega_L)\}] \end{aligned} \tag{7.1.1}$$

for a frozen Overhauser field $\vec{B}_n$, with $\vec{n} = (n_1,n_2,n_3)^T = (\vec{B}_n+\vec{B}_{\text{ext}})/|\vec{B}_n+\vec{B}_{\text{ext}}|$ the normalized total magnetic field and ω_L being the Larmor frequency of the total magnetic field. There are only non-zero contributions on the axes ($\omega_1 = 0$ or $\omega_2 = 0$) or the diagonal $\omega_1 = \omega_2$.

In order to present the data in a plot, the δ-distributions are broadened to a Lorentzian with a width of $\gamma T^* = 0.01$, as described in Eq. (5.2.22). For $b_x > 1$, the spectrum follows a Gaussian distribution centred around $\sqrt{b_x^2 + 1/2}$ with $\sigma = \omega_{\text{fluc}}/2$ in the direction of the diagonal. This agrees with the result of FOA [31], since a high magnetic field suppresses spin flips, leading to an Ising

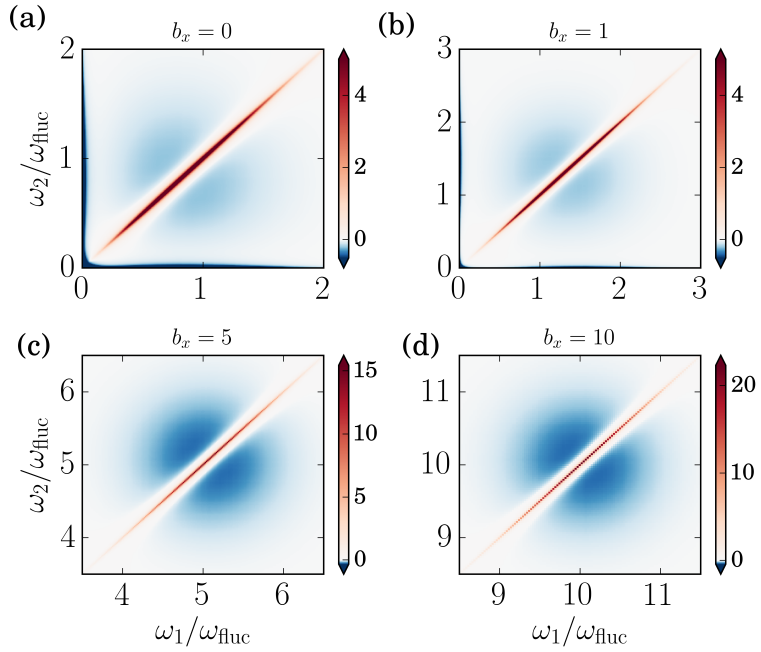

Figure 7.2: $S_4(\omega_1, \omega_2)$ in units of $1/\omega_{\text{fluc}}^2$ computed in the FOA averaged over 10^6 Overhauser fields for a transversal magnetic field of (a) $b_x = 0$, (b) $b_x = 1$ (c) $b_x = 5$ and (d) $b_x = 10$. The peaks were broadened with $\gamma/\omega_{\text{fluc}} = 0.01$.

model. The Gaussian distribution of polarization is due to the central limit theorem, since an infinite bath is assumed.

Combining $C_4(\omega_1, \omega_2)$ and $C_2(\omega)$ to obtain $S_4(\omega_1, \omega_2)$ as defined in Eq. (4.5.1) leads to correlations dominating on the diagonal $\omega_1 = \omega_2$ and anticorrelations elsewhere in the (ω_1, ω_2)-plane. Figure 7.2 depicts the results of the FOA for the fourth-order cumulant for different external magnetic fields. For small magnetic fields ($b_x = 0, 1$) one can also see an anticorrelation contribution at the axes. This is due to $C_2(\omega)$ featuring a distinct peak around $\omega = 0$ for small or absent magnetic fields, and not caused by any fourth-order phenomenon.

7.2 $S_4(\omega_1, \omega_2)$ in the Classical and Quantum Mechanical Regime

In this section the results of $S_4(\omega_1, \omega_2)$ obtained both via the classical EOM and the ED in the quantum mechanical regime are discussed, summarizing Ref. [104]. After the qualitative features of C_4 as well as the product C_2C_2 have been established via the FOA, we compare the results of more sophisticated methods like the quantum mechanical calculation and the classical EOM. This will enable us to gain a deeper understanding of the spectra.

The average ratio between nuclear and electric Zeeman energy amounts to $\zeta \approx 1.25 \times 10^{-3}$ for InAsGa using the gyromagnetic ratios found in Tab. 3.1. The

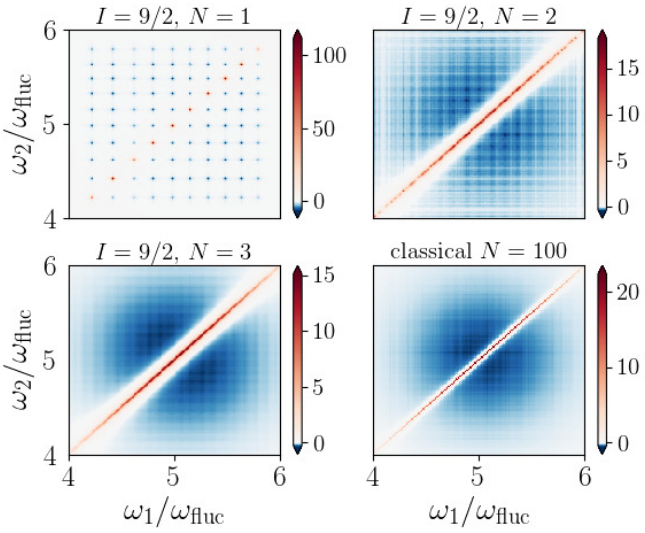

Figure 7.3: $S_4(\omega_1, \omega_2)$ computed for $N = 1, 2, 3$ bath spins with $I = 9/2$, and for $N = 100$ classical spins. The transversal magnetic field is $b_x = 5$, $\zeta = 1.25 \times 10^{-3}$, and quadrupolar interaction is not included. This plot has been taken from Ref. [104].

Zeeman energy ratio depends, however, on the ratio of isotopes. We will assume that all nuclear spins have the same average Zeeman factor instead of identifying the different isotopes in our model.

Figure 7.3 shows results from both methods, the ED for $I = 9/2$ nuclear spins (for example Indium) and $N = 1, 2, 3$, and the classical results for $N = 100$. For $N = 1$, the distance between the positions of the non-zero contributions are given by the Zeeman splitting of the nuclear spins. Therefore, we see in $(2I + 1)^2$ equidistant peaks on a grid around the point given by (ω_L, ω_L). The peaks are positive at the $\omega_1 = \omega_2$ diagonal and negative everywhere else. Increasing the bath size leads the spectrum to become more continuous. At $N = 3$ bath spins of length $I = 9/2$ the S_4 spectrum, as displayed in the lower left panel of Fig. 7.3, is already qualitatively congruent to the classical result depicted on the lower right panel of Fig. 7.3. The classical result is very similar to the FOA result given in Fig. 7.2 (c). This shows that the FOA is very well suited to explain the basic features of the spectrum. Additionally, Fig. 7.3 proves that the classical approach yields good results even for small baths as long as the nuclear spin length is relatively large.

Figure 7.4 depicts the quantum mechanical results for $S_4(\omega_1, \omega_2)$ calculated for different spin lengths ($I = 3/2,\ 5/2,\ 7/2$). The bath size is fixed and an external magnetic field $b_x = 5$ is applied. Due to the exponential increase in the Hilbert space dimension and the larger number of non-degenerate eigenenergies, the spectra become more continuous with increasing nuclear spin length I. Positive correlations are again restricted to the frequency subspace $\omega_1 = \omega_2$, while the negative anti-correlations can be found in an area centered around $\omega_1 = \omega_2 \approx b_x$. Note the similarity between the classical results (Fig. 7.3, lower right panel) and

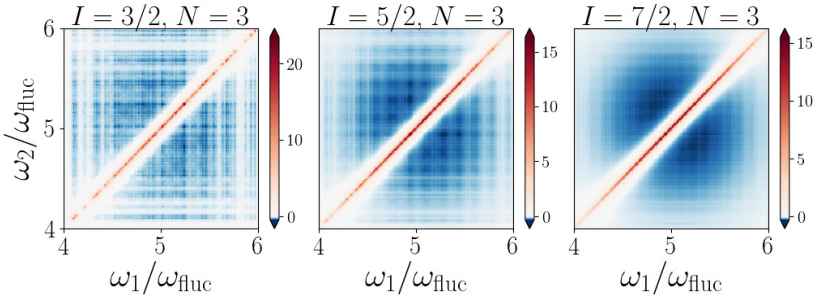

Figure 7.4: $S_4(\omega_1, \omega_2)$ computed via ED for a bath size of $N = 3$ with spin lengths $I = 3/2$, $I = 5/2$ and $I = 7/2$. The transversal magnetic field is set to $b_x = 5$, and quadrupolar interaction is switched off. This plot is taken from Ref. [104].

the quantum mechanical solution for $N = 3$ and $I = 7/2$ (Fig. 7.4, right panel). This solidifies the assumption that the quantum mechanical spectra approach the classical results in the limit of $I \to \infty$.

In order to further study the spectra, the diagonal cut $\omega_1 = \omega_2$ is parametrized as

$$A^{\text{diag}}(\tilde{\omega}) = A(\tilde{\omega}/\sqrt{2}, \tilde{\omega}/\sqrt{2}). \tag{7.2.1}$$

The function $A(\omega_1, \omega_2)$ can be $S_4(\omega_1, \omega_2)$, $C4(\omega_1, \omega_2)$ or $C_2(\omega_1)C_2(\omega_2)$. $S_4^{\text{diag}}(\tilde{\omega})$ is plotted in Fig. 7.5 in the lower right panel. The definition is used analogously for the diagonal cuts through the $C_2(\omega_1)C_2(\omega_2)$ and $C_4(\omega_1, \omega_2)$ spectra. The spectrum changes slightly when the applied magnetic field is small, here $b_x = 1$. This can be seen in Fig. 7.5, and is also the case in the FOA, see Fig. 7.2.

$S_4^{\text{diag}}(\tilde{\omega})$ for high magnetic fields is plotted in Fig. 7.6. While the quantum mechanical spectra has a Gaussian envelope centred around $\sqrt{b_x^2 + 1/2}$ for all magnetic fields, it develops a comb of peaks for very high magnetic fields, $b_x > 50$. This is due to the spin flip suppression at larger fields, which causes the system to become Ising-like. The location of the peaks is governed by the hyperfine interaction. The distance between the peaks decreases with an increasing number of nuclei spins, $\propto 1/\sqrt{N}$. This behaviour is not exhibited by the classical approach, since the larger spin bath causes a continuous shape. At a larger bath size the quantum mechanical results would again approach the classical simulation.

The results presented in this section prove that the classical calculations are valid limits of the quantum mechanical calculations for $I \to \infty$ and $N \to \infty$. The non-zero fourth-order cumulant shows that the central spin is not a random variable with purely Gaussian noise. Both numerical methods, classical and quantum mechanical, share the same restriction of C_4 to the diagonal $\omega_1 = \omega_2$ as the FOA. The features of the spectra in the CSM are driven by both the precession in the external magnetic field as well as the interaction with the nuclear spins.

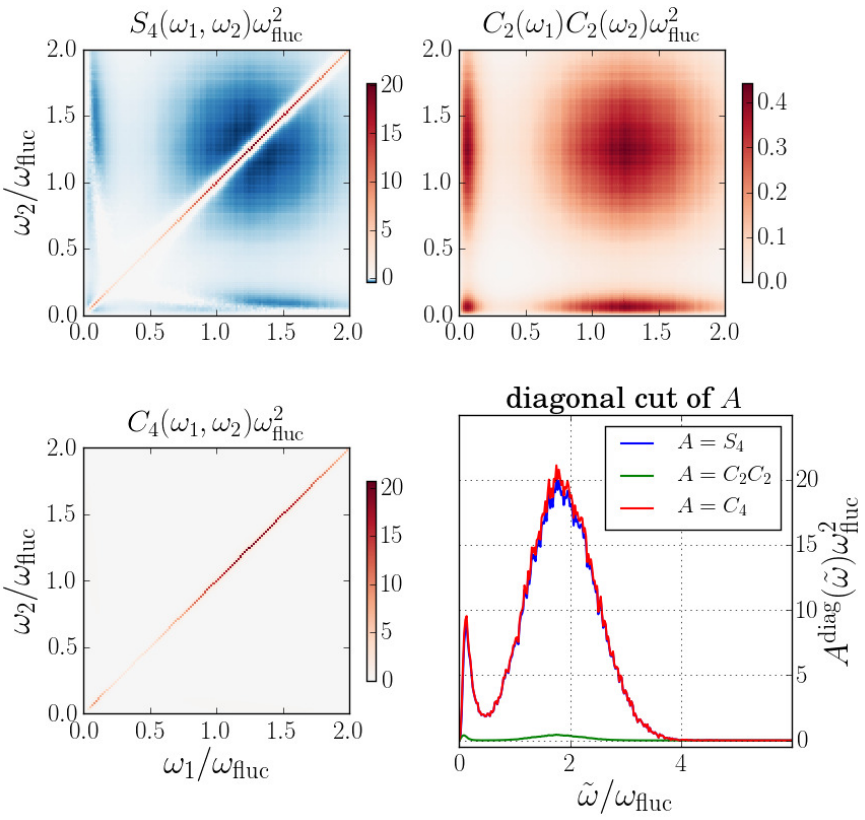

Figure 7.5: $S_4(\omega_1, \omega_2)$ as well as $C_4(\omega_1, \omega_2)$ and $C_2(\omega_1)C_2(\omega_2)$ for $b_{\text{ext}}^x = 1$ in the classical simulation with $N = 100$ bath spins. In the lower right panel the diagonal cut through all three spectra is shown. This plot has been previously published in Ref. [104].

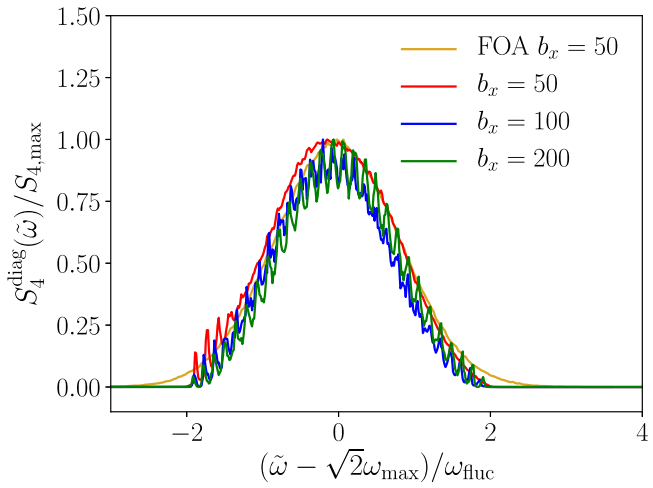

Figure 7.6: $S_4^{\text{diag}}(\tilde{\omega})$ for high ($b_x = 50, 100, 200$) transversal magnetic fields. Computed via the quantum mechanical scheme for $N = 3$ bath spins with a spin length of $I = 9/2$. The spectra are shifted by $\sqrt{2}\omega_{\text{max}} = \sqrt{2}\sqrt{b_x^2 + 1/2}$. The frozen Overhauser field approximation (FOA) is included for comparison. This plot has been previously published in Ref. [104].

7.3 Influence of Quadrupolar Interaction on S_4

Since the quadrupolar interaction changes the nuclear spin dynamics as well as the electron spin dynamics substantively, we will investigate its effect on the fourth-order spin noise in this section. The influence of quadrupolar coupling is evident in the second-order correlation function $C_2(t)$ only for $b_x \to 0$. The results of $S_4(\omega_1, \omega_2)$ in the FOA, the classical EOM and the quantum mechanical results for large bath sizes are all very similar without a quadrupolar term. Since the classical EOM approach presented in Ref. [104] only simulates isotropic quadrupolar coupling, the anisotropy factor is set to $\eta = 0$ in all calculations in this section. This enables a valid comparison between classical and quantum mechanical approaches.

As discussed in the previous two sections, the positive correlations of $S_4(\omega_1, \omega_2)$ are restricted to the diagonal $\omega_1 = \omega_2$, due to the spectral confinement of $C_4(\omega_1, \omega_2)$. Everywhere else in the plane, the correlation is either negative or zero, depending on the product $C_2(\omega_1, \omega_2)$. This investigation focuses on medium and large magnetic field strengths, since the second-order spin correlation $C_2(t)$ and the spin noise power spectrum $C_2(\omega)$ contain no information on the quadrupolar coupling on the spin dynamics in this regime. For $b_x > 1$, the spin noise power spectrum is in leading order a Gaussian [31, 38] centered around $\omega = \sqrt{b_x^2 + 1}$.

Figure 7.7 depicts $S_4(\omega_1, \omega_2)$ computed fully quantum mechanically by ED for nuclear spin lengths $I = 3/2,\ 7/2,\ 9/2$ as well as the results of the classical approach. The strength of the quadrupolar coupling Q_r is chosen in a way that $C_2(t)$ agrees for $b_{\text{ext}} = 0$ independent of the spin length. This was done according to the results shown in Fig. 6.6.

Without quadrupolar interaction, the fourth-order contribution to S_4 is restricted to the diagonal, $\omega_1 = \omega_2$. The introduction of quadrupolar coupling broadens the peak that is sharp for $Q_r = 0$. While the quantum mechanical spectra all feature roughly the same influence of the quadrupolar interaction, the broadening of the classical spectrum is smaller, causing the spectrum to exhibit a sharper peak. Since the quadrupolar coupling strengths were explicitly chosen so that the second-order correlation would show the same dynamics irrespective of spin length or method, this mismatch is related to the fourth-order correlation C_4.

The results shown in Fig. 7.7 were all computed for $b_x = 5$. At such a relatively large magnetic field strength, a second-order correlation is not changed by the introduction of quadrupolar coupling. However, the broadening featured in S_4 caused by quadrupolar interaction is quite strong. Therefore, it is proven that fourth-order correlation does indeed carry additional information compared to C_2.

In order to further analyze the broadening of the correlation due to quadrupolar coupling, we parametrize the anti-diagonal cut in the vicinity of the gloabal

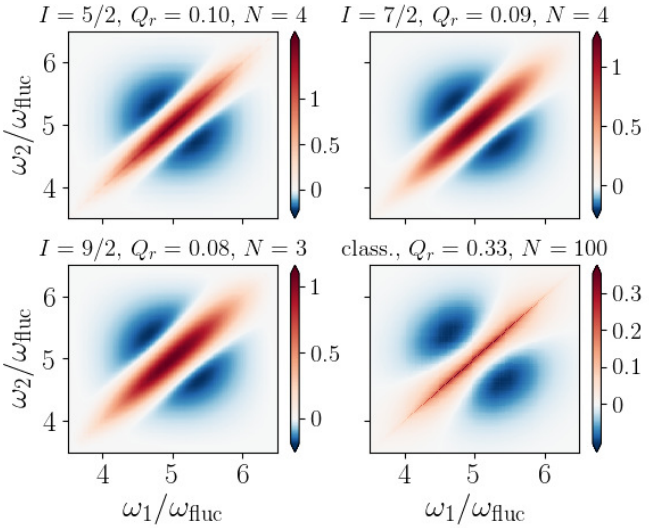

Figure 7.7: $S_4/\omega_1, \omega_2)$ with a magnetic field $b^x_{\text{ext}} = 5$, with different spin lengths I, bath sizes N and interaction strengths Q_r. The parameters are chosen for similar behavior in the second-order spin correlation, see right panel of Fig. 6.6. This plot has previously been published in Ref. [104].

maximum $S_4(\omega_{\max}, \omega_{\max})$, with $\omega_{\max}/\omega_{\text{fluc}} = \sqrt{b_x^2 + 1/2}$ by $\omega_1 + \omega_2 = 2\omega_{\max}$. It is expressed by

$$S_4^{\text{adiag}}(\tilde{\omega}) = S_4\left(\omega_{\max} + \frac{\tilde{\omega}}{\sqrt{2}}, \omega_{\max} - \frac{\tilde{\omega}}{\sqrt{2}}\right). \tag{7.3.1}$$

The global maximum is then located at the relative frequency $\tilde{\omega} = 0$.

Figure 7.8 (a) shows the the diagonal and panel (b) the anti-diagonal cuts of the data presented in Fig. 7.7. While the same parameters led to congruent results for the second-order spin correlation, as seen in Fig. 6.6 (b), they cause quite different behaviour in S_4. In Fig. 7.8 (a) the diagonal cuts computed with the quantum mechanical method for different nuclear spin length I and number of nuclear spins N are plotted, as well as the results of the classical approach for a bath size $N = 100$. The Gaussian curve progression for the diagonal cuts remains qualitatively the same, but with increasing spin length (and decreasing Q_r) the amplitude decreases markedly. The classically computed spectrum is an outlier and shows the lowest global maximum. This is directly linked to the broadening, since the total spectral weight of C_4 is conserved.

Figure 7.8 (b) presents the anti-diagonal cuts for the same parameters as Fig. 7.8 (a) and Fig. 6.6 (b). For comparison $S_4^{\text{adiag}}(\tilde{\omega})$ for $Q_r = 0$ is depicted as well. $S_4^{\text{adiag}}(\tilde{\omega})$ has a qualitatively different curve shape depending on the computational approach. While the classical curve exhibits a sharp peak, the results obtained by the quantum mechanical approach show a Gaussian shape.

One can conclude that the scaling behaviour which allows matching the classical and quantum mechanical results by adjusting Q_r is only present for the

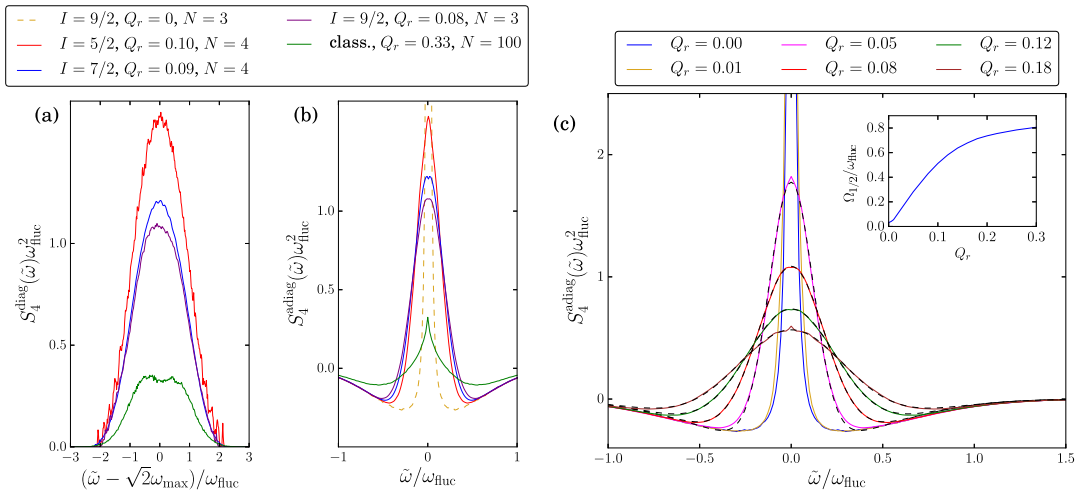

Figure 7.8: Panel (a): The same data plotted in Fig. 7.7, cut in the diagonal $\omega_1 = \omega_2$, $S_4^{\mathrm{diag}}(\tilde{\omega})$. Panel (b): The anti-diagonal cut $\omega_1 + \omega_2 = 2\omega_{\mathrm{max}}$, $S_4^{\mathrm{adiag}}(\tilde{\omega})$. $S_4^{\mathrm{diag}}(\tilde{\omega})$ without quadrupolar coupling was added in the middle panel as a yellow dotted line for comparison. Panel (c): $S_4^{\mathrm{adiag}}(\tilde{\omega})$ quantum mechanically calculated with $N = 3$, $b_x = 5$ and $I = 9/2$ for different Q_r. The inset plot shows the full width half maximum $\Omega_{1/2}$ of C_4 in relation to the quadrupolar coupling strength Q_r. All plots have been published previously in Ref. [104]

second-order correlation at $b_x = 0$. It is possible that the fourth-order bispectrum S_4 has features that have been neglected in the classical approach, such as the non-commutability of the spin operators. Also, C_4 could react more strongly than C_2 to the quadrupolar coupling q_k of an individual bath spin I_k. At constant Q_r, the individual coupling constants will be bigger in a small bath than in a large bath. Since the classical EOM approach can simulate more nuclear spins, and in fact only yields satisfactory results for large bath sizes, the individual q_k are much smaller than in the small baths computed by ED.

In order to investigate the connection between the strengths of the quadrupolar couplings and the broadening of the anti-diagonal cut, $S_4^{\mathrm{adiag}}(\tilde{\omega})$ is presented for $N = 3$ and $I = 9/2$ for different Q_r in Fig. 7.8 (c). The contribution of $C_2(\omega_1)C_2(\omega_2)$ on the spectrum is Gaussian with a variance $\sigma^2 = (\omega_{\mathrm{fluc}}/2)^2$. In the applied magnetic field, the second-order contribution is wholly independent of the quadrupolar coupling, and is equivalent to the FOA result [31]. The fourth-order contribution on the bispectrum, however, changes noticeably with the quadrupolar coupling strength. We obtain the full-width half maximum $\Omega_{1/2}$ by fitting only C_4 with a Gaussian. The relation between $\Omega_{1/2}$ is shown in the inset of in Fig. 7.8 (c). In the regime of small Q_r, $\Omega_{1/2}$ increases with Q_r in a roughly linear fashion, before the increase flattens for $Q_r > 0.1$. In the limit of small quadrupolar coupling $Q_r \to 0$ the Gaussian curve becomes a sharp peak, with $\Omega_{1/2} \to 0$ only non-zero due to the finite Lorentz broadening.

Figure 7.9 shows the anti-diagonal cut $S_4^{\mathrm{adiag}}(\tilde{\omega})$ for different magnetic fields

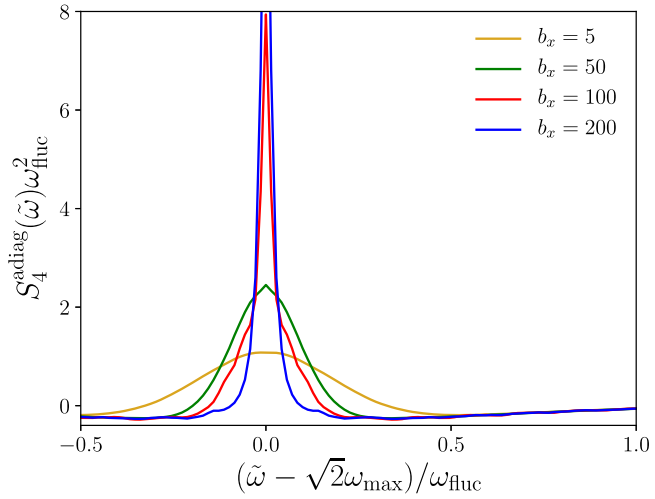

Figure 7.9: $S_4^{\mathrm{adiag}}(\tilde{\omega})$ quantum mechanically calculated with $N = 3$, $Q_r = 0.08$ and $I = 9/2$ for different transversally applied external magnetic fields b_x. This plot has been published before in Ref. [104].

b_x and a bath size $N = 3$ and nuclear spin length $I = 9/2$. The broadening induced by a quadrupolar coupling decreases when the external magnetic field is increased. For larger magnetic fields, the dynamics of the system becomes dominated by the Zeeman energy, with H_Q becoming increasingly perturbatory in comparison. Similar behaviour has also been observed in the fourth-order spin correlation in the time domain, where a large magnetic field drastically changes the long-time decay [29, 53, 72]. This will be explored further in the following chapter on fourth-order correlation in real time.

Lastly, we investigate the crossover regime, where the Zeeman energy is of the same magnitude as ω_{fluc}. For $b_x \approx 1$, the electron spin dynamic is dominated by both the fluctuating Overhauser field and the external magnetic field, as they have equal strength. Since the nuclear Zeeman energy is smaller than the electric Zeeman energy by the factor $\zeta = 0.00125$, the nuclei spin dynamics is mostly not influenced by the external magnetic field. The nuclear spin dynamic is only governed by the quadrupolar coupling and the hyperfine coupling with the electron spin.

In Fig. 7.10, two extreme cases are compared in the crossover regime $b_x = 1$. The left panel of Fig. 7.10 shows S_4 for the smallest possible bath size $N = 1$, while the right panel presents a classical calculation of $N = 100$ bath spins. While $N = 1$ is far away from a classical limit and requires quantum mechanical calculation, $N = 100$ is far removed from the capabilities of the quantum mechanical method and is thus computed classically. Note that the quantum mechanical S_4 on the left is the result of computation in the limit of weak measurement for $N = 1$. However, it is near identical to the S_4 presented for strong and continuous measurement in Ref. [76]. This shows that measurement strength does not have

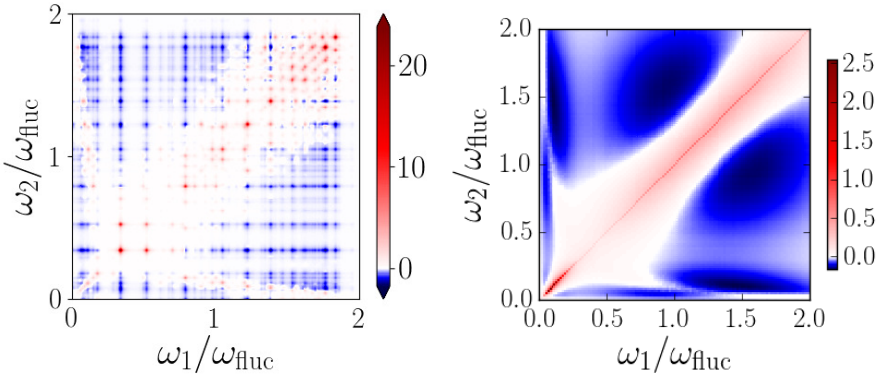

Figure 7.10: S_4 for a smaller magnetic field of $b_x = 1$. Left: obtained by quantum mechanical calculation, with $N = 1$, $I = 9/2$ and $Q_r = 0.08$. Right: the classically computed spectrum with $N = 100$, $Q_r = 0.33$. This plot has been previously published in Ref. [104].

a significant influence on S_4 in the CSM. For $b_x = 1$, the quadrupolar term does not only influence C_4, but also alters the second-order contribution C_2. S_4 exhibits alternating correlation and anti-correlation in the (ω_1, ω_2)-plane for small ω_1 or ω_2. For a fixed ratio $\omega_1/\omega_{\text{fluc}} = 1$, increasing ω_2 shows first weak anti-correlation, then correlations, and then anti-correlations again. Here, the positive correlations are not confined to the diagonal as depicted in Fig. 7.5 and Fig. 7.2, but are spread due to the presence of the quadrupolar couplings. The classically computed S_4 shown in the right panel exhibits a continuous spectrum, but with similar features. These are the anti-correlation at the axis with a local maximum along $\omega_{1/2}/\omega_{\text{fluc}} = 1$, with the broadening of the correlation along the diagonal.

7.4 Chapter Conclusion

In this chapter, the fourth-order spin noise bispectrum $S_4(\omega_1, \omega_2)$ was investigated. The bispectrum quantifies the correlation between a spin noise component with the frequency ω_2 and a spin noise component with the frequency ω_2. $S_4(\omega_1, \omega_2)$ is a cumulant, which means that all Gaussian noise is subtracted.

The basic features of the bispectrum can be explained in the FOA, such as the positive correlation being limited to the $\omega_1 = \omega_2$ diagonal and the anticorrelation having the shape of an bivariate Gaussian around $\omega_1 = \omega_2 = \omega_L$ in the case of $b_x > 1$. The bispectrum was computed both classically and quantum mechanically, which is presented in Sec. 7.2. Both methods agree remarkably well in the limits of a large spin bath and long nuclear spins. This is because for increased N or I, the number of eigenstates grows exponentially, causing the energy spectrum to become more similar to the continuous classical energy spectrum.

Sec. 7.3 deals with the fourth-order spin noise in the extended CSM with added quadrupolar coupling. Introducing quadrupolar interaction causes a broadening of the positive contribution to the fourth-order cumulant. The classical and the quantum mechanical method both yield congruent results in the case of second-order correlation with or without quadrupolar coupling, and in the case of fourth-order correlation without quadrupolar coupling. Here, however, classical and quantum mechanical results differ slightly the broadening caused by quadrupolar interaction. While second-order correlation is not influenced by quadrupolar coupling when an external magnetic field is applied, S_4 does so significantly. This proves that fourth-order correlation does yield information beyond second-order correlation.

Moreover, the results for S_4 obtained through the quantum mechanical method in the weak measurement limit with $N = 1$ are basically identical to the S_4 presented for strong, continuous measurement in Ref. [76]. This implies that the strength of the measurement does not have a significant effect on S_4.

In conclusion, fourth-order spin noise offers new information about the spin correlation in a QD system, and is thus well-worth investigating in experiment. It can be used to describe the influence nuclear quadrupolar coupling has on the spin when an external magnetic field is present.

Chapter 8

Fourth-Order Correlation in Real Time

While fourth-order spin noise, such as the bispectrum presented in the last chapter, has not yet been investigated in experiments at the time of publication of this thesis, fourth-order spin correlations in real time have. Two of these experiments, both measuring different kinds of fourth-order spin correlation functions, will be analyzed in this chapter [29, 72]. The central focus of this chapter is to demonstrate the importance of the nuclear electric quadrupolar interaction for understanding the long-time dynamics of these quantities. This chapter summarizes and expands upon the findings published in Ref. [107].

8.1 Three-Pulse Measurement

This section is about an experiment [72] measuring spin correlation in a single negatively charged GaInAs QD. Three σ^+ pulses were applied to an initially empty QD, the first exciting a $|\downarrow\rangle$-spin electron. After the pulse sequence, the charge of the QD is measured. As will be explained in the following, the probability function of finding one electron (and not two) in the QD, depending on the delay times between the three pulses, contains the fourth-order auto-correlation of the S_z component of the electron spin.

8.1.1 Experimental Realization

One way to measure correlation beyond second-order was explored by Bechtold et al. [72]. The system is a single QD with an asymmetric tunnel barrier and applied voltage, as sketched in Fig. 8.1. The experiment measured the probability of the central electron spin being in the spin-$|\downarrow\rangle$ state at times t_1 and $t_1 + t_2$, when the electron was initially transferred into the spin-$|\downarrow\rangle$ at $t = 0$.

An asymmetric tunnel barrier extends the lifetime of excited electrons up to several microseconds, while the lifetime of the holes is unaffected. At time $t = 0$, the empty QD is pumped with a σ^+-pulse that excites a neutral exciton state ($|\downarrow\Uparrow\rangle$). The hole then escapes the QD within picoseconds, which leaves the spin-$|\downarrow\rangle$ state ($|\downarrow\Uparrow\rangle \rightarrow |\downarrow\rangle$). After a delay time t_1, another σ^+-pulse is applied. The measurement of polarization follows as described in Sec. 2.3.2. If the electron spin has flipped during that time and is in the spin-$|\uparrow\rangle$ state, the QD is then charged with two electrons ($|\uparrow\downarrow\Uparrow\rangle \rightarrow |\uparrow\downarrow\rangle$) and becomes optically inactive. If the electron is in the spin-$|\downarrow\rangle$ state, the pulse has no effect, since the Pauli principle does not allow the creation of another $|\downarrow\rangle$-electron. We model the effect of this pulse as the projection operator $P_\downarrow = |\downarrow\rangle\langle\downarrow|$. The same σ^+-pulse is again applied at $t = t_1 + t_2$. After this, the total charge is measured. If the electron spin was in a spin-$|\downarrow\rangle$ state both at times t_1 and $t_1 + t_2$, the QD is charged with $1e$. If the electron spin was in the spin-$|\uparrow\rangle$ state at any time of measurement, the QD is doubly negatively charged. This measurement is then repeated often enough to gain a statistically significant probability of a singly charged QD at the end of these three pulses.

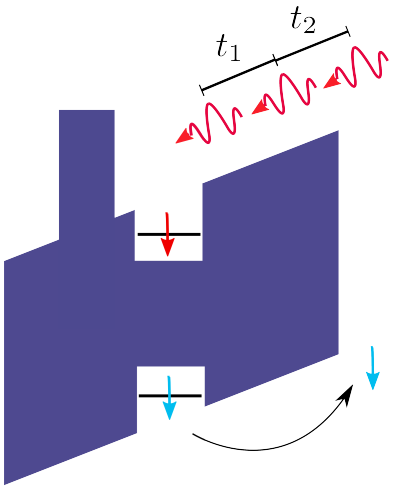

Figure 8.1: The QD system with applied voltage and an asymmetric tunnel barrier to allow for hole tunneling while the electron excited to the conduction band stays localized. Three σ^+ laser pulses are applied; one for initialising the spin, the second and third one at times t_1 and $t_1 + t_2$ [72].

The first probe pulse at time t_1 transfers the density operator from ρ_{init} to

$$\rho(t_1) = \frac{1}{w_1(t_1)} P_\downarrow U(t_1)\rho_{\text{init}}U^\dagger(t_1)P_\downarrow^\dagger. \tag{8.1.1}$$

$U(t) = \exp(-\mathrm{i}Ht)$ is the time evolution operator and

$$w(t_1) = \langle P_\downarrow(t_1)\rangle_{\text{init}} \tag{8.1.2}$$

is the probability to measure the electron spin $|\downarrow\rangle$ state at time t_1 (before the probe pulse). Since we are in the high temperature limit, and the pump pulse at $t = 0$ has generated an electron in the spin-$|\downarrow\rangle$ state, the initial density operator at $t = 0$ is $\rho_{\text{init}} = 2P_\downarrow(0)/D$. D is the dimension of the Hilbert space. We use the notation $\langle\hat{O}\rangle_{\text{init}} = \text{Tr}(\hat{O}\rho_{\text{init}})$ where $\hat{O}$ is an arbitrary operator, and the relation $P_\downarrow = P_\downarrow^\dagger = P_\downarrow^2$. The conditional probability of the electron being in the spin-$|\downarrow\rangle$ state again at time $t_1 + t_2$ can be written as

$$w(t_1|t_2) = \text{Tr}\left(P_\downarrow U(t_2)\rho(t_1)U^\dagger(t_2)P_\downarrow^\dagger\right). \tag{8.1.3}$$

The joint probability function for measuring spin-$|\downarrow\rangle$ at both times results in

$$\begin{aligned} w(t_1,t_2) &= w(t_1|t_2)w(t_1) \\ &= \mathrm{Tr}\left(P_\downarrow U(t_2)P_\downarrow U(t_1)\rho_{\mathrm{init}}U^\dagger(t_1)P_\downarrow^\dagger U^\dagger(t_2)P_\downarrow^\dagger\right) \\ &= \langle P_\downarrow^\dagger(t_1)P_\downarrow^\dagger(t_1+t_2)P_\downarrow(t_1)\rangle_{\mathrm{init}} \\ &= \frac{2}{D}\mathrm{Tr}\left(P_\downarrow(t_1)P_\downarrow(t_1+t_2)P_\downarrow(t_1)P_\downarrow(0)\right). \end{aligned} \tag{8.1.4}$$

This is a special case of a general fourth-order autocorrelation function defined as

$$G_4(t_1,t_2,t_3) \;=\; \frac{2}{D}\mathrm{Tr}\left(P_\downarrow(t_1)P_\downarrow(t_2)P_\downarrow(t_3)P_\downarrow(0)\right) \tag{8.1.5}$$

such that $w(t_1,t_2) = G_4(t_1,t_1+t_2,t_1)$. Using the identity $P_\downarrow = \mathbb{1}/2 - S_z$ results in

$$G_4(t_1,t_1+t_2,t_1) = \frac{1}{4} + C_2(t_1) + C_2(t_2) + \frac{1}{2}C_2(t_1+t_2) + 2C_4(t_1,t_1+t_2,t_1) \tag{8.1.6}$$

with second-order spin autocorrelation functions

$$C_2(t) = \langle S_z(t)S_z\rangle \tag{8.1.7}$$

and the general fourth-order autocorrelation function of the electron spin

$$C_4(t_1,t_2,t_3) = \langle S_z(t_1)S_z(t_2)S_z(t_3)S_z\rangle\,. \tag{8.1.8}$$

All expectation values are calculated with respect to the high-temperature density operator $\rho_{\mathrm{ht}} = \mathbb{1}/D$.

8.1.2 G_4 in the CSM: FOA and ED Results

The fourth-order autocorrelation of the projection operator $P_\downarrow$ as calculated in the FOA follows from Eq. (5.1.13) and Eq. (5.1.16),

$$\begin{aligned} G_4(t_1,t_1+t_2,t_1) =& \frac{1}{4} + 2C_4(t_1,t_1+t_2,t_1) + C_2(t_1) + C_2(t_2) + \frac{1}{2}C_2(t_1+t_2) \\ =& \frac{1}{4}\{(n_3^2+1)^2 + (n_1^2+n_2^2)^2\cos(\omega_{\mathrm{L}}t_1)\cos(\omega_{\mathrm{L}}t_2) \\ &+ (n_1^2+n_2^2)(n_3^2+1)[\cos(\omega_{\mathrm{L}}t_1)+\cos(\omega_{\mathrm{L}}t_2)]\}. \end{aligned} \tag{8.1.9}$$

For a large transversally applied magnetic field ($\vec{n} \approx \vec{e}_x$) we can neglect the $C_2(t)$ contributions, since they decay to zero after $t \approx 10T^*$, as demonstrated in Fig. 5.1. We obtain

$$\begin{aligned} G_4(t_1,t_1+t_2,t_1) =& \frac{1}{4} + 2C_4(t_1,t_1+t_2,t_1) \\ =& \frac{1}{4} + \frac{1}{8}\cos(\omega_L(t_1-t_2)) \end{aligned} \tag{8.1.10}$$

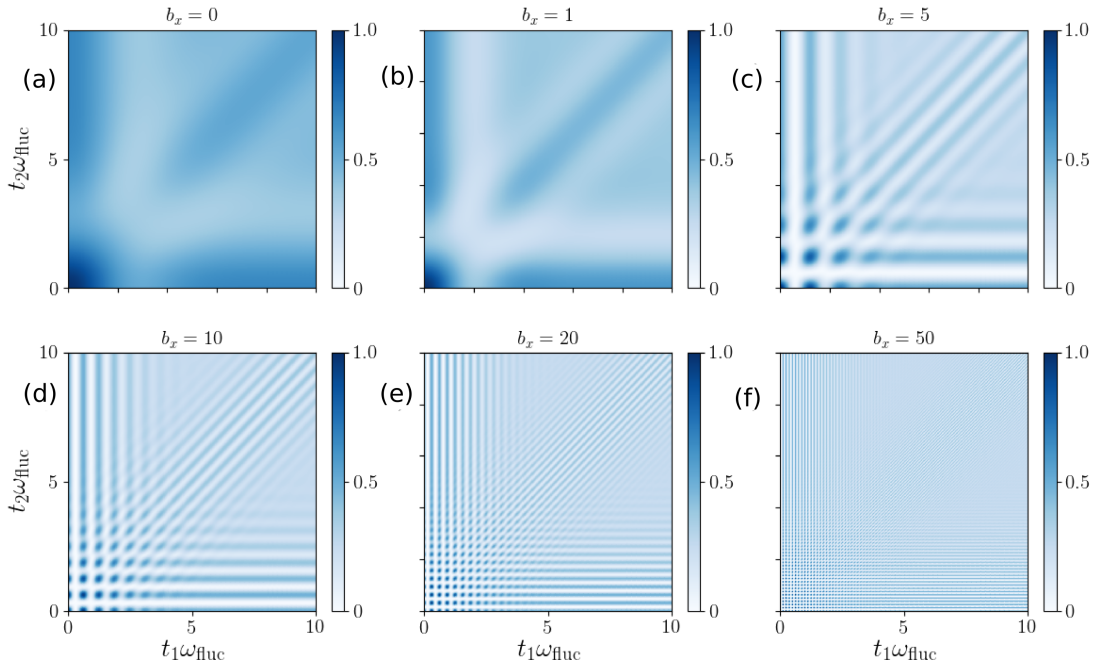

Figure 8.2: $G_4(t_1, t_1 + t_2, t_1)$ computed in the FOA for different magnetic fields, (a) $b_x = 0$, (b) $b_x = 1$, (c) $b_x = 5$, (d) $b_x = 10$, (e) $b_x = 20$, (f) $b_x = 50$. It was obtained through averaging over $M = 10^6$ random Overhauser fields.

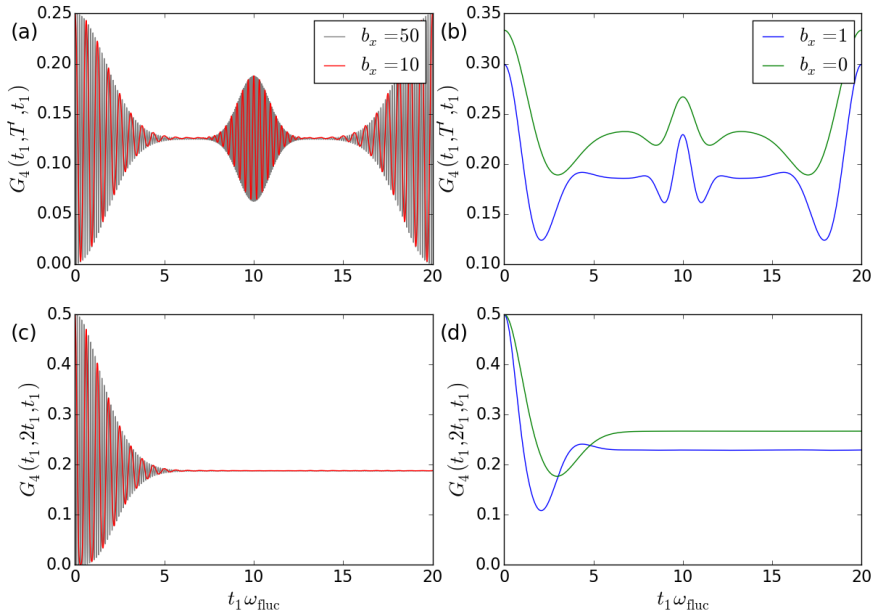

Figure 8.3: Cuts through $G_4(t_1, t_1 + t_2, t_1)$ computed in the FOA. (a) and (b) show the transversal cut $t_1 + t_2 = 20T^*$, while (c) and (d) show the longitudinal cut $t_1 = t_2$. The magnetic field strengths are $b_x = 10, 50$ in (a) and (c), and $b_x = 0, 1$ in (b) and (d).

for $t_1, t_2 \gg T^*$ with Eqs. (5.1.16) and (8.1.9). For equal delay times, $t_1 = t_2 = t$, $G_4(t, 2t, t) = 3/8$ for long-time scales. If the sum of the delay times (the time of the second probe pulse) is held constant ($t_1 + t_2 = T'$) we observe an oscillation with $2\omega_\mathrm{L}$, double the Lamor frequency for the fourth-order function

$$G_4(t_1, T', t_1) = \frac{1}{4} + \frac{1}{8}\cos(\omega_\mathrm{L}(2t_1 - T')). \tag{8.1.11}$$

This explains the oscillation with $2\omega_\mathrm{fluc}$ at around $t_1 = T'/2$ that was observed in experiment [72] for high magnetic fields if the time between the initialization and the second pulse is kept a constant T'.

Fig. 8.2 shows $G_4(t_1, t_1 + t_2, t_1)$ averaged over 10^6 Gaussian distributed Overhauser fields for different magnetic field strengths. The color represents the magnitude of the correlation function in the two-dimensional color plot. The oscillations present in $G_4(t_1, t_1 + t_2, t_1)$ are parallel to the axes ($t_1 = 0$ or $t_2 = 0$) and the diagonal $t_1 = t_2$. The contributions along the axes clearly stem from second-order correlation: If either one of the two delay times is zero, the pulse sequence only consists of two pulses, resulting in a second-order correlation measurement. The magnetic field strength causes oscillation with the Larmor frequency, both along the axes and along the diagonal. In the following, we will focus on two subspaces in the (t_1, t_2)-plane: The diagonal defined by $t_1 = t_2$ and the anti-diagonal for a fixed $T' = t_1 + t_2$. In Ref. [72], the measurements were performed for (t_1, t_2) pairs along these lines.

In Fig. 8.3 (a), the cut along the anti-diagonal direction, keeping $t_1 + t_2 = 20T^*$ for $G_4(t, T' = 20T^*, t)$ obtained by FOA is depicted for $b_x = 10, 50$. For $t \approx 0$ and $t \approx T'$, oscillations $G_4(t, T' = 20T^*, t) = 1/4$ around with the Larmor frequency with a Gaussian envelope function can be seen. The maximal value the correlation reaches is $1/2$, and the global maxima of G_4 are located at $t = 0$ and $t = T'$. The local maximum at $t = T'/2$ and has a value of $3/8$. Figure 8.3 (b) shows the same cut but for small and absent magnetic field, $b_x = 0, 1$. Here, the correlation function reaches higher maxima, since the second-order contribution does not decay for longer times. Fig. 8.3 (c) shows the diagonal cut of G_4 for the same parameters as (a). The correlation shows an oscillation with the Larmor frequency, that quickly decays for $t > 5T^*$ to stay at a constant level of $3/8$. The diagonal cut $G_4(t, 2t, t)$ plotted in Fig. 8.3 (c) is the local maximum of $G_4(t, T', t)$ at $t = T'/2$ as seen in Fig. 8.3 (a). The diagonal cut gives the maximal amplitude of the oscillation around $t = T'/2$. Why the long-time limit decays to exactly $3/8$ for large magnetic fields can be explained by assuming equal delay times in Eq. (8.1.11). The oscillation centred around $t = T'/2$ originates solely from the fourth-order spin correlation contribution to G_4, since the second-order contributions are completely decayed for $t > 5T^*$. In Fig. 8.3 (d) the diagonal cuts of G_4 are plotted for the same magnetic fields as the anti-diagonal cuts of Fig. 8.3 (b). The constant long-time limit is larger than for high magnetic fields, again due to the second-order correlation not decaying.

Fig. 8.4 (a) presents the anti-diagonal cut $G_4(t, T', t)$ for $b_x = 200$ computed via the FOA (grey) and ED with $N = 6$ nuclear spins $I = 3/2$ (black). We

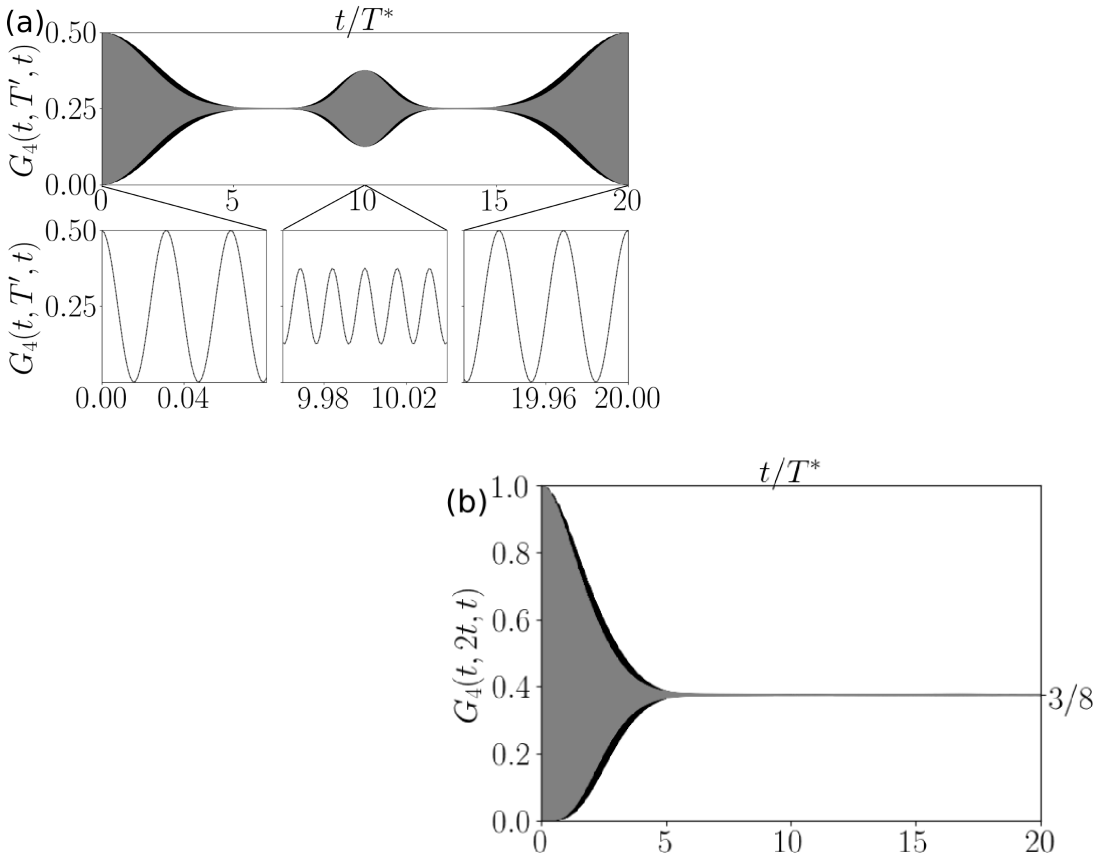

Figure 8.4: Panel (a): $G_4(t, T', t)$ computed in the FOA averaged over 10^6 Overhauser fields (grey) and ED with $N = 6$, $I = 3/2$ nuclear spins (black), both with $b_x = 200$. The lower panels show detailed plots of the oscillation, where ED and FOA results are identical. Panel (b): The diagonal cut of G_4, computed with the same parameters as the data shown in the left panel. Both plots were taken from Ref. [107].

extracted the characteristic time scale as $T^* = 1\,\mathrm{ns}$ by matching the Gaussian envelope of the ED results in Fig. 8.4 (b) to the results of Bechtold et al. [72]. $T^* = 1\,\mathrm{ns}$ is used in all calculations as a reference scale. This also defines the characteristic energy scale of the system, $\omega_{\mathrm{fluc}} = 1/T^* = 1\,\mathrm{GHz}$. Then the dimensionless magnetic field $b_x = 200$ translates to the applied magnetic field strength $B_x = 4.1\mathrm{T}$, which is comparable to $4\,\mathrm{T}$, the highest magnetic field Bechtold et al. applied in the experiment. The lower detailed plots in Fig. 8.4 (a) show the oscillation on a picosecond time scale. At $b_x = 200$, the Larmor frequency is to high for the oscillations to be visible in the main plot. The detailed plots reveal that the results obtained by quantum mechanical ED show the same frequency doubling for the oscillation around $t = T'/2$ as the FOA result does.

Figure 8.4 (b) depicts the diagonal cut $G_4(t, 2t, t)$ calculated with the same parameter as the left panel, again computed via a fully quantum mechanical ED (black) and in the FOA (grey). It exhibits the same features as already observed in Fig. 8.3 (c) for $b_x = 10, 50$.

All in all, the results of the FOA and the fully quantum mechanical ED with a rather small number of $N = 6$ nuclear spins agree remarkably well in a larger external magnetic field, $|\vec{b}_{\mathrm{ext}}| \gg |\vec{b}_N|$. Small finite size effects are responsible for the slight deviation of the ED envelope function compared to the Gaussian of the SCA, which is generated by the central limit theorem requiring $N \to \infty$.

While the results presented so far bring a great deal of clarity to $G_4(t_1, t_1 + t_2, t_1)$, both the results obtained by the FOA and the ED of the CSM Hamiltonian do not show the long-time decay observed in experiment. Apparently, the CSM model is insufficient for accurately describing the long-time dynamics. Bechtold et al. [72] have reported that $G_4(t, 2t, t)$ decays down to $1/4$ for $t \to \infty$ at moderate magnetic fields. They also observed a crossover to an exponential decay with long-time decay time $T_2 \approx 1.4\,\mu\mathrm{s}$. This contradicts our observations of a constant $G_4(t, 2t, t) = 3/8$ for $t > 10T^*$.

8.1.3 Influence of Quadrupolar Coupling on G_4

Quadrupolar coupling is a likely candidate for the interaction causing the decay of $G_4(t, 2t, t)$ down to $1/4$ for longer times, since it has already been proven to be influential for the spin dynamics in QD systems [59]. Since the FOA assumes a static nuclear spin bath, it is not suitable for modeling quadrupolar interaction.

The probes used for the experiments are made of InGaAs. Gallium and Arsenide nuclear spins have a spin length $3/2$, which is the spin length used in the calculations presented here. Indium nuclear spins have a spin length $9/2$, which we will also simulate by $I = 3/2$ in order to access larger bath sizes. The anisotropy of the quadrupolar coupling is set to $\eta = 0.5$ [87].

In order to investigate the influence of the nuclear Zeeman energy and the quadrupolar coupling separately, we first study the system for $\zeta = 0$. A quadrupolar coupling of $Q_r = 0.15$ was used. This value was chosen by comparing

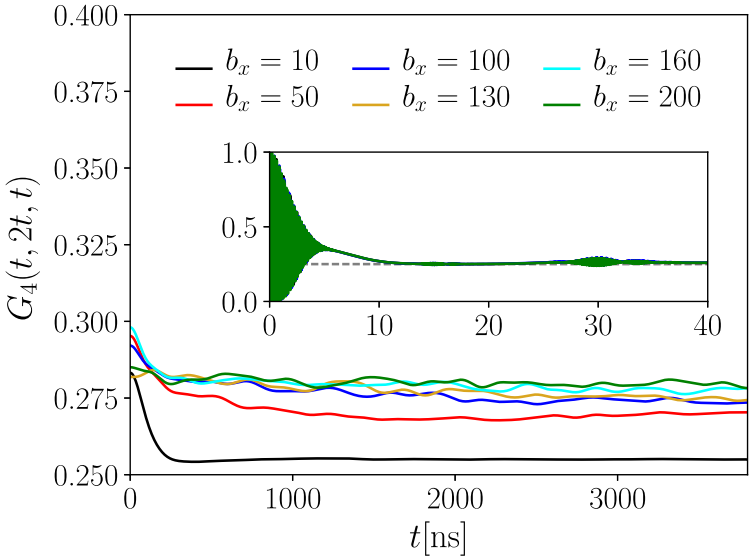

Figure 8.5: $G_4(t, 2t, t)$ as function of t for different external magnetic fields. The curves were smoothed through a low-pass filter to suppress finite size oscillations. The inset reveals the short-time behavior without the low-pass filter. One can see that G_4 decays down to a constant level close to $1/4$ in $\mathcal{O}$(ns), and that the time frame of the decay is not dependent on the applied magnetic field. Parameters: $N = 5$ with $I = \frac{3}{2}$ and $Q_r = 0.15$, $\zeta = 0$. This plot was taken from Ref. [107].

the theoretical results plotted in the left panel of Fig. 6.6 to the direct measurement of the decay of $C_2(t)$ [53]. With this values, $G_4(t, 2t, t)$ rapidly approaches a constant with some finite-size oscillations. This decay occurs one a time scale of about 10 ns, as can be seen in the inset plot of Fig. 8.5. Furthermore, the externally applied magnetic field does not influence the decay significantly, as long as the magnetic field is larger than $b_x = 50$. The results do not show he long-time exponential decay at high magnetic fields reported in the experiment [72]. It does, however, describe the experimental results for smaller magnetic fields (0.5 T) quite well.

For extracting the long-time behavior, the finite size oscillations need to be suppressed. Therefore, we smooth the curves through convolution with a Gaussian function

$$g(t) = \frac{1}{\sqrt{2\pi\sigma^2}} \exp\left(-\frac{t^2}{2\sigma^2}\right). \tag{8.1.12}$$

In Fig. 8.5 and Fig. 8.6, a standard deviation $\sigma = 60$ ns was used for this low-pass filter. This is small enough to not interfere with the curve progression in $\mathcal{O}(\mu s)$.

In order to make a connection to the experiments [72], a suppression of the dephasing caused by quadrupolar coupling has to be introduced. This suppression needs to be a function of the external magnetic field, since the decay shown in experiments is $\mathcal{O}$(ns) for small fields, and $\mathcal{O}(\mu s)$ for large fields. The desired effect

is provided by the nuclear Zeeman term, which dominates the local nuclear spin dynamics at large magnetic fields. When the Zeeman energy is in the order of magnitude of the hyperfine interaction energy, the Zeeman splitting of the nuclei suppresses nuclear spin flips.

The average ratio between nuclear and electric Zeeman energy in InGaAs probes amounts to $\zeta \approx 1.25 \times 10^{-3}$, as introduced in Sec. 7.2 for the fourth-order cumulant S_4. While the nuclear Zeeman term is negligible in small magnetic fields, the magnetic field strength applied in the experiment is large enough so that it becomes relevant to the spin dynamics.

With nuclear Zeeman energy taken into account, a completely different behavior for the long-time limit of $G_4(t, 2t, t)$ emerges, as presented in Fig. 8.6. In the larger left panel of the figure, $G_4(t, 2t, t)$ is plotted up to $4\,\mu$s for different magnetic field strengths. Again the low-pass filter was employed to suppress the finite size noise in the long-time evolution. The dimensionless fields $b_x = 50, 100, 115, 130, 160, 200$ can be translated to physical units of $B_x = |\vec{B}_{\text{ext}}| = 1.03, 2.07, 2.38, 2.68, 3.31, 4.14\,\text{T}$. The data presented in Fig. 8.6 is calculated using ED with only $N = 5$ nuclear 3/2-spins, a uniform average ratio $\zeta = 1.25 \times 10^{-3}$ and averaged over $N_c = 32$ configurations of $\{A_k\}$.

For magnetic fields where the nuclear Zeeman energy is considerably lower than ω_{fluc}, $b_x = 50, 100$, the results are very similar to those for $\zeta = 0$. Within nanoseconds, $G_4(t, 2t, t)$ decays to its asymptotic magnetic field dependent long-time limit defined by

$$G_{\text{lim}}(b_x) = \lim_{t\to\infty} G_4(t, 2t, t). \tag{8.1.13}$$

The magnetic field dependency of $G_{\text{lim}}(b_x)$ is shown as blue squares in the lower right panel of Fig. 8.6. A considerably different picture emerges once b_x exceeds $b_x = 100$. While the long-time limit is magnetic field independent for $\zeta = 0$, for $\zeta = 1.25 \times 10^{-3}$ $G_{\text{lim}}(b_{\text{ext}})$ monotonically increases with b_x. The increase approaches a plateau for large fields, as $G_{\text{lim}}(b_x)$ cannot is limited by the analytic asymptotic value 3/8.

We analyze the slow long-time decay of $G_4(t, 2t, t)$ by introducing the fit function

$$G_4^{\text{fit}}(t, 2t, t) = G_{\text{lim}}(b_x) + \xi \exp(-2t/T_2^{\text{G}}) \tag{8.1.14}$$

parametrized by the amplitude ξ and the additional exponential decay time T_2^{G} in order to compare our results to the experimental findings by Bechtold et al. [72]. These fits are plotted as dashed lines along with the $G_4(t, 2t, t)$ curves obtained by ED in the left panel of Fig. 8.6. The decoherence time T_2^{G} extracted is plotted as a function of the external magnetic field in the upper right panel of Fig. 8.6. For small magnetic fields, T_2^{G} is small due to the rapid decay and difficult to extract. It rapidly increases around $b_x = 115$, which translates to $B_x = 2.38\,\text{T}$. This agrees excellently with the experimental findings of Ref. [72]. We obtained values

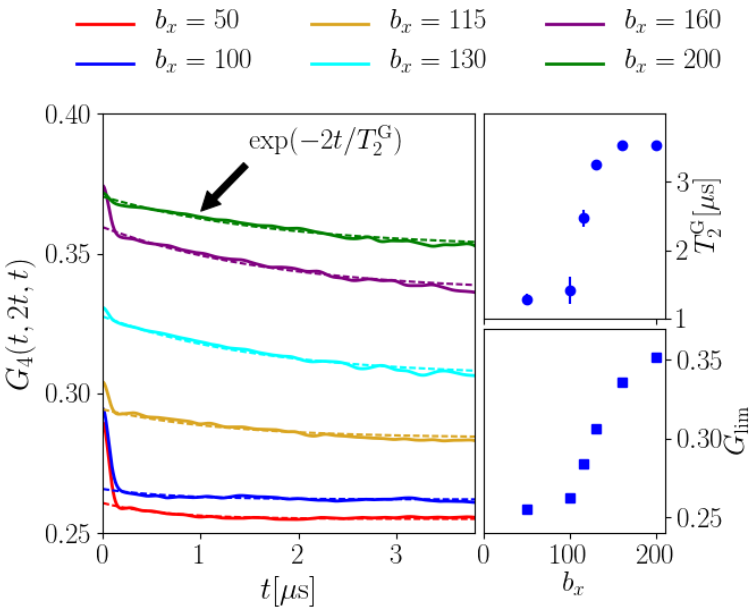

Figure 8.6: $G_4(t, 2t, t)$ as a function of t for different external magnetic fields. and a relative strength of the Zeeman splitting of $\zeta = 1.25 \times 10^{-3}$. The decoherence time T_2^{G} and the convergence level G_{lim} are plotted against the external magnetic field b_x. A low pass filter was utilized to suppress finite size oscillations. In the upper right panel, the decay time T_2^{G} is plotted in blue dots. The long-time limit G_{lim} is shown in the lower right as blue squares. The dashed lines show the ED data fitted with Eq. (8.1.14). Parameters: $N = 5$ with $I = \frac{3}{2}$ and $Q_r = 0.15$. Data presented in the plot has been previously published in Ref. [107].

of $T_2^{\mathrm{G}} \approx 3.5\mu\mathrm{s}$ for $B_x = 4.14\,\mathrm{T}$, while Bechtold et al. reported $T_2^{\mathrm{G}} = 1.4 \pm 0.1\,\mu\mathrm{s}$ for an external magnetic field of $B_x = 4\,\mathrm{T}$. The experimental data points presented in Fig. 4 (a) of Ref. [72] can also be fitted by a larger T_2^{G}. If only the data points for the long-time decay $t > 300\,\mathrm{ns}$ are taken into account, T_2^{G} between $2 - 5\,\mu\mathrm{s}$ are found. This indicates that the values for T_2^{G} depend quite strongly on the details of the fit procedure.

$N = 5$ is a very small number of nuclear spins, but it is the highest odd-numbered bath size our method utilizing all eigenenergies obtained by ED can calculate. But $G_4(t, 2t, t)$ can be accessed for $N = 7$ with the numerically expensive Lanczos approach with restart outlined in Sec. 5.4. The results of this calculation are shown in Fig. 8.7. The larger the external magnetic field, the shorter the time evolution step will be for a given Krylov space dimension M. Since the magnetic fields needed to observe a long-time exponential decay are quite high, using this method presents a challenge. The Krylov depth used for these calculations is $M = 128$. The propagation times were chosen dependent on the external magnetic field strength: For the magnetic field strengths $b_x = 50, 100, 130, 160, 200$ the propagation times are $\delta t = 1.2\,\mathrm{ns}, 0.6\,\mathrm{ns}, 0.6\,\mathrm{ns}, 0.3\,\mathrm{ns}, 0.3\,\mathrm{ns}$ for a single restart step. Since the computation for the highest magnetic fields requires two-

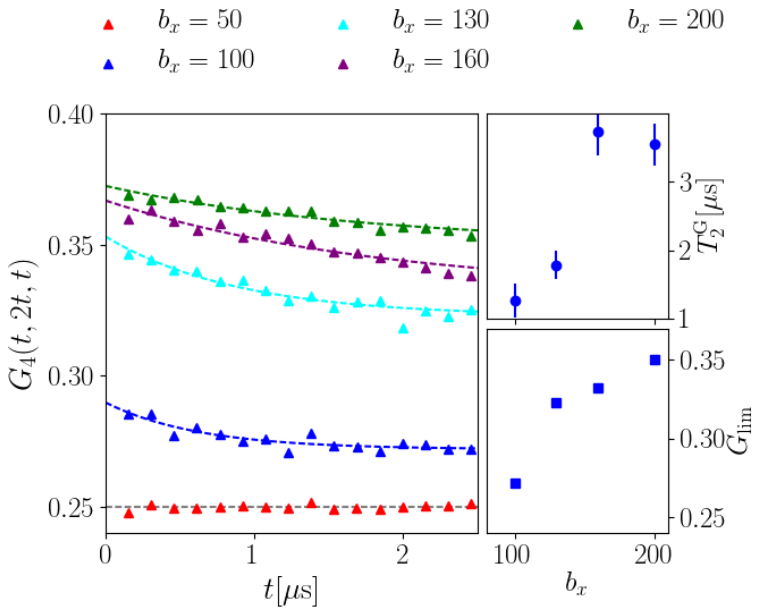

Figure 8.7: Single values of $G_4(t, 2t, t)$ dependent on t for different external magnetic fields and $\zeta = 1.25 \times 10^{-3}$. Computed with a Lanczos algorithm with a Krylov depth $M = 128$ and propagation times between restarts between $\delta t = 0.3\,\text{ns}$ and $\delta t = 1.2\,\text{ns}$ depending on the magnetic field strength. The decoherence time T_2^G and the convergence level G_{lim} are plotted against the external magnetic field b_x. In the upper right panel, the decay time T_2^G is plotted in blue dots. The long-time limit G_{lim} is shown in the lower right in blue squares. The dashed lines show the ED data fitted with Eq. (8.1.14). Parameters: $N = 7$ with $I = \frac{3}{2}$ and $Q_r = 0.15$. The data for $b_x = 200$ has been previously published in Ref. [107].

week runs on our HPC cluster, $G_4(t, 2t, t)$ was only calculated for a small number of times.

The results of the Lanczos method for do not show a significant difference to the results of the $N = 5$ ED calculation, which leads us to the conclusion that the long-time dynamics extracted from the ED computation do not contain significant finite size errors. As for $N = 5$, the maximum decay time was found to be $T_2^G \approx 3.5\,\mu\text{s}$ for $N = 7$. It was not possible to fit an exponential curve to the data for $b_x = 50$, since $G_4(t, 2t, t)$ is already decayed down to $1/4$ at the first data point $t = 152\,\text{ns}$.

One question is how the fourth-order correlation depend on the different quadrupolar coupling strengths Q_r. Figure 8.8 depicts $G_4(t, 2t, t)$ for $N = 7$, $b_x = 160$, $\zeta = 1.25 \times 10^{-3}$ for different Q_r, computed via the Lanczos method with a Krylov depth $M = 128$ and a distance between restarts of $\delta t = 0.3\,\text{ns}$. The quadrupolar coupling strength has a noticeable influence on the correlation decay: For higher Q_r, the correlation function is much earlier at a lower level. It should be noted that the difference in correlation for $Q_r = 0.15$ and $Q_r = 0.35$ is higher for small times than in the long time limit. Most of the additional decay caused by the

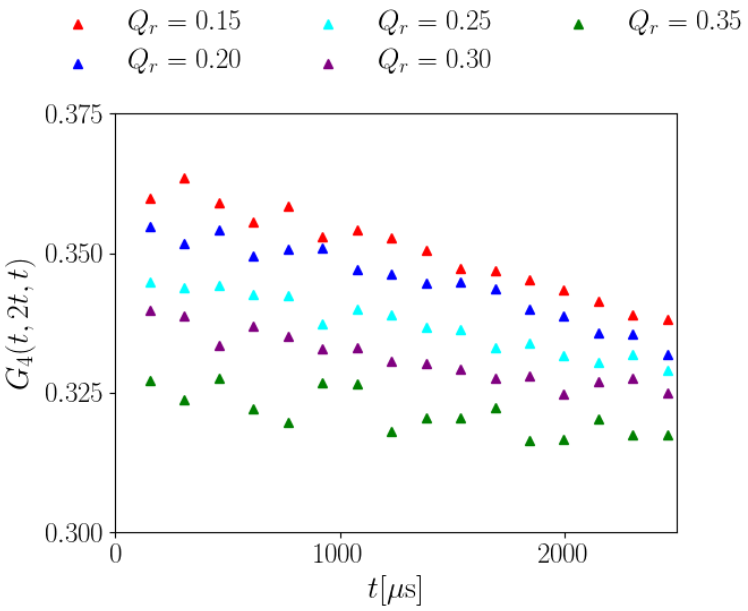

Figure 8.8: Single values of $G_4(t, 2t, t)$ dependent on t for different quadrupolar coupling strengths Q_r, an external magnetic field $b_x = 160$ and $\zeta = 1.25 \times 10^{-3}$. Computed with a Lanczos algorithm with a Krylov depth $M = 128$ and a propagation time between restarts $\delta t = 0.3\,\text{ns}$. Parameters: $N = 7$ with $I = \frac{3}{2}$.

higher quadrupolar coupling takes place in the short time scale.

Another topic of interest is the influence of ζ on the decay. While $\zeta = 1.25 \times 10^{-3}$ is, approximated, the average value for the InGaAs probe used in the experiment by Bechtold et al. [72], our theoretical simulations can also compute G_4 for a different material with a higher ζ. Figure 8.9 shows $G_4(t, 2t, t)$ for $\zeta = 2.5 \times 10^{-3}$. All other parameters are identical to those of the results presented in Fig. 8.7. For $\zeta = 2.5 \times 10^{-3}$, the long-time exponential decay sets in at smaller magnetic fields. This effect is expected, since it is the Zeeman energy ζb_x that causes the crossover from immediate decorrelation to slow exponential decay. The qualitative change is that the exponential decay is more pronounced for $\zeta = 2.5 \times 10^{-3}$, because the long-time limit G_{lim} drops lower than for $\zeta = 1.25 \times 10^{-3}$ at comparable magnetic fields. The decay time of G_4 in a large magnetic field ($b_x = 100$) is about $T_2^G \approx 3.2\,\mu\text{s}$. Note that due to the expensive computation of $N = 7$, no data for $t > 2.5\,\mu\text{s}$ was calculated. Values for G_{lim} had to be estimated based on ED calculations for $N = 5$.

Quadrupolar interaction requires nuclear bath spin lengths of $I = 3/2$ or longer. This severely limits the bath size computationally viable for quantum mechanical calculations. The long time limit of $C_2(t)$ with quadrupolar coupling showed an even-odd behaviour in regards to bath size, as presented in Fig. 6.6. In order to minimize long-time finite size effects, we focused on odd-numbered baths.

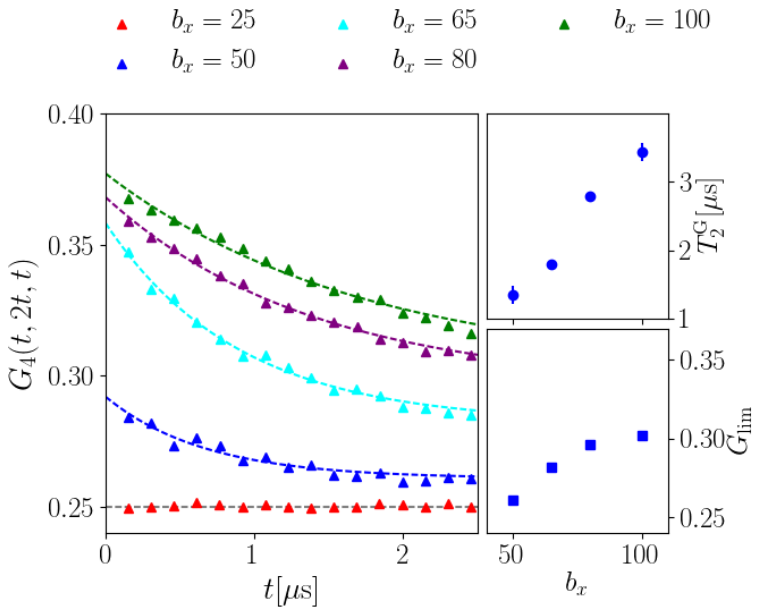

Figure 8.9: $G_4(t, 2t, t)$ calculated with identical parameter values as presented in Fig. 8.7, except that $\zeta = 2.5 \times 10^{-3}$. The range of magnetic field strengths was also changed accordingly.

Note that the limitation of the energy spectrum of the Hamiltonian introduce finite-size errors which will influence $G_{\lim}(b_x)$. In the real system with $\approx 10^5$ nuclear spins, the hyperfine coupling distribution function $P(A)$ is nearly continuous. This then leads to a nearly continuous energy spectrum, increasing the phase space for spin-flip processes. For $N \to \infty$, $G_{\lim}(b_x)$ will be smaller than in the computations presented here. But since these finite size corrections of $G_{\lim}(b_x)$ only influence the prefactor ξ, the decay time T_2^G should remain unaltered.

8.2 Spin Echo Measurement of Fourth Order Correlation

8.2.1 Experimental Realization

A different fourth-order correlation function was recently measured via spin echo method [29]. Here, the intrinsic long-time decoherence scale T_2 is determined by applying a $\pi/2 - \pi - \pi/2$ pulse sequence to a singly negatively charged QD that has been initialized into the ground state. A strong external magnetic field is applied in Voigt geometry, perpendicular to the optical axis. In our coordinate system, the optical axis is in z direction and the magnetic field in x direction. The index of the spin states $|\uparrow\rangle_{\mathrm{opt}/B}$ denotes whether the quantization axis is oriented along the optical axis or the magnetic field.

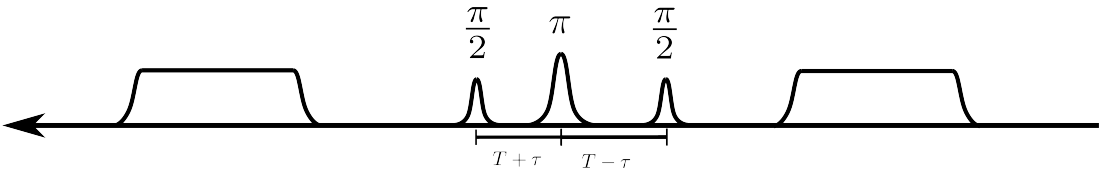

Figure 8.10: The laser pulse sequence used in the spin echo experiment measuring a fourth-order spin correlation function. The first pulse pumps the system into the $|\uparrow\rangle_B$ state. Then follows the $\pi/2 - \pi - \pi/2$ Hahn echo sequence, where the laser pulses cause Rabi rotations in the plane perpendicular to the magnetic field. At $\tau = 0$, if no decorrelation has taken place, the spin should be in the $|\uparrow\rangle_B$ again after the second $\pi/2$ pulse. Lastly, another pump pulse is applied. If the spin is in the $|\downarrow\rangle_B$ state, the excitation and resulting trion decay will lead to a measurable emission of photons.

The magnetic field splits the electron spin states into the two states $|\uparrow\rangle_B$ and $|\downarrow\rangle_B$. The system is pumped by a 26 ns long circularly polarized σ^- pulse resonant with the transition between $|\downarrow\rangle_B$ and the related trion state. This can be expressed in the quantization axis oriented along the optical axis as $|\downarrow\rangle_B = (|\uparrow\rangle_{\text{opt}} - |\downarrow\rangle_{\text{opt}})/\sqrt{2}$. The $|\uparrow\rangle_{\text{opt}}$ state is not affected by the pulse, but the $|\downarrow\rangle_{\text{opt}}$ contribution is excited into the trion state $|\downarrow\uparrow, \Downarrow\rangle_{\text{opt}}$. As the trion decays and the unaffected spin $|\uparrow\rangle_{\text{opt}}$ rotates in the magnetic field, a polarization in $|\uparrow\rangle_{\text{opt}}$ is created. Since $|\uparrow\rangle_{\text{opt}} = (|\uparrow\rangle_B + |\downarrow\rangle_B)/\sqrt{2}$, the pumping drains the $|\downarrow\rangle_B$ state and initializes the system in $|\uparrow\rangle_B = (|\uparrow\rangle_{\text{opt}} + |\downarrow\rangle_{\text{opt}})/\sqrt{2}$. This corresponds to an orientation along the x axis in our coordinate system.

The first spin-echo $\pi/2$-pulse causes a coherent rotation around the y axis into the xz-plane, after which the spin freely precesses around the magnetic field for a time $T + \tau$. Then the π-pulse is applied, which reverses the direction of the spin dephasing. The spin again precesses in the xz-plane for a time $T - \tau$, bringing the total duration of the pulse sequence to $2T$. The second $\pi/2$-pulse will then rotate the spin up into the initial state oriented along the x axis. In the experiment, the same circularly polarized pump pulse is used to read out the coherence. If the spin has flipped during the process, the pump pulse will excite an exciton state, which will decay emitting a photon.

We want to quantify the probability of finding the spin again in its initial state

$$|g_0\rangle = \frac{|\uparrow\rangle_{\text{opt}} + |\downarrow\rangle_{\text{opt}}}{\sqrt{2}} \tag{8.2.1}$$

after the pulse sequence. The probability amplitude of finding the system with the central spin in the $|g_0\rangle$-state after the time $2T$ can be described by

$$\begin{aligned} A(T, \tau, \vec{m}, \vec{m'}) &= \langle g_0, \vec{m}| \, U_y(\pi/2) e^{-\mathrm{i}H(T-\tau)} \\ &\quad \times U_y(\pi) e^{-\mathrm{i}H(T+\tau)} U_y(\pi/2) \, |g_0, \vec{m'}\rangle \, . \end{aligned} \tag{8.2.2}$$

$U_y(\phi)$ is the rotation matrix around the y axis with the angle ϕ. The nuclear spin configurations $\vec{m} = (m_1, m_2, ..., m_N)^T$ are neither measured nor initialized

and are, therefore, unknown. In order to obtain the total probability, we need to sum over all nuclear contributions

$$P_{g_0 g_0}(T,\tau) = \frac{2}{D}\sum_{\vec{m},\vec{m}'} |A(T,\tau,\vec{m},\vec{m'})|^2 \tag{8.2.3}$$

$$\begin{aligned} = \frac{2}{D}\sum_{\vec{m}} &\langle g_0,\vec{m}| U_y^\dagger(\pi/2) e^{\mathrm{i}H(T+\tau)} U_y^\dagger(\pi) \\ &\times e^{\mathrm{i}H(T-\tau)} U_y^\dagger(\pi/2)\hat{P}_{g_0} U_y(\pi/2) e^{-\mathrm{i}H(T-\tau)} \\ &\times U_y(\pi) e^{-\mathrm{i}H(T+\tau)} U_y(\pi/2)\,|g_0,\vec{m}\rangle \end{aligned} \tag{8.2.4}$$

where $D/2$ is the number of nuclear spin configurations and

$$\hat{P}_{g_0} = |g_0\rangle\langle g_0| \tag{8.2.5}$$

is the projector onto the state $|g_0\rangle$. We define

$$A = U_y(\pi/2)\hat{P}_{g_0}U_y^\dagger(\pi/2) \tag{8.2.6}$$

$$\bar{A} = U_y^\dagger(\pi/2)\hat{P}_{g_0}U_y(\pi/2) \tag{8.2.7}$$

$$B = U_y(\pi) \tag{8.2.8}$$

and gain the fourth-order correlation function

$$P_{g_0,g_0}(T,\tau) = \frac{2}{D}\mathrm{Tr}[B^\dagger \bar{A}(T-\tau)BA(-T-\tau)]. \tag{8.2.9}$$

We use the fact that the spin operators are the generators of electron-spin rotations and write the rotation matrices as

$$U_y(\pi/2) = \mathrm{e}^{-\mathrm{i}\sigma_y\pi/4} = \frac{1}{\sqrt{2}}(\mathbb{1} - \mathrm{i}\sigma_y) \tag{8.2.10}$$

$$U_y(\pi) = \mathrm{e}^{-\mathrm{i}\sigma_y\pi/2} = -\mathrm{i}\sigma_y. \tag{8.2.11}$$

Therefore, we obtain for the operators in $P_{g_0,g_0}(T,\tau)$

$$A = \bar{A} = \frac{1}{2}\mathbb{1} - S_z \tag{8.2.12}$$

$$B = -2\mathrm{i}S_y \tag{8.2.13}$$

and can finally express the probability of finding the spin in its initial state after the pulse sequence as [107]

$$P_{g_0,g_0}(T,\tau) = \frac{1}{2} - 8\left\langle S_y S_z(T-\tau) S_y S_z(-T-\tau)\right\rangle. \tag{8.2.14}$$

With the transversal magnetic field applied in x direction, the system is rotationally symmetric in the yz plane. Note that the fourth-order correlation derived here is not the same as the G_4 function derived in the previous section. While G_4 quantifies the correlation of S_z with itself at different points in time, $P_{g_0,g_0}(T,\tau)$ describes the correlation between two different electron spin components, S_z and S_y. Due to the isotropy in the xy plane, we can expect similar behaviour to G_4, but the two experiments discussed in this chapter do not measure the same correlation function.

8.2.2 FOA Results for the Spin Echo

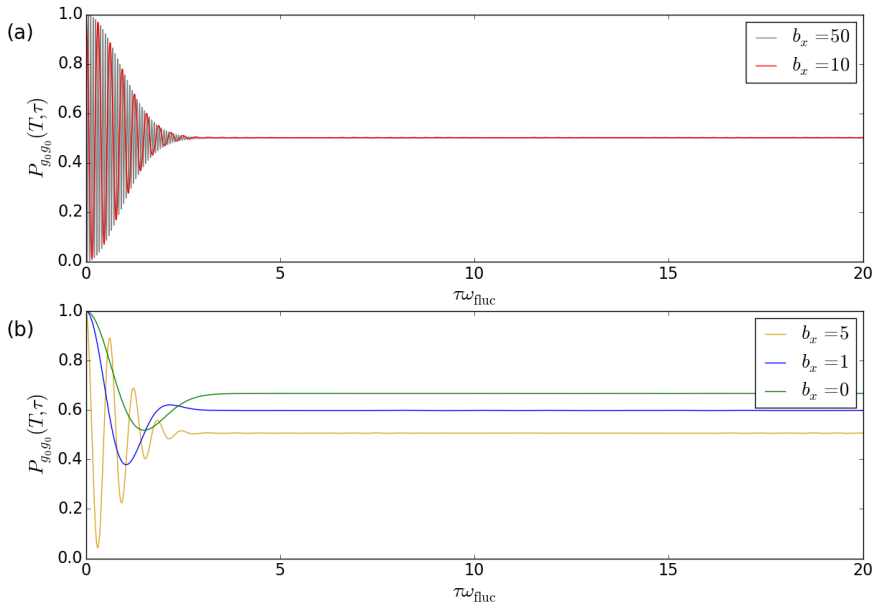

Figure 8.11: $P_{g_o g_0}(\tau, T)$ computed in the FOA averaged over 10^6 Overhauser fields. Panel (a) shows the behaviour at higher magnetic fields ($b_x = 10$, 50), while panel (b) features $P_{g_o g_0}(\tau, T)$ at small to intermediate fields ($b_x = 0$, 1, 5).

The spin echo fourth-order correlation function $P_{g_0,g_0}(T,\tau)$ as introduced in Eq. (8.2.14) is given by

$$P_{g_0,g_0}(T,\tau) = \frac{1}{2} + \frac{1}{2}\left(n_3^2 + (n_1^2 + n_2^2)\cos(2\omega_{\mathrm{L}}\tau)\right) \tag{8.2.15}$$

with a normalized and constant total magnetic field vector $\vec{n} = (\vec{B}_{\mathrm{ext}} + \vec{B}_N))|\vec{B}_{\mathrm{ext}} + \vec{B}_N|$ in the FOA. The Overhauser field $\vec{B}_N$ is randomly generated from a Gaussian distribution. Note that the dependence on T vanishes, since with the nuclear spin dynamics frozen no information is lost no matter how long ago the system was initialized. By comparing the FOA solution for $C_2(t)$ for a given frozen Overhauser field $\vec{B}_N$ in Eq. (5.1.13) to the FOA solution of $P_{g_0,g_0}(T,\tau)$ derived in Eq. (8.2.15), one notices that in the case of frozen nuclear dynamics

$$P_{g_0,g_0}(T,\tau) = \frac{1}{2} + 2C_2(2\tau). \tag{8.2.16}$$

Averaging over 10^6 randomly generated Overhauser fields yields the results presented in Fig. 8.11. The results agree with Eq. (8.2.16). Figure 8.11 (a) shows $P_{g_0,g_0}(T,\tau)$ for higher magnetic fields ($b_x = 10, 50$), while Fig. 8.11 (b) depicts $P_{g_0,g_0}(T,\tau)$ for smaller magnetic fields ($b_x = 0, 1, 5$). For magnetic fields $b_x > 1$, $P_{g_0,g_0}(T,\tau)$ quickly decays to 1/2, while oscillating with $2\omega_L$. For smaller magnetic fields, the probability of measuring the spin in its initial state after the pulse sequence stays above 1/2 for the limit $\tau \to \infty$.

8.2.3 $P_{g_0,g_0}(T,\tau)$ for the Full Hamiltonian

In general, the fourth-order correlation function $P_{g_0,g_0}(T,\tau)$ cannot be reduced to a second-order correlation $C_2(2\tau)$. Due to nuclear spin dynamics and quadrupolar couplings, information is not retained for an arbitrary time T.

In order to compare the theoretical results with the experimental measurements, we investigate both $P_{g_0,g_0}(T = \text{const},\tau)$ as a function of τ and the oscillation amplitude of $P_{g_0,g_0}(T,\tau=0) = \bar{P}_{g_0,g_0}(T)$ as a function of T for several different external magnetic fields. Like $G_4(t,2t,t)$ discussed in the previous section, the amplitude of $P_{g_0,g_0}(T,\tau)$ exhibits a long-time exponential decay that can be fitted by

$$\bar{P}_{g_0,g_0}(T) = P_{\text{lim}} + \xi \exp\left(-\frac{2T}{T_2^{\text{P}}}\right). \tag{8.2.17}$$

The same system parameters were employed for the calculation of $P_{g_0,g_0}(T,\tau)$ using ED, as for the computation of $G_4(t,2t,t)$ in Fig. 8.6. This is done in order to show that the same material parameters can explain both experiments. For a constant T, $P_{g_0,g_0}(T,\tau)$ oscillates with twice the Larmor frequency as a function of τ. This has already been understood by deriving the FOA result in Eq. (8.2.15). But since the FOA accounts for the decay down to a asymptote of $P_{\text{lim}} = \lim_{T\to\infty} P_{g_0,g_0}(T,0) = 1/2$, the additional decay observed in experiment and fully quantum mechanical simulation is caused by the competition between the nuclear Zeeman energy and the quadrupolar interaction.

In the results of $P_{g_0,g_0}(T,\tau)$ obtained by ED for $N = 5$, $\zeta = 1.25 \times 10^{-3}$ and $Q_r = 0.15$, the decay of the spin-echo amplitude is noticeable, but not as pronounced as in the experiment. Exponential fitting for different external magnetic field strengths yields decay times T_2^G that are similar to the decay times reported by experiment, but long-time limits P_{lim} that lie above the experimental values [29]. Figure 8.12 shows the long-time decay of the amplitude $\bar{P}_{g_0,g_0}(T)$ for two different magnetic fields, $b_x = 130$ and $b_x = 160$. These dimensionless magnetic field strengths translate with an electron g-factor of $g_{\text{e}} = 0.442$ as reported in the experiment [29] to $B_x = 3.34\,\text{T}$ and $B_x = 4.11\,\text{T}$, respectively. On the left panels of Fig. 8.12 of the spin echo amplitude, the oscillations in τ are presented for two different times T in order to illustrate the decay of the echo amplitude.

Through applying the pulse sequence of $\pi/2-\pi-\pi/2$-pulses coherence can be maintained on a time scale of $\mathcal{O}(\mu\text{s})$, $T_2^{\text{P}} \gg T^*$. In Fig. 8.13, the decay time T_2^{P} is shown dependent on the externally applied magnetic field. The extracted dependence of $T_2^{\text{P}} \gg T^*$ on the external magnetic field strength concurs considerably well with the experimental data presented in Fig. 4, Ref. [29].

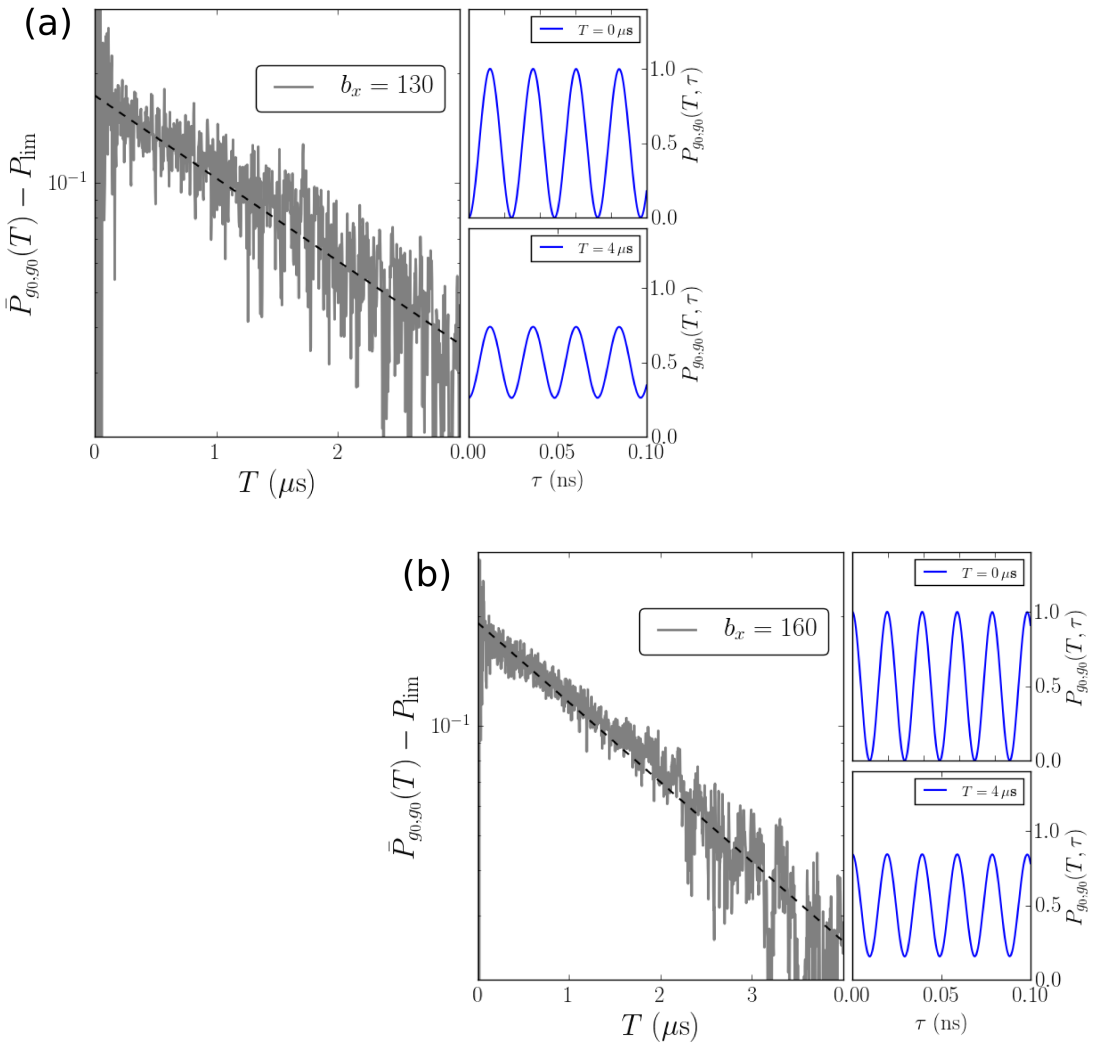

Figure 8.12: Exponential decay of the amplitude of $P_{g_0,g_0}(T, \tau = 0)$ with $N = 5$, here plotted for $b_x = 130$ in panel (a), and $b_x = 160$ in panel (b), which corresponds [29] to a magnetic field $B_x = 3.34\,\mathrm{T}$ and $B_x = 4.11\,\mathrm{T}$ for $g_\mathrm{e} = 0.442$. The decay time was fitted as $T_2^\mathrm{P} = 3.96\,\mu\mathrm{s}$. On the right hand side, $P_{g_0,g_0}(T, \tau)$ for a constant pulse distance T is shown, once for $T = 0\,\mu\mathrm{s}$ and once for $T = 2\,\mu\mathrm{s}$. The spin echo oscillates with twice the Larmor frequency, like $G_4(t, T, t)$ at $t \approx T/2$. All system parameters are equal to the ones used in Fig. 8.6 to describe the experiment by Bechtold et al [72]. Some of the data for $b_x = 160$ has been previously published in Ref. [107].

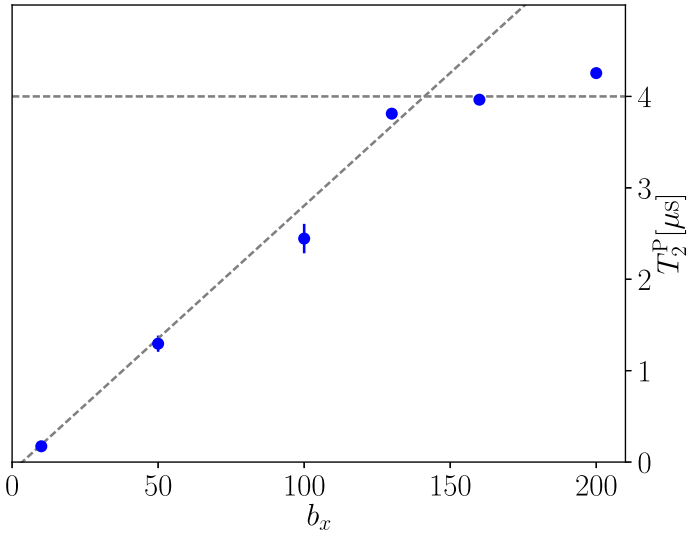

Figure 8.13: The decay time T_2^{P} of $\bar{P}_{g_0,g_0}(T)$ dependent on the external magnetic field B_x. The grey dashed lines are guides to the eye, indicating a rising slope that saturates at magnetic fields $b_x > 130$. With $g_{\mathrm{e}} = 0.442$ the saturation point is reached at $B_x \geq 3.5\,\mathrm{T}$ with a saturation level of $T_2^{\mathrm{P}} \approx 4\,\mu\mathrm{s}$. A higher saturation point $B_x = 4\,\mathrm{T}$ at a lower saturation level $T_2^{\mathrm{P}} \approx 3\,\mu\mathrm{s}$ was reported by Press et al. [29]. This plot is taken from [107].

8.3 Chapter Conclusion

This chapter dealt with two different fourth-order spin correlation functions in real time, both having been observed in recent experiments, The first part of this chapter discussed the three σ^+-pulses experiment conducted by Bechtold et al. [72], and the second part was dedicated to the analysis of the spin echo experiment presented by Press et al. [29].

In Sec. 8.1.1 we were able to show that the joint probability of measuring a central spin $|\downarrow\rangle$ twice at times t_1 and $t_1 + t_2$ in a single QD after initializing the electron spin in a spin $|\downarrow\rangle$ state is related to the fourth-order correlation function of the projection operator $P_\downarrow$ into the electron spin-$|\downarrow\rangle$ state, $G_4(t_1, t_1+t_2, t_1)$. G_4 was calculated via the FOA, the ED and and the Lanczos algorithm. We investigated the long-time behavior of G_4 with and without nuclear Zeeman splitting and quadrupolar interaction, and compared the results to the experimental findings reported by Bechtold et al. [53, 72]. $G_4(t, 2t, t)$ features a long time exponential decay in a strong transversal magnetic field, which cannot be understood with the semi-classical approximation or the full quantum dynamics within the CMS including electron and nuclear Zeeman term.

G_4 computed using ED for the simple CSM model is very similar to G_4 computed by the FOA, as both approaches agree well with the experiments concerning short time behavior but fail to explain the observed long time decay of G_4. By

extending the CSM with the nuclear-electric quadrupolar interaction and including the nuclear Zeeman splitting, both ED and the Lanczos method yield results which that qualitatively agree with the findings of the recent experiments [53,72]. If the nuclear Zeeman term is neglected ($\zeta = 0$) and nuclear quadrupolar coupling is introduced, G_4 features a rapid decay after the initial Larmor oscillations on a time scale of $t_{\text{decay}} \approx 10\,\text{ns}$. While this agrees well with the experimental findings for small magnetic fields, it is not sufficient for the understanding of the slow exponential decay observed when a large magnetic field is applied. We demonstrated that the nuclear Zeeman term is necessary to observe the crossover from a fast non-exponential decay in weak and intermediate magnetic fields to a slow exponential decay at larger magnetic fields. This is due to the competition between quadrupolar coupling, which induces decay, and nuclear Zeeman splitting, which suppresses decoherence. Above a threshold of $b_x \approx 100$, $G_4(t, 2t, t)$ featured a long-time exponential decay. The decay time T_2^G increases with the magnetic field strength until it reaches a plateau of $T_2 = 3.5\,\mu\text{s}$. This concurs qualitatively with the experimental results reported by Bechtold et al. [72].

In the second part of the chapter we derived that the spin echo measurement is described by a fourth-order spin correlation function $P_{g_0,g_0}(T, \tau)$. $P_{g_0,g_0}(T, \tau)$ is different from G_4 in that it is not related to an auto-correlation function of the spin component S_z, but involves both S_y and S_z. However, the decay mechanism is the same, and the long time behavior is qualitatively similar. Like $G_4(t, 2t, t)$, $\bar{P}_{g_0,g_0}(T)$ exhibits decay times that increase monotonically with the external magnetic field strength, until reaching a plateau for very high fields. However, the magnetic field dependency of the two long-time scales $T_2^{\text{G}}(b_x)$ and $T_2^{\text{P}}(b_x)$ differs. While $T_2^{\text{G}}(b_x)$ shows a very abrupt increase around $b_x \approx 115$, $T_2^{\text{P}}(b_x)$ exhibits a nearly linear increase before reaching the plateau. The saturation values are likewise not identical, with $T_2^{\text{P}} \approx 4\,\mu\text{s}$ and $T_2^{\text{G}} \approx 3.5\,\mu\text{s}$. This actually agrees very well with the experimental findings, since the saturation level of the decay time $T_2^{\text{P}}(b_x)$ reported in Ref. [29] is higher than the decay time obtained for $G_4(t, 2t, t)$ by Ref. [72]. Note, however, that the three pulse experiment measuring $G_4(t, 2t, t)$ did only extract T_2^{G} for a single magnetic field. Whether a saturation of the decay time at high magnetic fields as predicted by our calculations could be observed here experimentally remains a task for the future.

For the anti-diagonal of $G_4(t_1, t_2{+}t_2, t_1)$ at a fixed distance between the second probe pulse and the initial pump pulse ($t_1 + t_2 = T'$), i. e. $G_4(t_1, T', t_1)$, G_4 oscillates with $2\omega_L$ and a Gaussian envelope around $t_1 = T'/2$. The cause of the frequency doubling can be analytically understood in the FOA. The Gaussian envelope is caused by the dephasing introduced by the Overhauser field. $P_{g_0,g_0}(T, \tau)$ exhibits a similar behaviour at constant T.

In conclusion, the CSM model expanded by nuclear-electric quadrupolar coupling and nuclear Zeeman splitting describes fourth-order correlation functions in QD adequately. Quadrupolar coupling induces an immediate decay of the correlation, while an increasing nuclear Zeeman splitting suppresses this effect leading to a long-time exponential decay in large magnetic fields. Applying the full model

predicts a long-time exponential decay of the fourth-order correlation functions dependent on the transversal magnetic field strength, that agrees with the recent experimental results qualitatively as well as quantitatively.

Chapter 9

Conclusion

The primary focus of this thesis was the investigation of fourth-order spin correlation in QD systems. Both fourth-order spin correlation functions in real time as well as in the frequency domain were calculated using classical and quantum mechanical methods. Making the connection with experiments, we were able to prove that the extended CSM with quadrupolar couplings is a good description of the spin dynamics in the QD system, and is capable of reproducing the experimental findings qualitatively and quantitatively. Most importantly, this work unmistakably shows that fourth-order correlators, be it in the real time or the frequency domain, yield information beyond that of the well known second-order correlation function and second-order noise.

Different methods were presented in order to calculate fourth-order correlation. The FOA describes the correlation adequately for short times, and enables us to simulate an infinite nuclear spin bath. A scheme relying on ED of the Hamilton matrix yields numerically exact results, but is computationally limited in regards to bath size. Another method based on Lanczos time propagation can simulate a larger bath sizes, but is computationally expensive, especially for large magnetic fields.

To investigate fourth-order correlation, first second-order correlation function has to be reviewed. After presenting the well known general features of the second-order electron spin correlation, we discussed the influence of the hyperfine coupling distribution and the nuclear-electric quadrupolar coupling on the long-time spin decay. By making a connection between our numerical results of second-order spin correlation influenced by quadrupolar coupling and previous experiments [53], we gauged the quadrupolar coupling strength Q_r with the experimentally observed long-time decay. The influence of the nuclear spin length I on the decay induced by quadrupolar coupling was investigated. We found an even-odd behaviour of the decay in regard to bath size for small N.

Furthermore, we analyzed the second-order spin bath correlation function both analytically and numerically in the CSM. The CSM is exactly solvable for

homogeneous coupling constants, which makes it possible to obtain the auto-correlation function of the total bath polarization for an arbitrary number of spins. The effect of an inhomogeneous hyperfine coupling distribution function was studied analytically in the hmf limit. With a nuclear Zeeman term, the spin bath noise exhibits a peak at the frequency corresponding to the nuclear Zeeman energy. The shape of that peak is given by the hyperfine coupling distribution. This makes it possible to measure the distribution of the A_k directly through spin noise spectroscopy, with the location of the peaks goven by the Zeeman energy of the corresponding isotopes. A numerical approach with Lanczos time propagation shows that the analytical methods provide an adequate description of the spin bath correlation, especially at high magnetic fields.

The fourth-order cumulant $S_4(\omega_1, \omega_2)$ was investigated using the FOA, ED and a classical EOM approach. For the CSM, all methods produce congruent results. The quantum mechanical bispectrum converges to the result of the classical simulation when the quantum mechanical spectrum of eigenenergies approaches a continuous distribution, for larger bath sizes and a large nuclear spin length. But even calculations with a small number of nuclear spins provide a good representation of a larger bath bispectrum. The bispectrum is made up of fourth-order and second-order spin noise contributions. The fourth-order contributions constitute the positive correlation to the bispectrum, and are only non-zero for $\omega_1 = \omega_2$. When the quadrupolar couplings are added, the fourth-order contribution exhibits a broadening around the frequency diagonal $\omega_1 = \omega_2$. While second-order noise is not influenced by quadrupolar coupling when a transversal magnetic field is present, the fourth-order spin noise changes depending on the quadrupolar coupling strength. This proves that fourth-order correlation function provides additional information compared to the second-order correlation function. Also, the simple linear response theory employed in this work yields congruous results to those obtained through elaborate continuous measurement theory presented in Ref. [76]. Hence the assumption of non-perturbative measurement is justified, since the perturbation included in Ref. [76] does not change the resulting S_4.

We were able to show analytically that the two recently conducted experiments, the three σ^+-pulse experiment [72] and the spin echo experiment [29], actually measure two different fourth-order correlation functions in real time. The joint probability of measuring the electron spin in a QD in its spin-$|\downarrow\rangle$ state at t_1 and $t_1 + t_2$ after initializing it in that same state is described by the fourth-order correlation function of the projection operator into the electron spin-$|\downarrow\rangle$ state, $P_\downarrow$. The short time dynamics of this fourth-order correlator, $G_4(t_1, t_1 + t_2, t_1)$, can be adequately explained by FOA or ED in the CSM. However, neither of these approaches showed the crossover behaviour of fast decay for a small external magnetic field and a slow exponential decay for large magnetic fields. By introducing quadrupolar interaction and nuclear Zeeman splitting to the model, we were able to show long time exponential decay that concurs with the observations made in the experiment [72]. The decay rate T_2^G increases with the transversal magnetic field strength before reaching a plateau for large magnetic fields of about $T_2^G = 3.5\,\mu\text{s}$. We derived that the spin echo amplitude measured

in Ref. [29] is described by a fourth-order spin correlation function $P_{g_0,g_0}(T,\tau)$, involving two different electron spin components, S_y and S_z. We showed that the decay mechanisms are the same and that both correlation functions exhibit qualitatively similar long-time decay. This was expected, as the system is isotropic in the yz plane. The decay times of both P_{g_0,g_0} and G_4 reach a plateau for large external magnetic fields. The asymptotic decay time of G_4 is lower, $T_2^G = 3.5\,\mu\text{s}$, than that of P_{g_0,g_0}, where $T_2^P = 4\,\mu\text{s}$. Since Press et al. observed a higher asymptotic decay time $T_2^P = 3\,\mu\text{s}$ [29] than Bechtold el al. [72], who reported $T_2^G = 1.4\,\mu\text{s}$ for $B_x = 4\,\text{T}$, this agrees well with experiments.

In conclusion, fourth-order spin correlation in QD systems is well described by an enhanced CSM including quadrupolar couplings and nuclear Zeeman splitting. Fourth-order correlation yields information about the system beyond the well known second-order correlation function, and is, therefore, highly interesting for future studies.

Bibliography

[1] G.E. Moore. Cramming more components onto integrated circuits. *Proceedings of the IEEE*, 86:82–85, 02 1998.

[2] R. P. Feynman. Simulating physics with computers. *International Journal of Theoretical Physics*, 21(6):467–488, Jun 1982.

[3] E. Bernstein and U. Vazirani. Quantum complexity theory. In *Proceedings of the Twenty-fifth Annual ACM Symposium on Theory of Computing*, STOC '93, pages 11–20, New York, NY, USA, 1993. ACM.

[4] D. Deutsch and R. Penrose. Quantum theory, the church-turing principle and the universal quantum computer. *Proceedings of the Royal Society of London A: Mathematical, Physical and Engineering Sciences*, 400:97–117, July 1985.

[5] D. Deutsch and R. Jozsa. Rapid solution of problems by quantum computation. *Proceedings of the Royal Society of London A: Mathematical, Physical and Engineering Sciences*, 439:553, Dec 1992.

[6] P. W. Shor. Algorithms for quantum computation: Discrete logarithms and factoring. In *Proceedings of the 35th Annual Symposium on Foundations of Computer Science*, SFCS '94, pages 124–134, Washington, DC, USA, 1994. IEEE Computer Society.

[7] P. W. Shor. Polynomial-time algorithms for prime factorization and discrete logarithms on a quantum computer. *SIAM J. Comput.*, 26(5):1484–1509, October 1997.

[8] Y. Makhlin, G. Schön, and A. Shnirman. Quantum-state engineering with josephson-junction devices. *Rev. Mod. Phys.*, 73:357–400, May 2001.

[9] M. A. Sillanpää, J. I. Park, and R. W. Simmonds. Coherent quantum state storage and transfer between two phase qubits via a resonant cavity. *Nature*, 449(438), September 2007.

[10] A. A. Houck, H. E. Türeci, and J. Koch. On-chip quantum simulation with superconducting circuits. *Nature Physics*, 8(4):292–299, 4 2012.

[11] L. M. K. Vandersypen and I. L. Chuang. NMR techniques for quantum control and computation. *Rev. Mod. Phys.*, 76:1037–1069, Jan 2005.

[12] J. A. Jones. Quantum computing with nMR. *Progress in Nuclear Magnetic Resonance Spectroscopy*, 59(2):91 – 120, 2011.

[13] E. B. Kane. Kane, b. e. a silicon-based nuclear spin quantum computer. *Nature*, 393:133–137, 05 1998.

[14] R. Hanson, V. V. Dobrovitski, A. E. Feiguin, O. Gywat, and D. D. Awschalom. Coherent dynamics of a single spin interacting with an adjustable spin bath. *Science*, 320(5874):352–355, 2008.

[15] F. Jelezko, T. Gaebel, I. Popa, A. Gruber, and J. Wrachtrup. Observation of coherent oscillations in a single electron spin. *Phys. Rev. Lett.*, 92:076401, Feb 2004.

[16] F. Jelezko and J. Wrachtrup. Single defect centres in diamond: A review. *physica status solidi (a)*, 203(13):3207–3225, 2006.

[17] C. H. Bennett and D. P. DiVincenzo. Quantum information and computation. *Nature*, 404:247 EP –, Mar 2000. Review Article.

[18] G. Burkard, H. Engel, and D. Loss. Spintronics and quantum dots for quantum computing and quantum communication. *Fortschritte der Physik*, 48(9?11):965–986, 2000.

[19] D. Loss and D. P. DiVincenzo. Quantum computation with quantum dots. *Phys. Rev. A*, 57:120–126, Jan 1998.

[20] A. V. Khaetskii, D. Loss, and L. Glazman. Electron spin decoherence in quantum dots due to interaction with nuclei. *Phys. Rev. Lett.*, 88(18):186802, 2002.

[21] R. Hanson, L. P. Kouwenhoven, J. R. Petta, S. Tarucha, and L. M. K. Vandersypen. Spins in few-electron quantum dots. *Rev. Mod. Phys.*, 79:1217–1265, Oct 2007.

[22] J. M. Elzerman, R. Hanson, L. H. Willems van Beveren, B. Witkamp, L. M. K. Vandersypen, and L. P. Kouwenhoven. Single-shot read-out of an individual electron spin in a quantum dot. *Nature*, 430:431 EP –, Jul 2004.

[23] N. H. Bonadeo, J. Erland, D. Gammon, D. Park, D. S. Katzer, and D. G. Steel. Coherent optical control of the quantum state of a single quantum dot. *Science*, 282(5393):1473–1476, 1998.

[24] A. Greilich, A. Shabaev, D. R. Yakovlev, Al. L. Efros, I. A. Yugova, D. Reuter, A. D. Wieck, and M. Bayer. Nuclei-induced frequency focusing of electron spin coherence. *Science*, 317:1896, 2007.

[25] L. V. Fokina, I. A. Yugova, D. R. Yakovlev, M. M. Glazov, I. A. Akimov, A. Greilich, D. Reuter, A. D. Wieck, and M. Bayer. Spin dynamics of electrons and holes in InGaAs/GaAs quantum wells at millikelvin temperatures. *Phys. Rev. B*, 81:195304, May 2010.

[26] S. Spatzek, A. Greilich, Sophia E. Economou, S. Varwig, A. Schwan, D. R. Yakovlev, D. Reuter, A. D. Wieck, T. L. Reinecke, and M. Bayer. Optical control of coherent interactions between electron spins in ingaas quantum dots. *Phys. Rev. Lett.*, 107:137402, Sep 2011.

[27] J. Schliemann, A. Khaetskii, and D. Loss. Electron spin dynamics in quantum dots and related nanostructures due to hyperfine interaction with nuclei. *Journal of Physics: Condensed Matter*, 15(50):R1809, 2003.

[28] A. Greilich, D. R. Yakovlev, A. Shabaev, Al. L. Efros, I. A. Yugova, R. Oulton, V. Stavarache, D. Reuter, A. Wieck, and M. Bayer. Mode locking of electron spin coherences in singly charged quantum dots. *Science*, 313(5785):341–345, 2006.

[29] D. Press, K. De Greve, P. L. McMahon, T. D. Ladd, B. Friess, C. Schneider, M. Kamp, S. Höfling, A. Forchel, and Y. Yamamoto. Ultrafast optical spin echo in a single quantum dot. *Nat Photon*, 4:367 – 370, Apr 2010.

[30] E. Fermi. Über die magnetischen Momente der Atomkerne. *Zeitschrift für Physik*, 60(5-6):320–333, 1930.

[31] I. A. Merkulov, Al. L. Efros, and M. Rosen. Electron spin relaxation by nuclei in semiconductor quantum dots. *Phys. Rev. B*, 65:205309, Apr 2002.

[32] W. A. Coish and D. Loss. Hyperfine interaction in a quantum dot: Non-markovian electron spin dynamics. *Phys. Rev. B*, 70:195340, Nov 2004.

[33] J. Fischer, W. A. Coish, D. V. Bulaev, and D. Loss. Spin decoherence of a heavy hole coupled to nuclear spins in a quantum dot. *Phys. Rev. B*, 78:155329, 2008.

[34] C. Testelin, F. Bernardot, B. Eble, and M. Chamarro. Hole-spin dephasing time associated with hyperfine interaction in quantum dots. *Phys. Rev. B*, 79:195440, May 2009.

[35] S. Lee, P. Von Allmen, F. Oyafuso, G. Klimeck, and K. Whaley. Electron spin dephasing and decoherence by interaction with nuclear spins in self-assembled quantum dots. *Conference paper*, 01 2004.

[36] M. Gaudin. Diagonalisation d,une classe d,hamiltoniens de spin. *J. Physique*, 37:1087, 1976.

[37] K. A. Al-Hassanieh, V. V. Dobrovitski, E. Dagotto, and B. N. Harmon. Numerical modeling of the central spin problem using the spin-coherent-state p representation. *Phys. Rev. Lett.*, 97:037204, Jul 2006.

[38] M. M. Glazov and E. L. Ivchenko. Spin noise in quantum dot ensembles. *Phys. Rev. B*, 86:115308, Sep 2012.

[39] M. Bortz and J. Stolze. Exact dynamics in the inhomogeneous central-spin model. *Phys. Rev. B*, 76:014304, Jul 2007.

[40] M. Bortz and J. Stolze. Spin and entanglement dynamics in the central-spin model with homogeneous couplings. *Journal of Statistical Mechanics: Theory and Experiment*, 2007(06):P06018, 2007.

[41] M. Bortz, S. Eggert, and J. Stolze. Spectrum and screening cloud in the central spin model. *Phys. Rev. B*, 81:035315, Jan 2010.

[42] M. Bortz, S. Eggert, C. Schneider, R. Stübner, and J. Stolze. Dynamics and decoherence in the central spin model using exact methods. *Phys. Rev. B*, 82:161308, Oct 2010.

[43] A. Faribault and D. Schuricht. Spin decoherence due to a randomly fluctuating spin bath. *Phys. Rev. B*, 88:085323, Aug 2013.

[44] A. Faribault and D. Schuricht. Integrability-based analysis of the hyperfine-interaction-induced decoherence in quantum dots. *Phys. Rev. Lett.*, 110:040405, Jan 2013.

[45] D. Stanek, C. Raas, and G. S. Uhrig. Dynamics and decoherence in the central spin model in the low-field limit. *Phys. Rev. B*, 88:155305, Oct 2013.

[46] N. A. Sinitsyn and Y. V. Pershin. The theory of spin noise spectroscopy: a review. *Reports on Progress in Physics*, 79(10):106501, 2016.

[47] E.B. Aleksandrov and V.S. Zapasskii. Magnetic resonance in the Faraday-rotation noise spectrum. *JETP*, 54:64, 1981.

[48] V. S. Zapasskii. Spin-noise spectroscopy: from proof of principle to applications. *Adv. Opt. Photon.*, 5(2):131–168, 2013.

[49] S. A. Crooker, D. G. Rickel, A. V. Balatsky, and D. L. Smith. Spectroscopy of spontaneous spin noise as a probe of spin dynamics and magnetic resonance. *Nature*, 431:49, 2004.

[50] M. Oestreich, M. Römer, R. J. Haug, and D. Hägele. Spin noise spectroscopy in GaAs. *Phys. Rev. Lett.*, 95(21):216603, 2005.

[51] S. A. Crooker, L. Cheng, and D. L. Smith. Spin noise of conduction electrons in n-type bulk gaas. *Phys. Rev. B*, 79:035208, Jan 2009.

[52] F. Berski, J. Hübner, M. Oestreich, A. Ludwig, A. D. Wieck, and M. Glazov. Interplay of electron and nuclear spin noise in n-type gaas. *Phys. Rev. Lett.*, 115:176601, Oct 2015.

[53] A. Bechtold, D. Rauch, F. Li, T. Simmet, P. Ardelt, A. Regler, K. Muller, N. A. Sinitsyn, and J. J. Finley. Three-stage decoherence dynamics of an electron spin qubit in an optically active quantum dot. *Nat Phys*, 11:1005, Sep 2015.

[54] G. S. Uhrig, J. Hackmann, D. Stanek, J. Stolze, and F. B. Anders. Conservation laws protect dynamic spin correlations from decay: Limited role of integrability in the central spin model. *Phys. Rev. B*, 90:060301, Aug 2014.

[55] S. A. Crooker, J. Brandt, C. Sandfort, A. Greilich, D. R. Yakovlev, D. Reuter, A. D. Wieck, and M. Bayer. Spin noise of electrons and holes in self-assembled quantum dots. *Phys. Rev. Lett.*, 104:036601, 2010.

[56] Y. Li, N. Sinitsyn, D. L. Smith, D. Reuter, A. D. Wieck, D. R. Yakovlev, M. Bayer, and S. A. Crooker. Intrinsic spin fluctuations reveal the dynamical response function of holes coupled to nuclear spin baths in (in,ga)as quantum dots. *Phys. Rev. Lett.*, 108:186603, May 2012.

[57] Ph. Glasenapp, D. S. Smirnov, A. Greilich, J. Hackmann, M. M. Glazov, F. B. Anders, and M. Bayer. Spin noise of electrons and holes in (in,ga)as quantum dots: Experiment and theory. *Phys. Rev. B*, 93:205429, May 2016.

[58] J. Hackmann and F. B. Anders. Spin noise in the anisotropic central spin model. *Phys. Rev. B*, 89:045317, Jan 2014.

[59] J. Hackmann, Ph. Glasenapp, A. Greilich, M. Bayer, and F. B. Anders. Influence of the nuclear electric quadrupolar interaction on the coherence time of hole and electron spins confined in semiconductor quantum dots. *Phys. Rev. Lett.*, 115:207401, Nov 2015.

[60] N. Wu, N. Fröhling, X. Xing, J. Hackmann, A. Nanduri, F. B. Anders, and H. Rabitz. Decoherence of a single spin coupled to an interacting spin bath. *Phys. Rev. B*, 93:035430, Jan 2016.

[61] N. A. Sinitsyn, Y. Li, S. A. Crooker, A. Saxena, and D. L. Smith. Role of nuclear quadrupole coupling on decoherence and relaxation of central spins in quantum dots. *Phys. Rev. Lett.*, 109:166605, Oct 2012.

[62] R. Dahbashi, J. Hübner, F. Berski, J. Wiegand, X. Marie, K. Pierz, H. W. Schumacher, and M. Oestreich. Measurement of heavy-hole spin dephasing in (InGa)As quantum dots. *Appl. Phys. Lett.*, 100:031906, 2012.

[63] P. Glasenapp, N. A. Sinitsyn, Luyi Yang, D. G. Rickel, D. Roy, A. Greilich, M. Bayer, and S. A. Crooker. Spin noise spectroscopy beyond thermal equilibrium and linear response. *Phys. Rev. Lett.*, 113:156601, Oct 2014.

[64] M. Poggio, H. J. Mamin, C. L. Degen, M. H. Sherwood, and D. Rugar. Nuclear double resonance between statistical spin polarizations. *Phys. Rev. Lett.*, 102:087604, Feb 2009.

[65] C. L. Degen, M. Poggio, H. J. Mamin, and D. Rugar. Role of spin noise in the detection of nanoscale ensembles of nuclear spins. *Phys. Rev. Lett.*, 99:250601, Dec 2007.

[66] D. K. Young, J. A. Gupta, E. Johnston-Halperin, R. Epstein, Y. Kato, and D. D. Awschalom. Optical, electrical and magnetic manipulation of spins in semiconductors. *Semiconductor Science and Technology*, 17(4):275, 2002.

[67] N. Jäschke, F. B. Anders, and M. M. Glazov. Electron spin noise under the conditions of nuclei-induced frequency focusing. *Phys. Rev. B*, 98:045307, Jul 2018.

[68] A. Greilich, R. Oulton, E. A. Zhukov, I. A. Yugova, D. R. Yakovlev, M. Bayer, A. Shabaev, Al. L. Efros, I. A. Merkulov, V. Stavarache, D. Reuter, and A. Wieck. Optical control of spin coherence in singly charged (In, Ga)As/GaAs quantum dots. *Phys. Rev. Lett.*, 96:227401, Jun 2006.

[69] N. Jäschke, A. Fischer, E. Evers, V. V. Belykh, A. Greilich, M. Bayer, and F. B. Anders. Nonequilibrium nuclear spin distribution function in quantum dots subject to periodic pulses. *Phys. Rev. B*, 96:205419, Nov 2017.

[70] S. Varwig, E. Evers, A. Greilich, D. R. Yakovlev, D. Reuter, A. D. Wieck, T. Meier, A. Zrenner, and M. Bayer. Advanced optical manipulation of carrier spins in (in,ga)as quantum dots. *Applied Physics B*, 122(1):17, 2016.

[71] R-B. Liu, S.-H. Fung, H.-K. Fung, A. N. Korotkov, and L. J. Sham. Dynamics revealed by correlations of time-distributed weak measurements of a single spin. *New Journal of Physics,*, 12:013018, 2010.

[72] A. Bechtold, F. Li, K. Müller, T. Simmet, P.-L. Ardelt, J. J. Finley, and N. A. Sinitsyn. Quantum effects in higher-order correlators of a quantum-dot spin qubit. *Phys. Rev. Lett.*, 117:027402, Jul 2016.

[73] F. Li and N. A. Sinitsyn. Universality in higher order spin noise spectroscopy. *Phys. Rev. Lett.*, 116:026601, 2016.

[74] L. M. Norris, G. A. Paz-Silva, and L. Viola. Qubit noise spectroscopy for non-gaussian dephasing environments. *Phys. Rev. Lett.*, 116:150503, Apr 2016.

[75] P. Szańkowski, G. Ramon, J. Krzywda, D. Kwiatkowski, and Ł. Cywiński. Environmental noise spectroscopy with qubits subjected to dynamical decoupling. *Journal of Physics: Condensed Matter*, 29, 05 2017.

[76] D. Hägele and F. Schefczik. Higher-order moments, cumulants, and spectra of continuous quantum noise measurements. *Phys. Rev. B*, 98:205143, Nov 2018.

[77] J. Márquez, L. Geelhaar, and K. Jacobi. Atomically resolved structure of InAs quantum dots. *Appl. Phys. Lett.*, 78(16):2309–2311, 2001.

[78] L. Goldstein, F. Glas, J. Y. Marzin, M. N. Charasse, and G. Le Roux. Growth by molecular beam epitaxy and characterization of InAs/GaAs strained layer superlattices. *Applied Physics Letters*, 47(10):1099–1101, 1985.

[79] I. Stranski and L. Kastranov. *Abhandlungen der mathematisch- naturwissenschaftlichen Klasse*. Akademie der Wissenschaften und der Literatur in Mainz, 1939.

[80] S. Huang, S. J. Kim, R. Levy, X. Q. Pan, and R. S. Goldman. Mechanisms of InAs/GaAs quantum dot formation during annealing of In islands. *Applied Physics Letters*, 103(13):132104, 2013.

[81] B. Urbaszek, X. Marie, T. Amand, O. Krebs, P. Voisin, P. Maletinsky, A. Högele, and A. Imamoglu. Nuclear spin physics in quantum dots: An optical investigation. *Rev. Mod. Phys.*, 85:79–133, Jan 2013.

[82] M. M. Glazov. *Electron & Nuclear Spin Dynamics in Semiconductor Nanostructures*. Series on Semiconductor Science and Technology. OUP Oxford, 2018.

[83] A. Abragam. *Principles of nuclear magnetism*. Oxford University Press, 1961.

[84] G. H. Fuller. Nuclear spins and moments. *J. Phys. Chem. Ref. Data*, 5:835, 1976.

[85] J. Hackmann. Spin dynamics in doped semiconductor quantum dots. Phd dissertation, TU Dortmund, 2015.

[86] C. P. Slichter. *Principles of Magnetic Resonance*. Springer Science & Business Media,, Berlin, 1996.

[87] C. Bulutay. Quadrupolar spectra of nuclear spins in strained $In_xGa_{1-x}As$ quantum dots. *Phys. Rev. B*, 85:115313, Mar 2012.

[88] N. Grewe. A theory for the anderson lattice. *Zeitschrift für Physik B Condensed Matter*, 67(3):323–339, Sep 1987.

[89] N. Grewe, T. Pruschke, and H. Keiter. Investigation of the low temperature behaviour of the anderson lattice. *Zeitschrift für Physik B Condensed Matter*, 71(1):75–94, Mar 1988.

[90] A. N. Rubtsov, M. I. Katsnelson, A. I. Lichtenstein, and A. Georges. Dual fermion approach to the two-dimensional hubbard model: Antiferromagnetic fluctuations and fermi arcs. *Phys. Rev. B*, 79:045133, Jan 2009.

[91] H. Hafermann, S. Brener, A. N. Rubtsov, M. I. Katsnelson, and A. I. Lichtenstein. Cluster dual fermion approach to nonlocal correlations. *JETP Letters*, 86(10):677–682, Jan 2008.

[92] H. Hafermann. Numerical approaches to spatial correlations in strongly interacting fermion systems. Phd dissertation, Universität Hamburg, 2009.

[93] W. Belzig. Full counting statistics of super-poissonian shot noise in multilevel quantum dots. *Phys. Rev. B*, 71:161301, Apr 2005.

[94] J. C. Cuevas and W. Belzig. Full counting statistics of multiple andreev reflections. *Phys. Rev. Lett.*, 91:187001, Oct 2003.

[95] M. Braun and J. König. Faraday-rotation fluctuation spectroscopy with static and oscillating magnetic fields. *Phys. Rev. B*, 75:085310, Feb 2007.

[96] Š. Kos, A. V. Balatsky, P. B. Littlewood, and D. L. Smith. Spin noise of itinerant fermions. *Phys. Rev. B*, 81:064407, Feb 2010.

[97] M. M. Glazov and E. Ya. Sherman. Theory of spin noise in nanowires. *Phys. Rev. Lett.*, 107:156602, Oct 2011.

[98] R. Kubo. Generalized cumulant expansion method. *Journal of the Physical Society of Japan*, 17(7):1100–1120, 1962.

[99] J. M. Mendel. Tutorial on higher-order statistics (spectra) in signal processing and system theory: theoretical results and some applications. *Proceedings of the IEEE*, 79:278–305, Mar 1991.

[100] A. Khintchine. Korrelationstheorie der stationären stochastischen Prozesse. *Mathematische Annalen*, 109(1):604–615, Dec 1934.

[101] G. G. Kozlov. Exactly solvable spin dynamics of an electron coupled to a large number of nuclei; the electron-nuclear spin echo in a quantum dot. *Journal of Experimental and Theoretical Physics*, 105(4):803–815, Oct 2007.

[102] C. Lanczos. An iterative method for the solution of the eigenvalue problem of linear differential and integral. *J. Res. Nat. Bur. Std.*, 45:255, 1950.

[103] A. Weiße, G. Wellein, A. Alvermann, and H. Fehske. The kernel polynomial method. *Rev. Mod. Phys.*, 78:275–306, Mar 2006.

[104] N. Fröhling, N. Jäschke, and F. B. Anders. Fourth-order spin correlation function in the extended central spin model. *arXiv:1901.08923*, Jan 2019.

[105] G. Chen, D. L. Bergman, and L. Balents. Semiclassical dynamics and long-time asymptotics of the central-spin problem in a quantum dot. *Phys. Rev. B*, 76:045312, Jul 2007.

[106] D. Stanek, C. Raas, and G. S. Uhrig. From quantum-mechanical to classical dynamics in the central-spin model. *Phys. Rev. B*, 90:064301, Aug 2014.

[107] N. Fröhling and F. B. Anders. Long-time coherence in fourth-order spin correlation functions. *Phys. Rev. B*, 96:045441, Jul 2017.

[108] B. Fauseweh, P. Schering, J. Hüdepohl, and G. S. Uhrig. Efficient algorithms for the dynamics of large and infinite classical central spin models. *Phys. Rev. B*, 96:054415, Aug 2017.

[109] E. S. Artemova and I. A. Merkulov. Nuclear field and Faraday effect in semiconductors. *Sov. Phys. Solid State*, 27:941, 1985.

[110] R. Giri, S. Cronenberger, M. M. Glazov, K. V. Kavokin, A. Lemaître, J. Bloch, M. Vladimirova, and D. Scalbert. Nondestructive measurement of nuclear magnetization by off-resonant Faraday rotation. *Phys. Rev. Lett.*, 111:087603, 2013.

[111] N. Fröhling, F. B. Anders, and M. Glazov. Nuclear spin noise in the central spin model. *Phys. Rev. B*, 97:195311, May 2018.

[112] E. A. Chekhovich, M. M. Glazov, A. B. Krysa, M. Hopkinson, P. Senellart, A. Lemaitre, M. S. Skolnick, and A. I. Tartakovskii. Element-sensitive measurement of the hole-nuclear spin interaction in quantum dots. *Nat Phys*, 9(2):74–78, 2013.

Acknowledgements

I thank my advisor Prof. Anders and my advisor Prof. Glazov for the advice and support during my thesis, and all the work they put into helping me. I thank my boyfriend, Daniel, for his support, patience and understanding. I also thank my parents for the fiscal and human support that made my studies possible. I thank my colleagues Natalie, Andreas and Iris for reading my thesis and their helpful corrections. I thank everyone in the T2 department, but especially my office-mates Natalie and Andreas, for making the last few years such an enjoyable time.